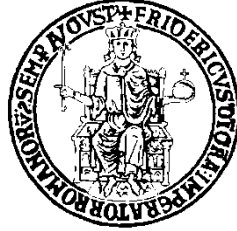


UNIVERSITÀ DEGLI STUDI DI NAPOLI FEDERICO II



*Dottorato di ricerca*

In

**INGEGNERIA STRUTTURALE,  
GEOTECNICA E RISCHIO SISMICO  
XXX CICLO**

**Earthquake Early warning Strategies for on-site and network  
based systems**

**Relatore**

Prof. Aldo Zollo

**Coordinatore**

Prof. Luciano Rosati

**Correlatrice**

Dott.ssa Simona Colombelli

**Ph.D. student**

Alessandro Caruso

# Summary

<b>Introduction</b> .....	7
<b>Preliminary concept of EEW</b> .....	8
<b>EEWS approaches</b> .....	9
<b>Technology improving and EEWS worldwide</b> .....	11
<b>Motivations and proposal</b> .....	15
<b>Chapter 1: An on-site early warning <math>Pd-\tau c</math> approach for Italy</b> .....	17
<b>1.1 Introduction</b> .....	17
<b>1.2 Methodology</b> .....	18
<b>1.3 Application and results</b> .....	24
<b>1.4 Discussion</b> .....	30
<b>Chapter 2: On-site Early warning Systems and a P-wave based approach</b> .....	35
<b>2.1 Introduction</b> .....	35
<b>2.2 Methodology</b> .....	36
<b>2.3 Test and performance</b> .....	41
<b>2.3.1 Application to the Japanese data-set</b> .....	41
<b>2.3.2 Application to the Italian data-set</b> .....	48
<b>2.4 Discussion</b> .....	56
<b>Chapter 3: Rapid estimation of the earthquake potential damage zone</b> .....	61
<b>3.1 Introduction</b> .....	61
<b>3.2 Methodology</b> .....	63

3.3.1 Application to 2016 Norcia 6.5 Mw earthquake .....	70
3.3.2 Application to Japan earthquakes .....	77
3.4 Discussion .....	86
<b>Chapter 4: Early warning system embedded into a seismic station .....</b>	<b>89</b>
4.1 Introduction .....	89
4.2 MOMA project .....	90
4.2.2 Analog to digital conversion.....	91
4.2.3 Timing module (GPS).....	92
4.3 End-user interface .....	94
4.4 EEWS for MOMA.....	95
4.5 Spectral straightening of the Geophone response .....	97
4.6 Discussion .....	99
<b>Conclusions .....</b>	<b>100</b>

## Abbreviations:

Earthquake Early Warning (EEW); Lead Time (LT); Filter Picker (FP); Characteristic Function (CF); P-wave Time Window (PTW); Peak Displacement ( $Pd$ ); Peak Velocity ( $Pv$ ); Peak acceleration ( $Pa$ ); Peak Ground Velocity (PGV); Ground Motion Prediction Equations (GMPEs).

## Glossary

**Earthquake Early Warning System :** Real-time, modern information systems that are able to provide rapid notification of the potential damaging effects of an impending earthquake, through the rapid telemetry and processing of data.

**Earthquake location:** An earthquake location specifies the spatial position and time of occurrence for an earthquake. The location may refer to the earthquake hypocenter and corresponding origin time, a mean or centroid of some spatial or temporal characteristic of the earthquake, or another property of the earthquake that can be spatially and temporally localized.

**Earthquake magnitude:** The magnitude is a parameter used by seismologists to quantify the earthquake size. The Richter magnitude scale, or more correctly local magnitude ML scale, assigns a single number to quantify the amount of seismic energy released by an earthquake. It is a base-10 logarithmic scale obtained by calculating the logarithm of the combined horizontal amplitude of the largest displacement from zero on a seismometer output. Measurements have no limits and can be either positive or negative. Introduced by the Japanese seismologist Aki in 1962, the seismic moment is the present-day physical parameter used to characterize the earthquake strength. It represents the scalar moment of one the couples of forces producing the dislocation at an earthquake fault and it is measured from the asymptotic DC level on displacement Fourier spectra of recorded seismic signals.

**Lead-time:** The time available from the moment of the alert is issued to the arrival of the strongest shaking at each site. The lead-time is the time available to start emergency actions after the warning

declaration and can be a matter of few seconds or tens of seconds, depending on the source-to-receiver distance. Due to the increasing travel-time difference between S- and P-waves, the greater the distance between the target and the source region, the longer the lead-time. In a regional Early Warning System the lead-time is the time available from the first P-wave detection at the network and the S-wave arrival at the target site. In an on-site system, the lead-time is given by the arrival time difference between P and S-waves. Generally, the lead time for a regional system is greater than that of an on-site configuration.

**Seismic Data-Logger:** It is a core element of a digital seismic station, whose aim is to record the analogue signals from seismic sensors and convert them in a digital form with an assigned sampling frequency. Ground motion signal acquired by seismic sensors are pre-amplified and anti-aliasing filtered in a data-logger before they are digitalized through an AD (analog-to-digital) converter. The main technical features of a modern data-logger are the number of available channels, the allowed sampling frequencies, the dynamic range, the digitizer clock type, the storage capacity (PCMCIA, internal flash and/or hard disk, USB, ...) , network interfaces (Ethernet, wireless LAN, or point-to-point) and power consumption.

**Seismic sensors:** The instruments which are used to record the ground vibration produced by natural and artificial sources, are generally denoted as seismometers. Seismometer measures the relative motion between the frame and the suspended mass. Early seismometers used optics, or motion-amplifying mechanical linkages. The motion was recorded as scratches on smoked glass, or exposures of light beams on photographic paper. In modern instruments the proof mass is held motionless by an electronic negative feedback loop that drives a coil. The distance moved, speed and acceleration of the mass are directly measured. Most of modern seismometers are broad band, working on a wide range of frequencies (0.01-100 Hz). Another type of seismometer is a digital strong-motion seismometer, or

accelerometer, since it measures soil acceleration. Due to its relatively high dynamic range, the accelerometers can record unsaturated strong amplitude signals at close distances from a large earthquakes. This data is essential to understand how an earthquake affects human structures.

**Blind Zone:** The area that cannot benefit from the warning provided by the Early Warning Systems, since the alert for the impending earthquake is given after the arrival of the damaging S-waves. As soon an earthquake is detected by an Early Warning System, few seconds of P-wave need to be analyzed, in order to compute the expected magnitude or the expected ground motion at the target and to decide whether to issue the warning or not. While the P-wave signals are being analyzed, the S-wave travel and may reach the closest target sites, before the warning is issued. The area in which the alert is provided after the arrival of the S-waves is called blind zone. The blind zone might be generally influenced by the source depth and wave velocity, as well as by geometry and density of the network.

# Introduction

At the sites of high seismic risk, earthquake hazards are a serious threat to the lives and property in urban areas. For the real-time seismic hazard mitigation, a useful approach is the development of Earthquake Early Warning Systems (EWS) which are automatic, real-time information systems able to detect an ongoing earthquake and broad-casting a warning in a target area, before the arrival of the most destructive waves (Nakamura, 1984, 1988; Heaton, 1985; Teng et al., 1997; Wu et al., 1998; Wu and Teng, 2002; Allen and Kanamori, 2003).

Many regions in the world are affected by natural hazards such as earthquakes, tsunamis, volcanoes, floods, storms, landslides, etc., each having devastating socio-economic impacts. Among these natural events, earthquakes, have been the most recurrent and damaging hazards during the last few decades, resulting in large numbers of casualties, and massive economical losses (Munich Re, 2006).

The problem of earthquake risk mitigation is faced using different approaches, depending upon the time scale being considered. Whilst over time scales of decades it is of utmost importance that land use regulations and building/infrastructure codes are continuously updated and improved, for time scales of a few years, the main risk mitigation actions are at the level of information and education in order to increase the individuals and social community awareness about potential damaging hazards. Over shorter time scales (months to hours), it would naturally be of great benefit to society as a whole if the capability to accurately predict the time, location and size of a potentially catastrophic natural event were available. However, due to the great complexity of the natural processes of concern, such predictions are currently not possible.

On the other hand, on very short time scales (seconds to minutes), new strategies for earthquake risk mitigation are being conceived and are under development worldwide, based on real-time information

about natural events that is provided by advanced monitoring infrastructures, denoted as “early warning systems”.

## **Preliminary concept of EEW**

The origin of the term “early warning” probably goes back to the first decades of the last century. However, the first practical use of an “early warning” strategy was military and it was developed during the “cold war” years as a countermeasure to the potential threat from ballistic intercontinental missiles. The objective of these systems was to give an alert to target areas as soon as a missile was detected by the radar system or a launch was detected by the satellite system. In this context, the term “lead time” was defined as the time elapsing from the detection of the missile to the estimated impact on the target.

In the last decades the use of the term “early warning” greatly expanded. It is used with small, but significant, variations in several types of risks, from epidemiological, to economical, social, and of course all the types of natural and environmental risks. In fact in these contexts, including some natural risks such as hydro-geological and volcanic, the warning is not given at the onset of the catastrophic phenomenon, but after the occurrence of some precursory phenomena which can trigger a catastrophic event (for instance intensive rainfall for hydrological risk, earthquakes and/or ground deformation for volcanic risk). The main consequence of this difference is the increase of probability of issuing false alarms.

The case of earthquake early warning is similar to the missile early warning. The alert is given after an earthquake is detected by a network of seismometers. An earthquake early warning is based on the fact that most of the radiated energy is contained in the slower travelling phases (S- and surface waves travelling at about 3.5 km/s or less) which arrive at any location with a delay with respect to small



amplitude higher velocity phases (P-waves, travelling at about 6-7 km/s) or to EM transmitted signals giving the warning.

## EEWS approaches

There are two primary types of EEWS. A “regional” (or network-based) EEWS is based on a dense sensor network covering a portion of, or the entirety of an area that is threatened by earthquakes. In this configuration, the relevant source parameters, e.g. event location and magnitude, are estimated from the early portion of recorded signals (initial P-waves) and are used to predict, with uncertainties,

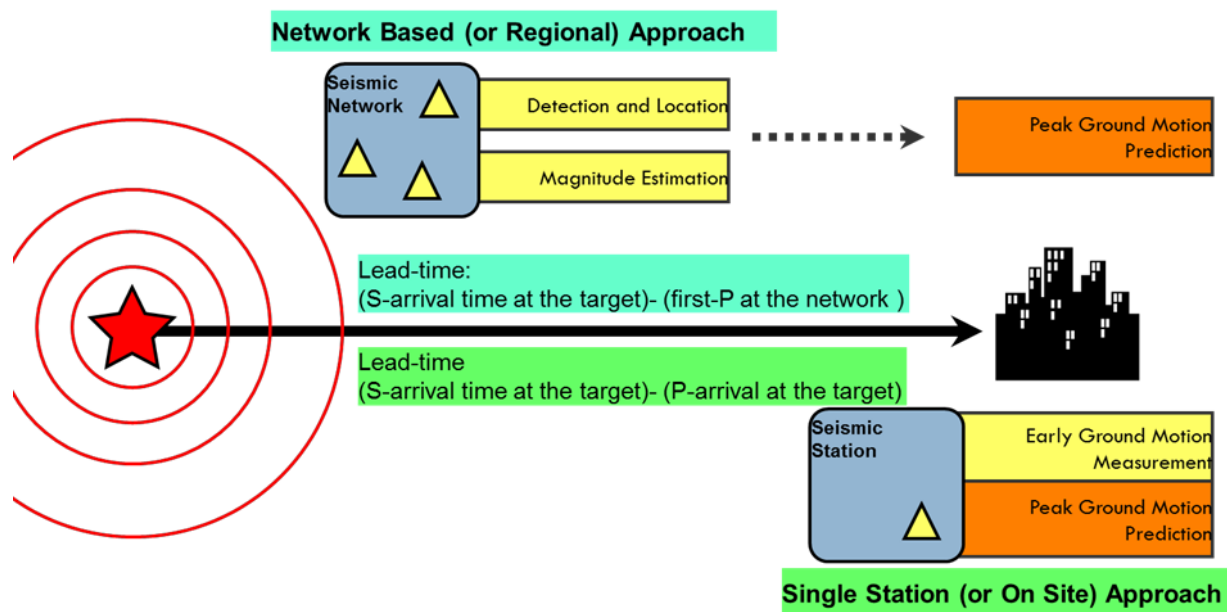


**FIGURE 2: EEWS approaches:** The figure shows a schematic configuration of regional and on-site EEWS.

the ground motion intensity expected at a distant site where a target structure of interest is located. Alternatively, a “site-specific” (or on-site) EEWS consists of a single sensor or an array of sensors deployed at (or in the proximity of) the target structure that is to be alerted, and whose measurements

of amplitude and predominant period of the initial P-wave motion are used to predict the ensuing peak ground motion (mainly related to the arrival of S and surface waves) at the same site.

A significant difference among the two configurations concerns the lead-time, i.e. the time available for the issuance of the warning before the arrival of strong ground shaking at the target sites. The maximum theoretical lead-time for regional EEWs is often defined as the time difference between the S arrival at the target and the first P arrival at the seismic network. However, an EEW system typically

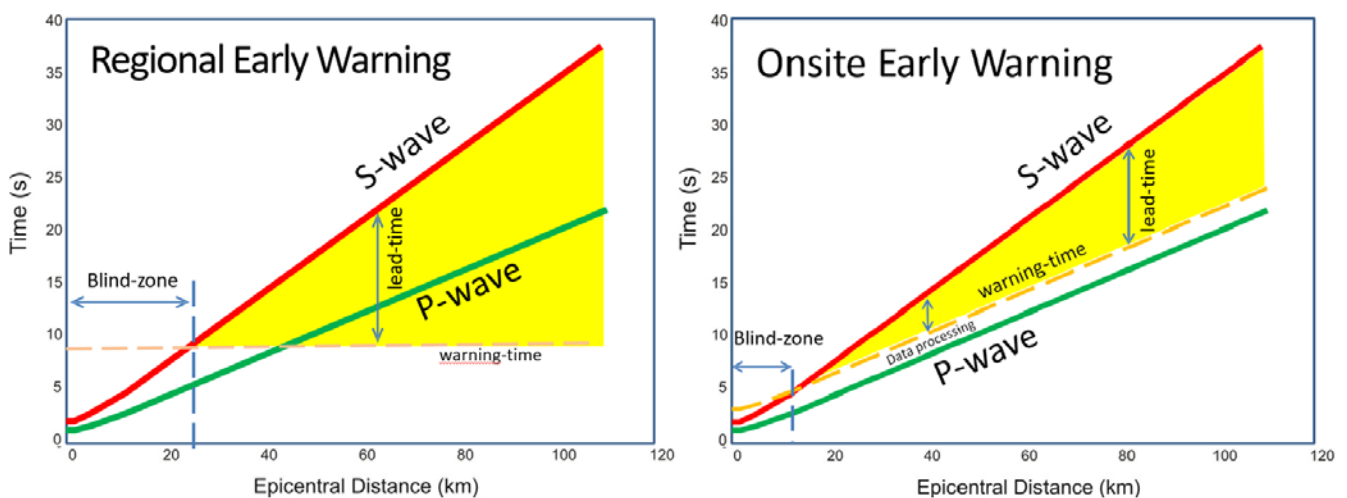


**FIGURE 3: EEWs lead-times:** The figure shows the Lead-times for two different EEWs approaches.

Requires a few seconds to detect the event, evaluate its severity, and decide whether to issue the alert, so that the effective lead-time is always smaller. It is clear that, for such systems, the lead-time increases with the distance of the target and with the rapidity of the detection. If the target site is close to the epicentral area, the regional approach may not be viable, since the lead-time may be zero, or can be too small for any application. For regional EEWs the extent of the “blind zone”, e.g. the area within which destructive Swaves may arrive before a warning can be issued, depends on the earthquake depth, network coverage of the source, and the speed of the telemetry and processing system. Its radius is typically 30km for shallow crustal earthquakes and a relatively dense network (station spacing 20-30

km). The onsite warning method uses the early part of the P-wave signal to predict the ensuing peak ground motion (mainly S and surface waves) at the same site. In this case, the theoretical lead-time can be defined as the time interval between the P and the S arrival at the target, though, again, some seconds for detection and computation must be taken into account. Similar to the case for the regional approach, the lead-time for the onsite methodology increases with the epicentral distance due to the growing travel-time difference between the slower S-phase and the faster P-phase. It is theoretically possible that the onsite EEWS can provide a useful lead-time where a regional EEWS system cannot, due to a significantly smaller blind zone. However, the cost is the higher false alarm rates. Still, when a regional strategy is possible, it generally provides a larger lead-time [Satriano *et al.*, 2010].

## **Technology improving and EEWS worldwide**

The latest technological innovations in seismic sensors, digitizers, communication systems, computers and seismological methods has greatly enhanced the capability of the seismic network.

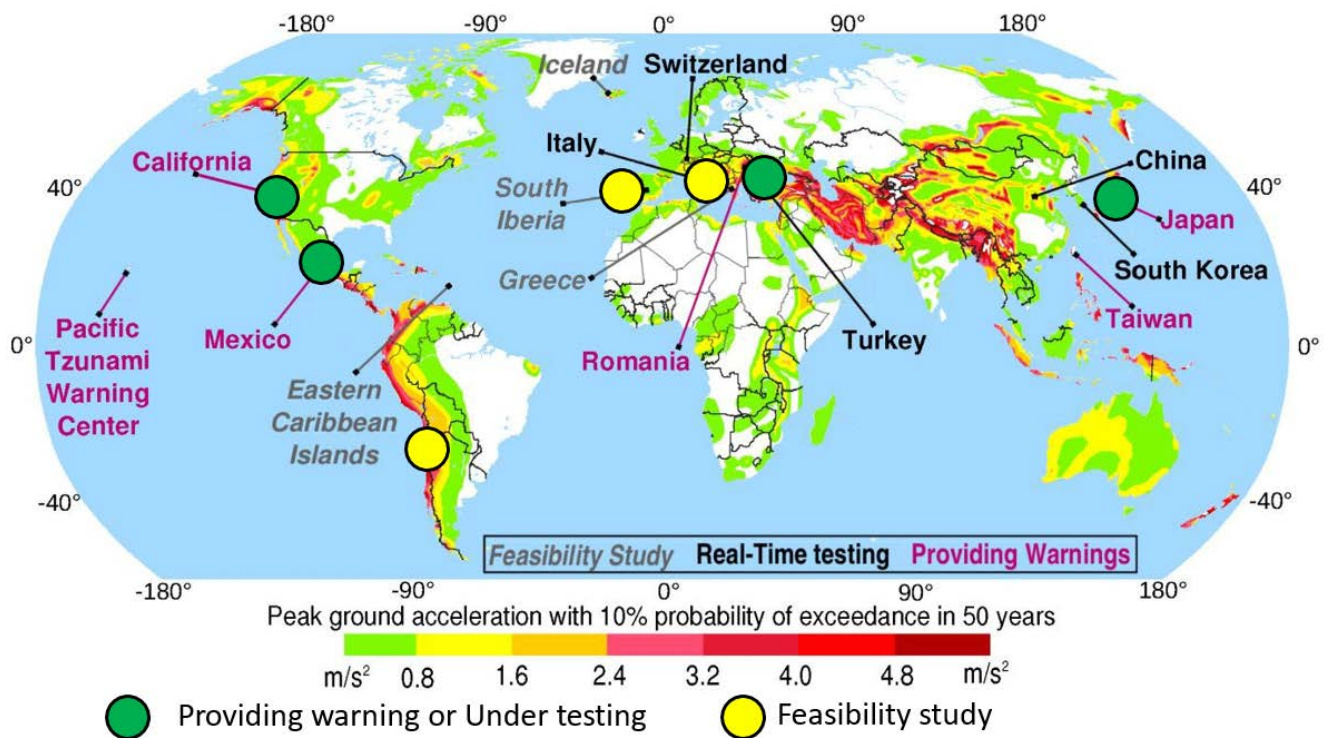


**FIGURE 2: EEWS worldwide:** The figure shows the development of EEWS in the world.

High-capacity digital communication systems, both land lines from the local telephone service providers and spread spectrum radios, that are capable of sending large amounts of data rapidly and reliably are now available.

The modern accelerographs and 24-bit digital data loggers can record motion ranging from the very weak, less than  $10^{-9}$  g, to very strong, for instance 2-4 g (where g is the acceleration due to gravity at the Earth's surface). This allows having reliable waveforms of both micro seismicity and events that cause a strong soil shake, which makes it particularly suitable for use in preventive alert systems.

Modern computers with multiple central processing units provide enough capability for processing data for real-time seismic systems. Overall, the introduction of modern sensors, digital data loggers, communication systems and computers holds promise for building rapid and reliable systems for real-

time monitoring of the distribution of strong ground motion, the essential for emergency operations and early warning systems.

Active warning systems that provide alerts to one or more users have been documented in different countries. Mexico and Japan stand apart as having systems with warnings provided to the general public via multiple communication routes. Taiwan, Turkey, Romania and California also have warning systems that provide information to one or more users.

In Switzerland , the Virtual Seismology (VS) system (Cua, 2005; Cua and Heaton, 2007; Cua et al., 2009) is undergoing real-time testing. The system uses a Bayesian approach. VS predicts the source location and the earthquake's magnitude using prior information inferred by the area seismicity history. VS is among the 3 EEW algorithms integrated in the CISN (California Integrated Seismic Network) ShakeAlert system. In Addition, the ShakeAlert system uses the ElarmS EEW methodology that is testing on the Californian network (Allen, Brown, Hellweg et al. 2009). Using the arrival time of the P-wave and the frequency content measured at several stations, ElarmS estimates the location and the magnitude of the earthquake. Last, the third system is an on-site algorithm. This is a single-sensory approach to EEW (Kanamori, 2005) that will be discussed in the following section.

In Mexico, the operational network-based warning system has been developed after the M 8.1 earthquake on 19 September 1985. This EEWS is based on two components: the SAS system for Mexico City and Guerrero and the SASO system for Oaxaca (Espinosa-Aranda et al. 1995). When two or more stations detect a dangerous earthquake, the system sends a warning to the public; when two or more detect a moderate earthquake, a “preventive” warning is issued. Espinosa-Aranda & Rodriguez (2003) describes the details of this system and its performance.

In Japan, the Railways began using systems of alert notification in the 1960s in order to shut off power to the Shinkansen bullet trains. The grandfather of onsite EEWS, UrEDAS (Nakamura 1988), started

operation along the Shinkansen lines in 1992 and was expanded across the system following the 1995 Kobe earthquake. Also, the Kobe earthquake event motivated the installation of a nationwide seismic networks with constant station density across the country. Following the installation of these networks, JMA (Japan Meteorological Agency) began testing EEW methodologies in February 2004. Now the public warnings from JMA are communicated to the people via various means (radio, tv, smartphone etc...). Engineering and construction companies are also using the warning systems both to provide enhanced building performance during earthquakes and to protect construction workers.

In Taiwan, after the Hualien's earthquake M 7.8 (1986), an early warning strategy was developed. The first EEW system in Taiwan started operation in 2001 and used ~100 accelerometers located across the island and a Virtual Sub-Net (VSN) algorithm to detect and locate earthquakes and estimate magnitudes. In order to reduce the size of the blind zone a second system that uses an on-site approach is now being tested. The public does not receive the warning, because no public education campaign has been possible but the warnings have been issued in an experimental mode to railway and rapid transit companies, disaster prevention agencies, and a hospital (Hsiao et al. 2009).

In Bucharest, the Horia Hulubei National Institute of Physics and Nuclear Engineering receives the warning notification by an EEWS. Where it is used to move in a safe position the nuclear source (Ionescu et al. 2007).

In Italy, the most important seismic risk areas are the Southern Apennines region. Here, the latest strong earthquake (Mw 6.9 1980), caused extensive damage and 3000 casualties. In the 2005, the development of a local seismic network in the Campania-Lucania region, called ISNet (Irpinia Seismic Network) ( Satriano et al., 2009), has been started. The goals of the network are: a) high-resolution studies of the seismogenic faults using the high-quality local data b) testing the EEWS to protect the strategically relevant infrastructures in the region as schools, factories railways etc. The early warning

algorithms have been embedded into an EEW platform called PRESTo (PRobabilistic and Evolutionary early warning SysTem) (Zollo et al. 2009). PRESTo is a software platform for regional EEW that is in testing phase on the ISNet network data-stream.

## **Motivations and proposal**

The main topic of this analysis is the development and testing of possible strategies to seismic risk mitigation through the declaration of alert message, ongoing of earthquake, before that the strong shaking occur. With this aim, a single and multi-stations approach are investigated performing statistical test to proof the rapidity and reliability of alert.

The first step of this study is explained in the chapter 1, where an on-site EEWS approach, called SAVE system, is implemented and tested. The system is a basic on-site single-station approach able to quickly characterize the earthquake in term of local intensity, magnitude and distance classification. The estimates provided by the system are affected by rather large uncertainties but the methodology is rapid, so to allow for an effective activation of automatic procedures for risk mitigation, also at the target sites very close to the source. The low computational cost of this algorithm makes it suitable for embedded solutions in a standalone seismic station, and a prototype was developed and described in the final chapter. In chapter 2, a refined and more accurate on-site system is proposed. Unlike the SAVE methodology, this P-wave based approach is aimed at providing a reliable overcoming prediction of the critical intensity level at recording site. The use of advanced data processing techniques, jointed with a multi-parameter approach, provides a more reliable prediction of maximum local intensity expected at site. This approach is useful for the rapid and strictly constrained local intensity prediction.

Chapter 3 finally describes an integrated methodology aimed to interpolate the information obtained from the individual stations and map the potential damage zone (PDZ) in real time. Further details on

this methodology, called Quake-up, are discussed in the same Chapter. In chapter 4, technical details about the project development of seismic station, called MOMA, and improvement of the spectral response of on-board geophone were provided.



# Chapter 1: An on-site early warning $Pd-\tau_c$ approach for Italy

## 1.1 Introduction

A recent feasibility study for a nationwide EEWs in Italy has been developed by *Picozzi et al.*, [2015]. The Italian strong motion network (RAN), owned and managed by the Italian Department of Civil Protection (DPC) [*Gorini et al.*, 2010], and the EEW software platform PRESTo have been considered, showing that, despite the high RAN's station density, a regional EEW approach for Italy may not provide timely warnings within a distance of about 25 km to 30 km from the epicenters. This observation, due to the closeness in Italy of seismogenic faults and populated cities, was the strong motivations to conceive, develop and propose an on-site approach to EEW. However, it is worth noting that many other seismic prone countries share a distribution of faults and cities similar to Italy.

An on-site, P-wave, based EWS (denoted as SAVE, Onsite Alert Level) was validated and tested. It has been conceived to operate either with a single station (i.e., a single sensor located at the target site) or with a set of co-located seismic nodes within a small area round the target to protect.

SAVE processes the vertical component of both accelerometers and (broad-band) velocimeters. Based on the real-time measurement of the initial Peak Displacement ( $Pd$ ) [*Wu et al.*, 2006; *Zollo et al.*, 2006] and the average period ( $\tau_c$ ) [*Kanamori*, 2005] over time windows of 1, 2 and 3 seconds after the P-phase arrival, SAVE predicts the expected ground shaking at the recording site, issues a local alert level and a qualitative assessment about the earthquake magnitude and the source to-site distance (Figure 1). As soon as a detected signal exceeds some user-configurable thresholds of the output parameters (e.g. predicted intensity IV or above), SAVE delivers a warning message both via internet (via UDP) and a

visual display, while providing a readable summary of the outputs of the system, which is also sent to remote users by mail.

During the follow chapter, first introduce the software platform SAVE and describe its methodology. Then, we evaluate the performance of the system, by applying it retrospectively to a database of earthquakes that have occurred during the last 10 years in Italy and have been recorded by the RAN network (made freely available by the ITalian ACcelerometric Archive, ITACA 2.0, <http://itaca.mi.ingv.it/ItacaNet/>;) [Luzi et al., 2008; Pacor et al., 2011].

## 1.2 Methodology

The on-site system SAVE processes the vertical ground motion component from one or more co-located sensors at a recording site. Both acceleration and (broad-band) velocity probes are supported. The waveforms can be streamed in real-time from the data loggers, or played-back from past events in off-line mode. In the real-time mode, SAVE supports the SeedLink protocol for data streaming, which

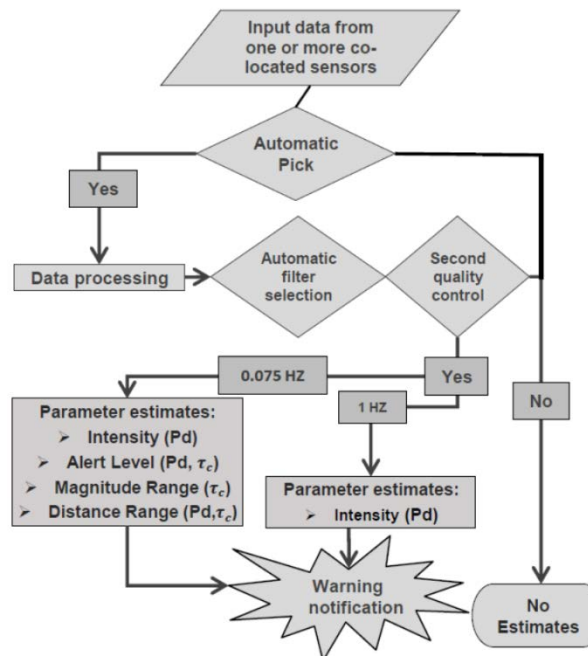


FIGURE 1.1: SAVE ALGORITHM. The figure shows the block diagram of SAVE algorithm.

has been chosen because it is commonly implemented in data-loggers or available through the installation of the *SeisComP* server for data collection [*SeisComP*, 2016].

In the off-line, simulation mode, each sensor component is read from a file in SAC format [*P. Goldstein et al.* 2003]. In off-line mode, previously recorded data (i.e., playbacks) are analyzed in 1-second consecutive packets, to simulate the actual *SeedLink* streams. Random transmission delays and data gaps can be configured to simulate the cases where the data-logger and SAVE are connected by a telecommunication network. This simulation mode is useful for batch testing and for the performance evaluation from a catalog of pre-recorded events, and it has been used to provide the statistics of the system output.

The preliminary data processing consists of: 1/ real-time mean value and linear trend removal, 2/ automatic picking of the P-phase, and 3/ a quality control based on the Signal-to-Noise Ratio (SNR). The P-wave picking algorithm implemented in SAVE is *FilterPicker* [*Lomax et al.*, 2012], which is optimized for earthquake early warning, as it already operates on data packets of variable lengths and it can declare a pick (P-wave arrival time measure) within few samples from the trigger. Five configuration parameters control the long and short time windows on which a characteristic function (*CF*) is evaluated. Among the configuration parameters, the most relevant are the thresholds for *CF* picking declaration and the minimum time window after a trigger where the *CF* must exceed these thresholds, which allows to ignore spikes and glitches of short duration (see *Lomax et al.*, [2012] for further details). When a single sensor is used, indeed, the risk for a wrong P-wave detection due to spurious, transient signals (e.g. from anthropic sources) is relatively high. Therefore, in order to avoid the declaration of too many false alarms, the automatic picking algorithm can be configured to be less sensible to spurious transient signals and different criteria to filter and rule-out low quality data have been implemented. The proper setting of *FilterPicker* parameters is extremely relevant for the onsite early-warning system in order to avoid the issuance of false alarms. The selection of the picker

parameters mainly depends on the noise level at the site, but also on the magnitude and distance ranges of the expected events, which determine the minimum ground motion level to be detected for the warning declaration.

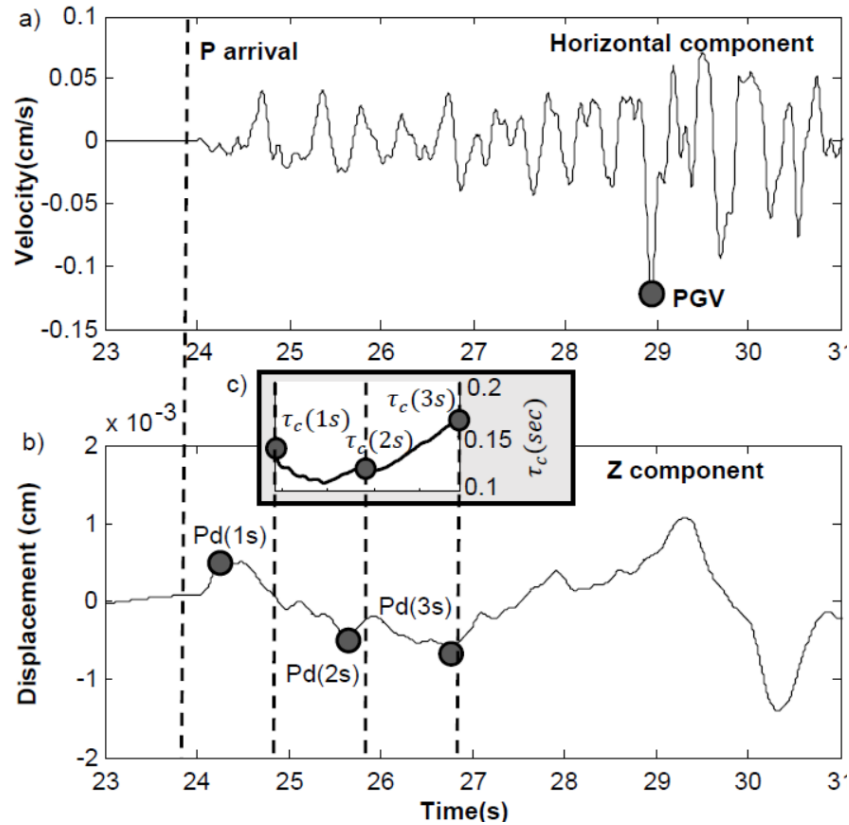


**FIGURE 1.2: DATA PROCESSING.** Panel (a) shows an example of horizontal component of the ground motion velocity. The grey circle represents the PGV (Peak ground velocity) measurement. Panel (b) shows the processing of the vertical-component of the ground displacement. From left to right, dashed lines represent the P-wave arrival time and 1 2 and 3 seconds after the P-wave picking, while grey circles show the  $P_d$  measurements, at 1, 2 and 3 seconds, respectively. Panel (c) shows the time evolution of  $\tau_c$  [1.1] and gray circles represent the three measurement after 1,2 and 3 seconds from the P-wave arrival time.

In case of event detection, three consecutive time window lengths are selected for the analysis: 1, 2 and 3 seconds after the first P-wave arrival (Figure 1.2). The data processing starts with a quality control of the recorded waveforms, which is based on the SNR and on the computation of the  $P_d/P_v$  ratio in a pre-determined time window.  $P_d$  and  $P_v$  are the peak displacement and velocity in the selected P-wave time

window, respectively. In particular, the quantity  $SNR$  is computed as  $SNR = 20 * \log_{10}(P_d/P_d^N)$ , where  $P_d$  is measured on the available signal in the selected time window and  $P_d^N$  is the maximum displacement of the pre-event noise, over the same time window. As for the  $P_d/P_v$  ratio, both peak amplitude parameters are measured in the same time window, using the displacement and velocity waveforms, respectively. A predetermined threshold value on their ratio is used to reject data possibly contaminated by noise. In fact, accelerometer waveforms are usually integrated once and twice to obtain displacement time series. The trace integration may lead to unstable results and low-frequency drifts [Boore *et al.*, 2002], which are generally corrected in real-time through the application of a proper high-pass filtering. If velocity and displacement waveforms are both correctly retrieved, the corresponding peak amplitude parameters ( $P_d$  and  $P_v$ ) follow a similar decay law with magnitude and distance, so that their ratio is expected to vary in a predetermined range. With this in mind, the real-time measurement of anomalous  $P_d/P_v$  values can be symptomatic of a noisy data processing, with consequent wrong measurement of the initial parameters. Depending on the  $SNR$  and on the  $P_d/P_v$  ratio, two different filters can be applied to obtain a clean waveform (see supplementary material for further details), or data are eventually discharged if the quality control is failed. All of these quality controls and the selection of the appropriate filtering are necessary for the correct estimation of EW parameters and to improve the reliability of the information released by the system. Indeed, especially in cases of small magnitude or far distant events, both the P-peak amplitude and characteristic period/frequency are likely hampered by noise at low frequencies [Shieh *et al.*, 2008], especially when derived by double-integrated acceleration signals.

The methodology is based on the joint estimate of the peak displacement ( $P_d$ ) and the period parameter  $\tau_c$ , which is defined as (Kanamori, 2005):

$$\tau_c(to) = 2\pi \sqrt{\frac{\int_0^{to} u^2(t)dt}{\int_0^{to} v^2(t)dt}} \quad [1.1]$$

Where  $u$  and  $v$  are respectively the ground motion displacement and velocity recorded at the site. The logarithm of this quantity is closely correlated to the moment magnitude of the source.

The velocity and displacement are respectively estimates through a single and double integration of data using time windows of 1, 2 and 3 seconds after the P-wave arrival time. The predominant period of the signal theoretically depend only from the size of the fault. The higher length of the source due the low frequency content of the recorded signal and consequently a higher value of predominant period.

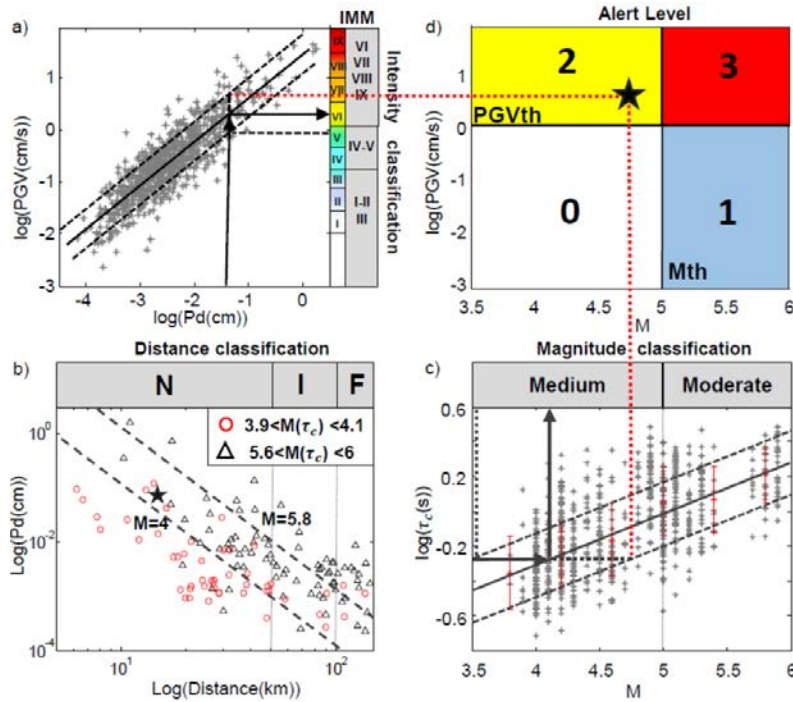


**FIGURE 1.3: OUTPUT OF SAVE.** (a) Scaling relationship between  $Pd$  (3 seconds of PTW) and PGV for the estimation of Intensity. Example of  $Pd$  estimate (black arrow), for which the algorithm provides as output a moderate intensity [VI-V]. (b) Two sets of data with different ranges of magnitude (estimated through  $\tau_c$  on 3 a second PTW) respectively [3.9-4.1] and [5.9-6.1]. The dashed lines show equation (9) at a fixed magnitude of 4 and 5.9. (c) Scaling relationship between  $\tau_c$  (3

seconds of PTW) and  $M_w$ . Example of magnitude estimate (black arrow), for which the algorithm classifies the event as a medium size earthquake [ $M_w$ 3-5]. (d) The system provides an alert level using the decision table [Zollo *et al.*, 2010].

Once the preliminary check of data quality is done and the appropriate filter is selected, for each time window,  $P_d$  and  $\tau_c$  are measured on the vertical component of displacement waveforms and are used to predict the output parameters (see the scheme in Figure 1.1). However, depending on the filter adopted, different outputs can be computed. In particular, when a 0.075 Hz filter is used, both  $P_d$  and  $\tau_c$  are measured and used for the estimation of instrumental intensity, magnitude, distance and the alert level. When the 1 Hz, high-pass filter is used, instead, only  $P_d$  is measured and used for the intensity prediction, being the relationship  $\tau_c$  vs Magnitude very poorly constrained with this filtering.

Considering the uncertainties associated to each estimated parameter, SAVE does not provide all the punctual output values, but it rather provides output parameters through a simplified classification scheme. The Instrumental Intensity ( $I_{MM}$ ) is derived by the conversion of Peak Ground Velocity (PGV) using the scale proposed by *Faenza and Michelini* [2010] and is classified in three class of perceived shaking: *Light* (if the intensity predicted is < III), *moderate* (if the intensity predicted is in the range IV-V) and *strong* (if the intensity predicted is upper than V) ([a] Figure 1.3). The setting of all classification intervals is based on the uncertainties of the empirical laws. Also for the earthquake magnitude and the source-to-receiver distance, both parameters may suffer for large uncertainties, which reflect the scattering of data of the empirical scaling relationship. Based on the standard error of equations (1.2-1.4) and (1.5-1.7) (next section), the on-site estimates of moment magnitude and distances are provided in the form a simplified classification scheme (Figure 1.3b & Figure 1.3c). In particular, the earthquake size is classified into *small* (if the predicted magnitude is < 3), *medium* (events with predicted magnitude in the range 3-5), *moderate* (events with predicted magnitude in the range 5-6.5) or *large-to-very large* event (if the predicted magnitude is > 6.5). Similarly, for the

distance, (Figure 1.3b) the system will distinguish the case of a *near* (**N**) (when the event is expected to be at a distance  $< 50$  km), *intermediate* (**I**) (when the predicted distance is in the range 50-100 km) or *far-away* (**F**) event (with predicted distance  $> 100$  km). Finally, the alert level is computed following the conceptual scheme proposed by *Zollo et al.* [2010] (Figure 1.3d).

In the real-time system, the alert messages are sent via UDP to a list of IP addresses associated with target sites, which can be either different devices in the building to protect or different nearby facilities/users. In this case, the alarm is sent via TCP/IP to a server that acts as a “broker”, relaying the messages to any number of subscribed clients. The graphical output of the system is composed by a display, that is intended to provide a visual feedback of the status of SAVE to bystanders and administrators at the target site. In case of a seismic event, SAVE can provide a readable summary of the outputs of the system, which is also sent to remote users by mail.

### **1.3 Application and results**

In this section, we present a statistical evaluation of the system performance using the Italian strong motion data. The database used consists of 128 Italian earthquakes (Figure 1.4), with moment magnitude ranging between 3.5 and 5.9 recorded at hypocentral distance between 10 and 200 km. We divided the dataset into two subsets, having approximately similar distribution in both distance and magnitude. We used the first group of data to estimate  $P_d$  and  $\tau_c$  over the time windows of 1, 2 and 3 seconds, in order to calibrate the empirical scaling relationships between the EEW parameters and PGV, magnitude and distance. The second set of data was used instead for testing the performance of the EW platform SAVE.



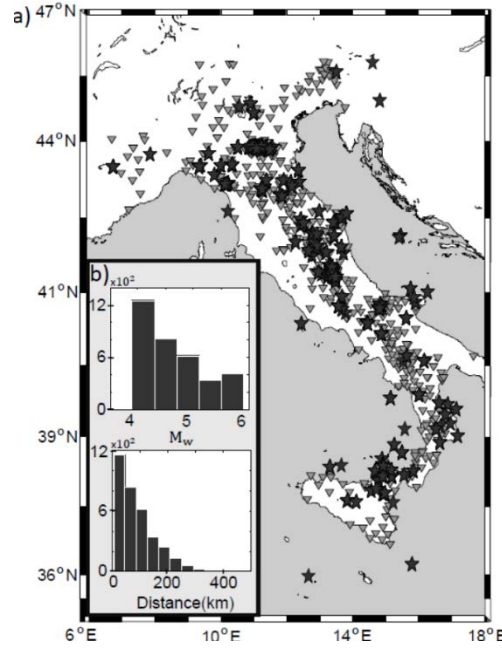


**Figure 1.4: DATA.** (a) Epicentral locations of the 128 earthquakes (black stars) and of the stations of the RAN (gray triangles) used for the analysis. (b) Histograms of the magnitude and distance distributions of the analyzed records.

We determined the empirical scaling relationships  $PGV$  vs  $Pd$  for each combination of cut-off filter (0.075Hz or 1 Hz) and P-wave time window (1, 2, 3 sec). For simplicity, we provide here only the scaling relationships for the 0.075 Hz filter, for both 1,2 and 3 seconds, while the corresponding relationships for the 1Hz filter are provided in the figure 1.5). Measuring  $Pd$  in centimeters and  $PGV$  in centimeters per seconds, we found:

$$1\text{ s} \rightarrow \log(PGV) = 0.62(\pm 0.05)\log(Pd(1)) + 0.51(\pm 0.14)\sigma: 0.37; \quad (1.2)$$

$$2\text{ s} \rightarrow \log(PGV) = 0.69(\pm 0.04)\log(Pd(2)) + 0.58(\pm 0.10)\sigma: 0.36; \quad (1.3)$$

$$3\text{ s} \rightarrow \log(PGV) = 0.69(\pm 0.04)\log(Pd(3)) + 0.51(\pm 0.10)\sigma: 0.36; \quad (1.4)$$

Similarly, by measuring  $\tau_c$  in seconds and using the moment magnitude ( $M_W$ ), we found:

$$1\text{ s} \rightarrow M_{w1}(\tau_c) = 4.36(\pm 3.44)\log(\tau_c(1)) + 5.38(\pm 0.75)\sigma: 0.21; \quad (1.5)$$

$$2\text{ s} \rightarrow M_{w2}(\tau_c) = 3.34(\pm 0.83)\log(\tau_c(2)) + 5.12(\pm 0.18)\sigma: 0.15; \quad (1.6)$$

$$3\text{ s} \rightarrow M_{w3}(\tau_c) = 3.39(\pm 0.81)\log(\tau_c(3)) + 5.04(\pm 0.17)\sigma: 0.14; \quad (1.7)$$

Then, with the aim to infer a rapid, but approximate, estimation of the source-to-receiver distance, we derived the following scaling relationships between the  $Pd$ ,  $M_w(\tau_c)$  and the hypocentral distance ( $R$ ), measured in km:

$$1 \text{ s} \rightarrow \log(R) = -0.30(\pm 0.04) \log(P_d) + 0.14(\pm 0.03) M_{w1}(\tau_c) + 0.18(\pm 0.17) \quad \sigma: 0.28; \quad (1.8)$$

$$2 \text{ s} \rightarrow \log(R) = -0.32(\pm 0.03) \log(P_d) + 0.22(\pm 0.02) M_{w2}(\tau_c) - 0.17(\pm 0.15) \quad \sigma: 0.28; \quad (1.9)$$

$$3 \text{ s} \rightarrow \log(R) = -0.33(\pm 0.03) \log(P_d) + 0.21(\pm 0.02) M_{w3}(\tau_c) - 0.14(\pm 0.14) \quad \sigma: 0.27; \quad (1.10)$$

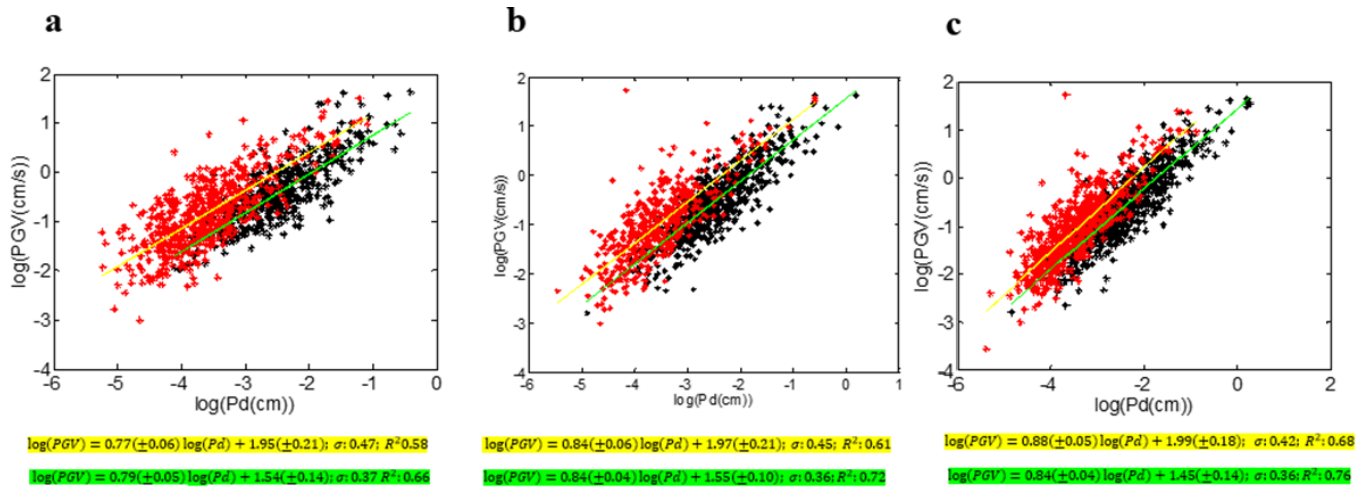


**Figure 1.5: PGV VS  $Pd$  CALIBRATION.** The figure shows the PGV vs.  $Pd$  data, estimated in three different P-wave Time windows (PTWs) of 1 (a), 2 (b) and 3 (c) seconds respectively after the arrival time of the P-wave, for the two different filters. Red points are the data filtered with a 1-20 Hz band pass filter, while black points are data filtered with the 0.075-15 Hz band pass filter. Yellow and green lines are the best-fit regression relationships for the red and black data, respectively. The comparison between the two linear regression relationships shows a systematic difference on the estimation of  $Pd$ , which is due to the filtering operation. Both filters, however, preserve the scaling between the two parameters.

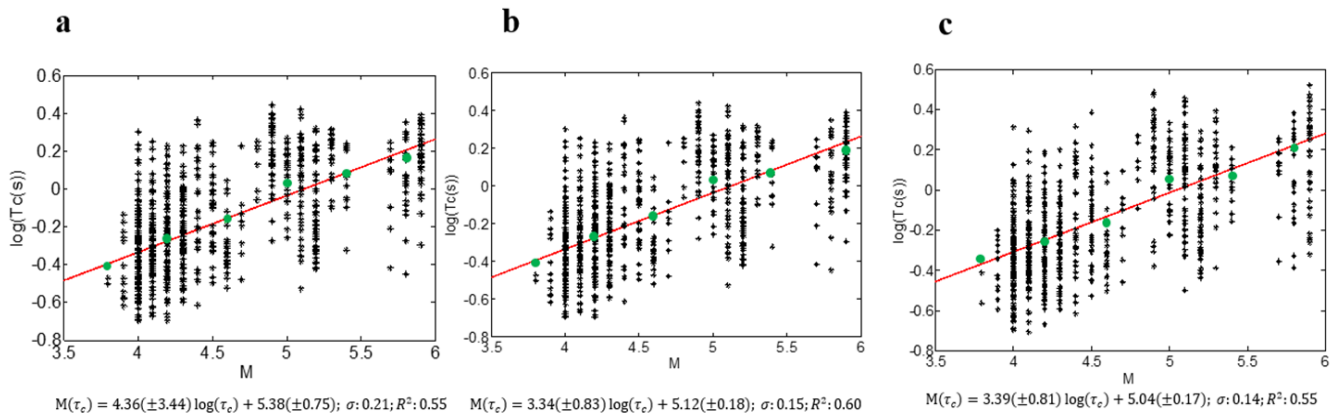


**Figure 1.6: M VS TC CALIBRATION.** The figure shows the three different relationships between the *Moment Magnitude* and  $\log(\tau_c)$  estimated using a PTW of 1 (a), 2 (b) and 3 (c) seconds. Since the data are not equally distributed in all magnitude ranges, we binned data with a step of 0.4 in magnitude and computed the mean value of  $\log(\tau_c)$  associated to the central value of magnitude in each bin (green point). The red solid line is the best fit regression line, using the mean values of  $\log(\tau_c)$ .

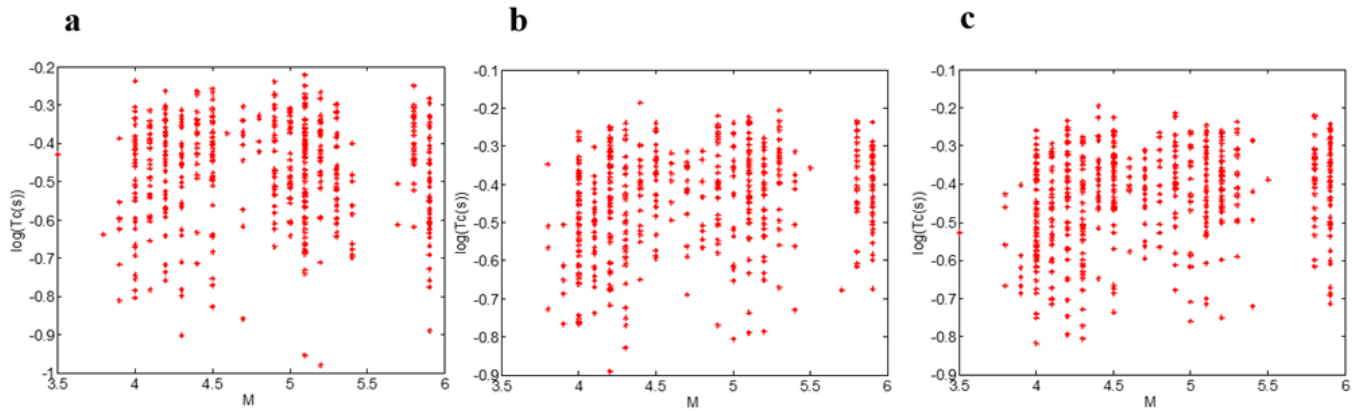


**Figure 1.7: M VS TC OF LOW QUALITY DATA.** The figure shows the  $\log(\tau_c)$  vs *Moment Magnitude* estimate on the data filtered by [1 20] Hz band pass filter after 1 (a), 2 (b) and 3 (c) seconds after the arrival time of the P wave. The scaling with magnitude is rather poor, as confirmed by the almost zero-slope of the resulting linear fit function.

We note that the correlation laws derived for Italy are different from those estimated for other seismotectonic areas, (i.e., Japan, *Colombelli et al.*, [2012]). For this reason, a local calibration is necessary in order to improve the reliability of the system.

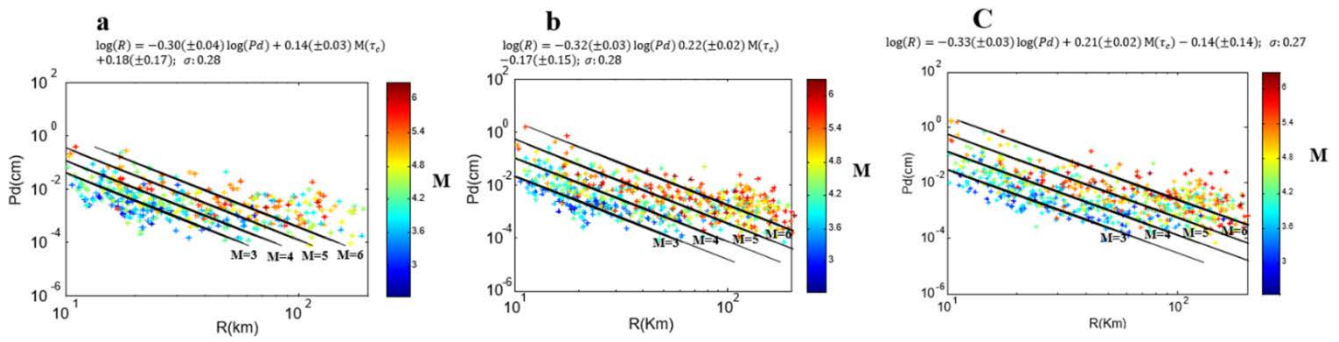


**Figure 1.8: R VS ( $P_d$ ; M).** The figure shows the empirical scaling relationship between  $P_d$  (measured in cm), event magnitude  $M$  (as obtained from  $\tau_c$ ) and hypocentral distance  $R$  (in km). The figure also shows the best fit lines of  $P_d$  vs.  $R$  (in log-log scale), for different fixed magnitude values (3, 4, 5, 6). The regression relationships are estimated for data measured at 1 (a), 2 (b) and 3 (c) seconds after the arrival time of the P-wave. The plot clearly shows the overestimation of the  $P_d$  values recorded at distances greater than 100 km, resulting from the effect of the double integration of data with low signal-to-noise ratio.

After calibrating the empirical scaling relationships using the first data-set, we applied the methodology to the remaining dataset, including only data that were not used for the calibration phase. To evaluate the performance of the system, we compared the output predicted by SAVE with the real parameter values, by using the classification scheme.

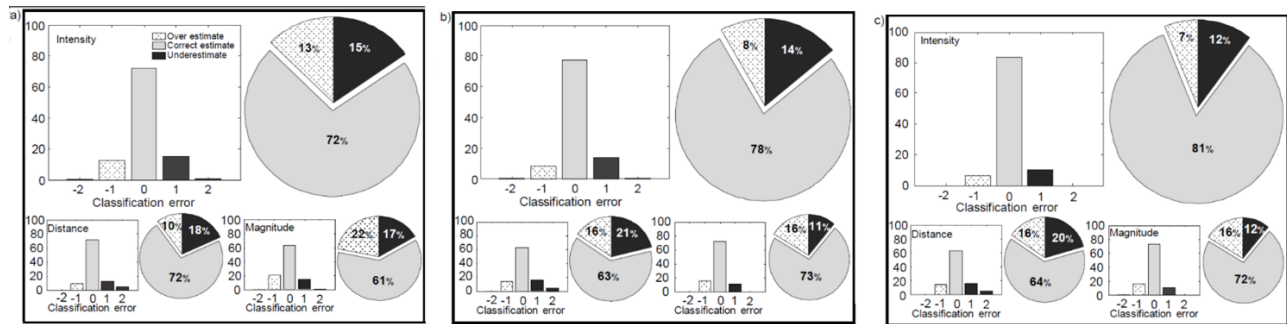


**Figure 1.9: RESULT.** Histograms of the difference between the real and predicted classification of the output parameters. The pie-graph represents the corresponding percentage of correct, underestimated, and overestimated classifications. The performance is evaluated for (a) 1 second, (b) 2 seconds and (c) 3 seconds after the P arrival.

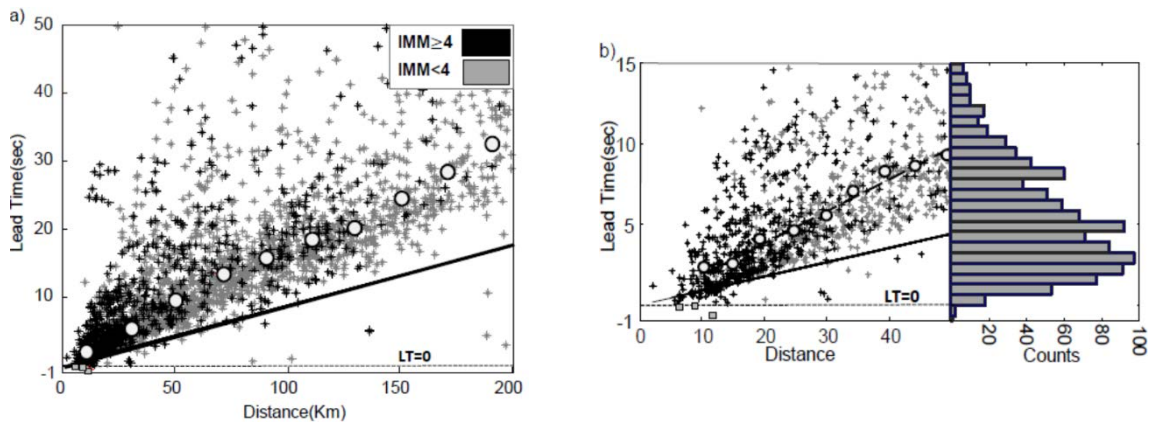


**Figure 1.10: Lead-Times.** Panel (a) shows the LT at different distances for all the data used for testing. The gray circles are the median values at different distances using binned data (bin of 10 km) and the solid line is the theoretical arrival time of the S wave. Panel (b) is the same plot as shown in panel (a) but limited to 50 km (the bin used for median values is 5 km) with the corresponding histogram of the LTs and the dashed line is the best fit of the median values. The gray squares are the negative LTs.

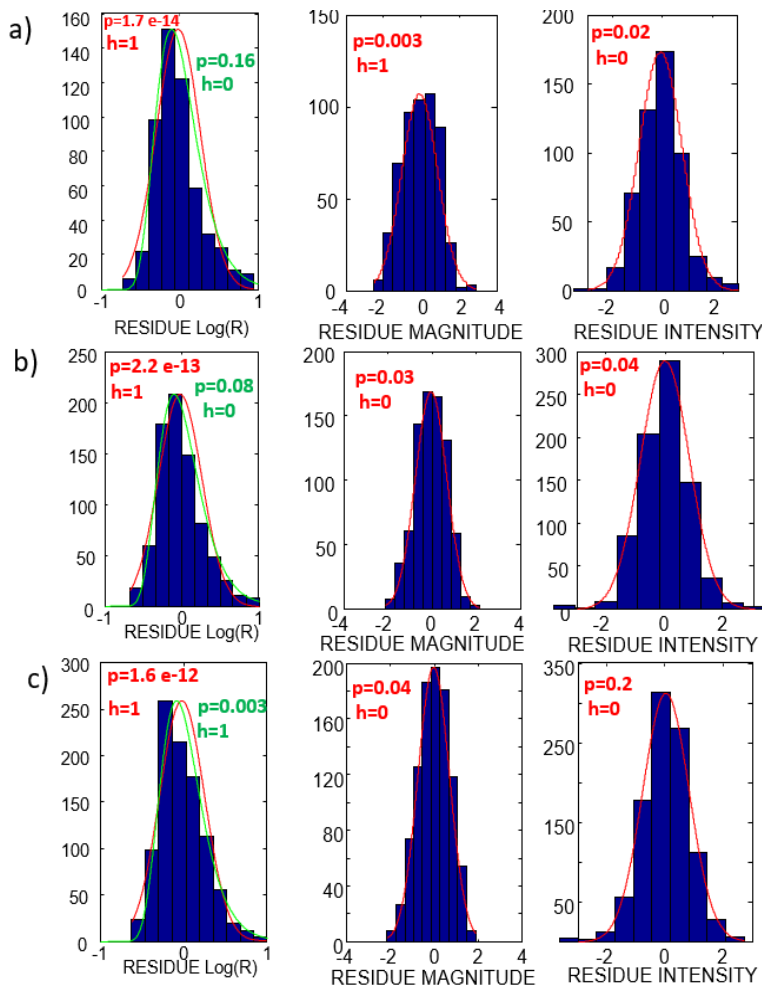


**Figure 1.11: ERROR DISTRIBUTION.** The figure shows the residual distribution of the output provided by SAVE (i.e., logarithm of distance, magnitude and intensity) at 1 (a), 2 (b) and 3 (c) seconds after the arrival time of the P-wave. Red lines show the Gaussian distribution with mean values and standard deviation of data, while green lines are the log-normal distributions. On each plot, the “h” value shows the decision test for the null hypothesis of a normal distribution (and log-normal in green, respectively), while the “p” value is the probability value. A value of  $h = 0$  indicates that the null hypothesis at the 1% significance level ( $p \geq 0.01$ ) is not rejected. Unlike magnitude and intensity histograms, the histogram of the distance classification is actually far from being a Gaussian distribution, but it rather it is consistent with a log-normal distribution, with a tail at the positive side of the distribution. This has a double origin. The first one is that data at large distances ( $> 50$  km) generally have a low signal-to-noise ratio (especially within 1 and 2 seconds of P-wave time windows). Furthermore, the low frequency noise is amplified by the double integration process and may dominate the signal, resulting in an overestimation of the peak displacement amplitudes and dominant periods. The second reason for a non-Gaussian distribution is that

data recorded near the source (distances  $< 20$  km) within three seconds of PTW may include the S waves, so that both  $Pd$  and  $\tau_c$  parameters might be overestimated again.

Figure 1.11 shows the histogram of the residual between the real and predicted intensity, magnitude and distance class, for a P-wave time window of one (Figure 1.9a), two (Figure 1.9b) and three (Figure 1.9c) seconds. The histograms show the percentage of over, under and correct estimated classifications. For intensity, the most populated bin is around zero, with more than 80% of successful predictions and a small percentage of values in the adjacent classes ( $\pm 1$ ). For magnitude and distance, the residues have a Gaussian-like distribution, centered around zero, with more than 60-70% of successful predictions.

## 1.4 Discussion

In the present chapter we introduced a methodology for an onsite, single station, EWS, denoted as SAVE (onSite Alert leVEl) and based on the real-time, evolutionary measurement of the P-wave peak amplitude and characteristic period, as acquired by one or more co-located sensors. The methodology we developed is able to provide a reliable, although first order, evaluation of the main source parameters, and this undoubtedly represents a significant improvement for standard on-site EWS approaches, for which the information about the earthquake source is absent or extremely unreliable.

SAVE has been tested off-line using a dataset of moderate-to-strong Italian earthquakes (M from 3.5 to 6) and the overall performance is shown in the histograms of Figure 1.9. In term of prediction error, the expected intensity is the most reliable parameter, with more than 80% of successful predictions, yet 1 second after P-wave arrival.

The robustness of the ground shaking prediction undoubtedly represents the most important feature for the decision-making processes of the end-user audience, especially for an on-site system, where no further information on the earthquake source is available.

As for magnitude and distance parameters, both quantities may suffer for large uncertainties, which

reflect the scattering of data, during the calibration of the empirical scaling relationships (eqs. 1.5 to 1.10). The earthquake magnitude, indeed, is estimated through the average period, which is known to be largely scattered and to represent a robust magnitude proxy only when averaged over many stations [Zollo *et al.* 2006, Colombelli *et al.* 2012]. The source-to-receiver distance is obtained from the theoretical scaling between the observed P-wave amplitude with magnitude and distance and the empirical scaling relationship is generally affected by large data scattering. This is the reason why both the earthquake magnitude and the source-to-receive distance are provided in the form of simplified ranges, rather than with their punctual values. For both parameters, the real-time predictions are correctly provided in most of the cases, as confirmed by the histograms of residuals, which are distributed around zero and with a Gaussian-like shape.

In a stand-alone EWS, where no information about the earthquake location is available, a possible risk is the inclusion of S-waves in the analyzed P-wave time window, which may lead to an overestimation of the predicted ground shaking level. To minimize the S-wave contamination, SAVE currently uses the vertical component of ground motion recordings only.

The graphical output of SAVE is composed by a display which provides a visual feedback of the status of the system at the target site. The display is not intended as a means to prompt people to action. The decision on whether and how to initiate safety measures is still demanded to the recipients of alert messages sent to individual systems or broadcast by SAVE through internet. However, SAVE can be easily connected to an automatic interface, which is able to receive the warning and activate security actions. Within this context, the rapidity and robustness of the system represent ideal features for the immediate activation of emergency operations.

Figure 1.10 shows the lead-time as a function of distance, for all the available data (gray dots) and for the highest observed intensities (black dots). The lead-time is computed as the difference between the arrival time of the maximum shaking amplitude (i.e., PGV) and the warning time (i.e., 1 second after

the P-wave detection). In order to have a statistical estimation of LT for each value of distance, the lead-time are

subdivided in several a number of intervals (the bin used is 10 km for [a] and 5km for [b]) and, for each of them, we have calculated a statistical representative value (gray circles). Since the data do not have a Gaussian distribution, we have selected the median as representative value of statistical distribution. As expected, the lead-time increases with distance, with a value of 8-10 seconds at 50 km, 15-18 seconds at 100 km and more than 20 seconds at 150 km. The occurrence of PGV may not correspond to the occurrence of structural building collapse in more cases, for this reason the LT have a probabilistic sense but the effective LT can be more or less of it. The figure also shows the theoretical arrival of the S-waves as a function of distance (gray, solid line). For small distances (< 50km), the arrival of the strongest shaking coincides mostly with the expected arrival of the S-wave, but at larger distances, the strongest shaking arrives later in time, probably due to the arrival of later phases.

Assuming the RAN network stations distribution over the Italian territory, the feasibility study for a regional EEWS performed by *Picozzi et al.*, [2015] showed that the first alert time would be available around 4 and 5.5 s in the highest seismic hazard areas assuming three and six triggered stations, respectively. Furthermore, the blind zones in these areas have radii of about 25 and 30 km when three and six stations have triggered, respectively.

As a further example, *Picozzi et al.*, [2015] performed a scenario analysis of the 1980 Irpinia earthquake (Ms 6.9) [*Bernard and Zollo*, 1989], considering the actual RAN configuration with respect to the observed macroseismic field after this event [*Guidoboni et al.*, 2007; *Locati et al.*, 2011, data available from <http://emidius.mi.ingv.it/DBMI11/>]. Keeping into consideration only the municipalities to which it was assigned a macroseismic intensity IMCS equal or larger than VII (i.e., from moderate toward very high damage), they observed that 35 municipalities fell within the BZ; 53 had lead times (LT) less than 5 s; 73 had LT between 5 and 10 s; 112 had LT between 10 and 20 s; and finally, 24 had



more than 20 s of LT.

For an on-site system like SAVE, the most relevant issue is the reduction of the blind zone and the increase of the lead times, for the effective protection of the target sites in the source area, or at a small distances from it. The bottom plot of Figure 1.10a shows a zoom on the lead-times for small epicentral distances ( $< 50$  km). About 3 seconds of lead-time would be available at a distance of 20 km, 5-6 seconds would be available at a distance of 30 km and 7-8 seconds at 40 km. In terms of practical applications, this result is extremely important, since it allows speeding up the warning declaration, with a consequent increase of the available lead-time at the site. Furthermore, if the station is the node of a network, the proposed approach would significantly reduce the radius of the BZ.

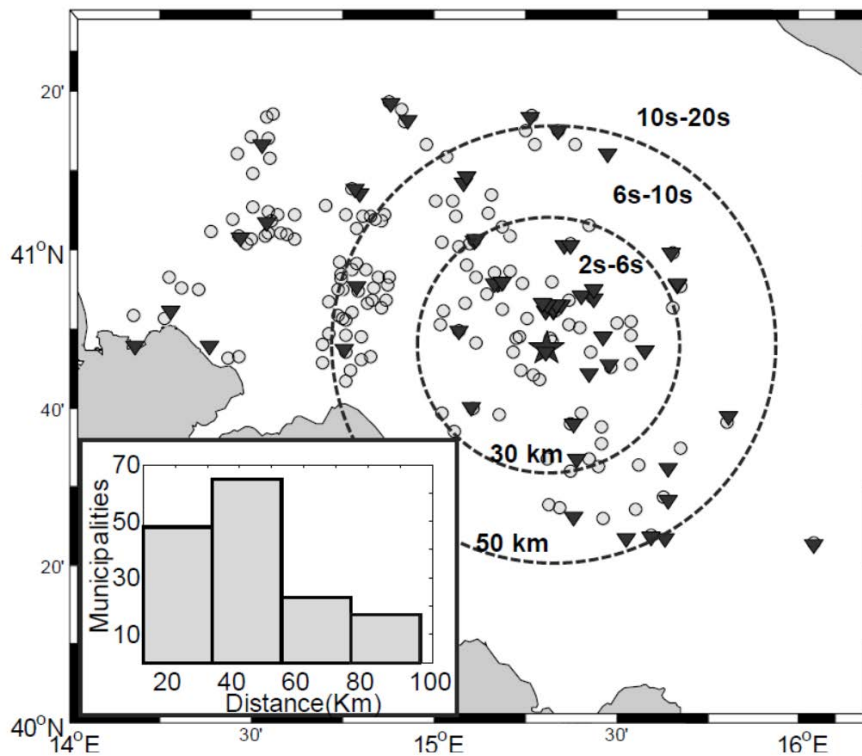


**Figure 1.11: SCENARIO OF THE IRPINIA EARTHQUAKE.** The figure shows the scenario case of the 1980 Irpinia earthquake. Black, inverted triangles show the stations used for the analysis, while the grey dots are the municipalities. The dashed lines show the epicentral distances of 30 and 50 km, with the corresponding LT range. The insert panel shows the histogram of the number of alerted municipalities, as a function of distance.

As an example, let us consider again the scenario analysis of the 1980 Irpinia earthquake ( $M_s$  6.9)

[*Bernard and Zollo, 1989*] and the municipalities with an assigned a macroseismic intensity IMCS [*Guidoboni et al., 2007; Locati et al., 2011*, data available from <http://emidius.mi.ingv.it/DBMI11/>] equal or larger than VII. If SAVE had been operative at each station of the RAN network, assuming that the alert was delivered in a range of 8 km around the station and that the BZ of the regional EEWS had a radius of 20 km [*Picozzi et al., 2015*], the number of municipalities that could not benefit from the warning would have been reduced to 85%. At the same time 48 municipalities would have had lead times (LT), according to the fit in figure 6, between 2 and 6 s (hypocentral distance between 10 and 30 km); 53 had LT between 6 and 10 s (distance between 30 and 50 km); and finally, 55 municipalities had LT between 10 and 20 s (distance between 50 and 100km) (Figure 1.11).

In its current configuration, SAVE is conceived and optimized to be used as a stand-alone system for a specific target site (i.e., a single sensor located at the target site or a small set of co-located seismic nodes), where no communication and exchange of information with other monitored targets is possible.

# **Chapter 2: On-site Early warning Systems and a P-wave based approach**

## **2.1 Introduction**

In this chapter, we introduce an innovative methodology for an on-site Earthquake Early Warning System. In order to have a reliable alert we have perform a robust algorithm based on the correlation between the P-wave amplitude and maximum intensity occurred at site. The robustness is increased using the P-wave amplitude measured on the acceleration, velocity and displacement vertical component. The three parameters are correlated because are derived by the same earthquake source and measured in the same site but the frequency domains are completely different and the combination of these three parameters is able to give a more complete description of the earthquake phenomena. P-wave amplitude parameters are estimate on a exempling time window aimed to avoid saturation of correlation laws. The expanding time window causes the inclusion of other seismic phase due the overestimation of P-wave amplitude and consequently the false alert. To reduce this effect, in section 2.3.2 a reliable filtering algorithm aimed to select only the P-wave phase in the signal is proposed and tested.

In order to calibrate and proof this methodology, we have select a Japan and Italian data-set aimed to have a large number of waveform in a large range of magnitude and distance for the calibration of empirical laws used for the predict the local intensity. Part of database is used to testing the methodology estimating the lead-time of alert and the prediction outcome in term of successful, false and missed alert. The cumulative and Scenario test show a high rate of successful alert (more than 80%) in the most of case.

## 2.2 Methodology

The methodology proposed here is essentially based on two key elements. The first one is the joint use of three peak amplitude parameters (the initial peak of displacement,  $P_d$ , velocity,  $P_v$ , and acceleration,  $P_a$ ), which are continuously measured along the vertical component of ground motion recordings. The second key element of the proposed methodology is an empirical combination of the three ground motion parameters and its use as a proxy for the ensuing Peak Ground Velocity (PGV) at the same site (Wu & Kanamori, 2005; Wu & Kanamori, 2008; Zollo et al., 2010).

In standard approaches to EEW, limited time windows (2-3 seconds) are generally used to measure the ground motion parameters for the rapid characterization of the ongoing earthquake. In case of very large events such short PTWs are not enough wide to properly characterize the source process, resulting in a significantly lower estimate of the earthquake size (Colombelli et al., 2012b; Colombelli et al., 2014). Following the concept of the expanded P-wave Time Window (PTW), here the real-time measurements are progressively measured starting from the P-wave onset time and continuously updated as long as the ground motion is recorded. At each time along the seismogram, the observed  $P_d$ ,  $P_v$  and  $P_a$  parameters are measured and compared to prior established threshold values. The threshold values have been defined through the empirical correlations between  $P_d$  ( $P_v$  and  $P_a$ ) and the final PGV for a given instrumental intensity (IMM, based on the PGV-to-IMM conversion table of Wald et al., 1999) and accounting for the estimated  $1-\sigma$  error bounds on the PGV versus  $P_d$  ( $P_v$  and  $P_a$ ) relationship.

Once compared to the threshold values, each observed parameter is then converted into dimensionless fuzzy variables, denoted as  $W_d$ ,  $W_v$  and  $W_a$ , for  $P_d$ ,  $P_v$  and  $P_a$ , respectively, following the scheme:

$$\begin{aligned}
W_x(t) &= 0 && \text{if } P_x(t) < P_{xL} \\
W_x(t) &= 1/3 (P_x(t) - P_{xL}) / (P_{xH} - P_{xL}) && \text{if } P_{xL} \leq P_x(t) \leq P_{xH} \\
W_x(t) &= 1/3 && \text{if } P_x(t) > P_{xH}
\end{aligned}$$

where the subscript  $x$  stands for displacement ( $d$ ), velocity ( $v$ ) or acceleration ( $a$ ), respectively, and  $P_{xL}$  and  $P_{xH}$  indicate the lower and higher threshold values for the parameter  $x$ .  $W_x(t)$  is computed at each time and is locked at the corresponding value until a larger value is encountered. As a result,  $W_x(t)$  is a monotonically increasing step-ladder like function, as shown in Figure 2.1d. We then sum up the values of  $W_d$ ,  $W_v$  and  $W_a$  to define a single logical variable  $W_t$ , which is now used for warning declaration (Figure 1a, bottom plot). Instead of using one parameter with a single preset threshold, here we are combining three ground motion parameters, accounting for the uncertainty of the empirical scaling relationships. The use of the fuzzy variable is a simplified, although arbitrary, way to convert a single-parameter, binary, decision scheme into a multi-variable, continuous, alert system. With the proposed definition of  $W_d$ ,  $W_v$  and  $W_a$ , the three ground motion quantities equally contribute to the final shaking prediction.

To define the thresholds for warning, we converted a given instrumental intensity (IMM) to PGV [Wald *et al.*, 1999] and extracted the values of  $P_d$ ,  $P_v$  and  $P_a$  associated to such a PGV value, through empirical correlations between these three parameters and the PGV (see Figure 2.1 panels b,e and f).

We used two intensity levels IMM=V, (i.e, PGV = 3.4 cm/s) and IMM=VII (i.e, PGV = 16 cm/s), which correspond to the “light-to-moderate” and “strong-to-very strong” transitions on the perceived shaking and on the produced damage [Wald *et al.*, 1999, table description]. For each intensity threshold value, the threshold values on the amplitude parameters are obtained from intersections of the threshold PGV with the empirical correlations plus/minus 1 standard deviation (Figure 2.1b, e, f). For the derivation of the empirical scaling relationships, we avoided the S-wave contamination by terminating

the time window for  $Pd$ ,  $Pv$  and  $Pa$  measurement at the expected arrival of the S-waves. The expected S-wave arrival time at each station ( $T_s$ ) is computed using the following relation:

$$T_s - T_p = b * R \quad [3.1]$$

where  $T_p$  is the observed P-wave onset time,  $R$  is the hypocentral distance and  $b = 0.088$  sec/km. The coefficient  $b$  has been derived by a linear regression analysis, after manually picking the S-wave arrival times for a selected number of records in the data-set and reducing the  $T_s - T_p$  time by 30% to ensure that the probability of including the S wave is very small.

In terms of output of the system, the definition of a threshold value on  $W_t$  identifies four different alert categories, whose order here intuitively reflects the increasing probability of alert failure (see PGV vs.  $W_t$  diagram in Figure 2.2): successful alarm (dark green zone), successful no-alarm (light green zone), false alarm (yellow zone) and missed alarm (red zone). The threshold value of  $W_t$  along the PGV vs.  $W_t$  plot controls the overall performance of the system, with an intrinsic trade-off between false and missed alerts (Figure 2.1d). High values of  $W_t$  generally provide a small number of false alarms but may frequently generate missed alarms. On the contrary, small values of  $W_t$  are expected to reduce the missed alerts, but consequently increase the occurrence of false alarms. After analyzing the number of missed, false and successful alarms as a function of  $W_t$ , for the present analysis the value of  $W_t$  was fixed in order to maximize the total percentage of successful alarms.

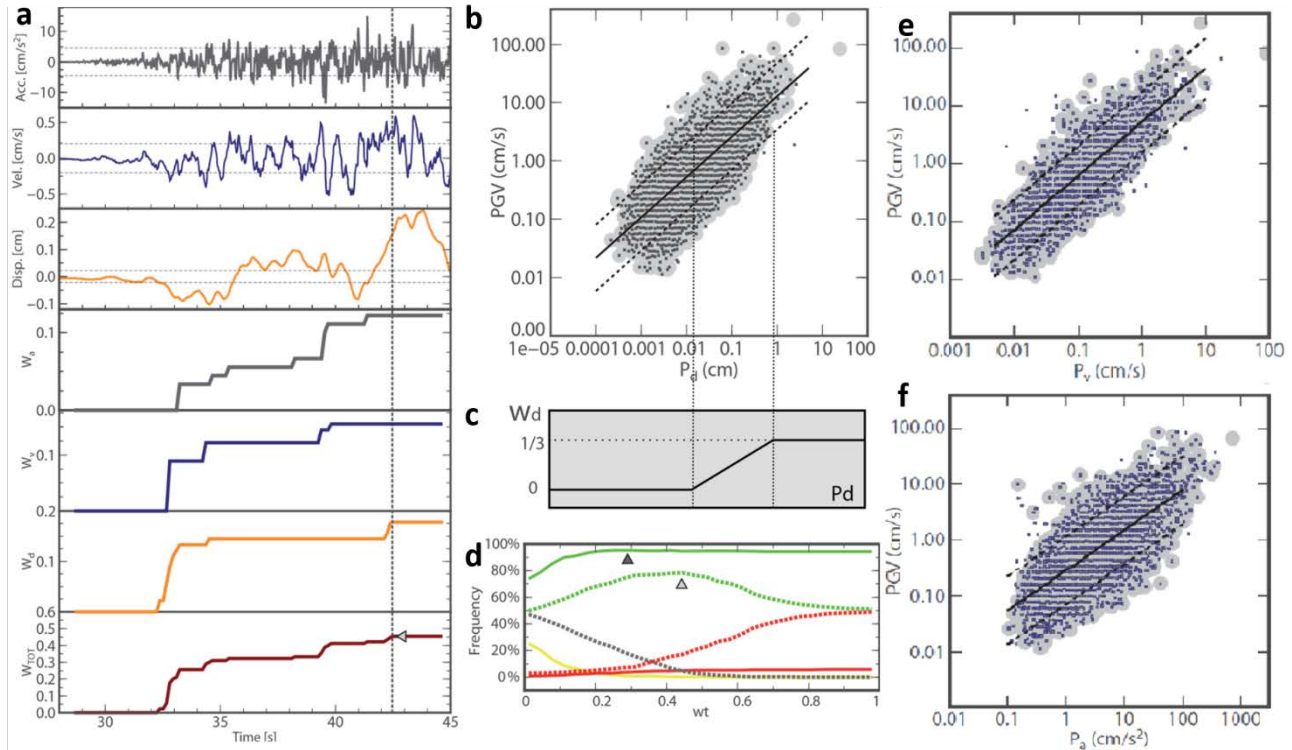


**FIGURE 2.1: METHOD AND EMPIRICAL CORRELATIONS:** In panel (a) from top to bottom, an example of the vertical component of acceleration (black), velocity (blue), and displacement (orange) signals. The initial peak amplitude parameters  $P_d$ ,  $P_v$ , and  $P_a$  are measured as the absolute maximum of displacement waveform on the early portion of P wave. The threshold values (for the intensity IMM = V) on each parameter are schematically shown as a black, dashed line on each record. Examples of  $W_a$ ,  $W_v$ , and  $W_d$  as a function of time are also shown with a solid black, blue, and orange lines, respectively. Each step on  $W_a$ ,  $W_v$ , and  $W_d$  corresponds to an increase of the peak amplitude parameters (as absolute value) on the ground motion records. Finally, the bottom plot shows the cumulative logical variable  $W_t$  as a function of time (purple curve). Here the gray rotated triangle shows the threshold value  $W_t^*$  used for warning declaration ( $W_t^* = 0.45$ , in this case). (b, e, f) Data distribution and empirical relationships between respectively  $P_d$ ,  $P_v$ ,  $P_a$  and PGV. The background, gray circles represent the whole data set, while the small, blue and black squares are data used for calibrating the scaling relationships. Solid black lines are the best-fit lines while dashed lines are the standard error bars. (c) Example of  $W_d$  definition. The observed  $P_d$  parameter is compared to its threshold value and converted into a dimensionless variable, named  $W_d$ , which is equal to 0 in the region below the lower threshold to  $1/3$  in the region above the higher threshold and linearly increases between 0 and  $1/3$  in the intermediate region. (d) Calibration curves: the figure shows the number of MA (red line), FA (yellow line), and total successful alarms (including SA and SNA, green line) as a function of  $W_t$ . The solid lines are referred to the higher-intensity threshold (IMM = VII), while the dashed lines are associated to the lower intensity threshold (IMM = V). The threshold values of  $W_t$  are marked as a triangle on the successful alarm curves (light gray for the lower intensity and dark gray for the higher-intensity threshold).

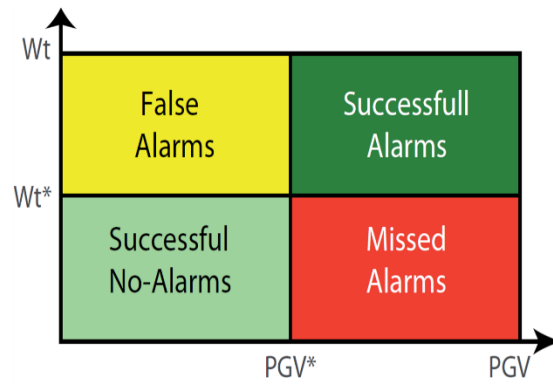


**FIGURE 2.2: PREDICTION OUTCOME TABLE:** Predictive categories provided by the system in function of Wt and PGV thresholds.



## 2.3 Test and performance

### 2.3.1 Application to the Japanese data-set

The database we used consists of 76 Japanese events in the magnitude range  $4.0 \leq M \leq 9.0$ . Among them, 73 events were used for deriving the empirical correlations and for setting the threshold values, and 3 earthquakes were used for validation and scenario studies. For each event, we selected the three-component, strong-motion accelerometer records, available in the distance range  $R$  0-500 km, for a total of 12,792 three-component records.

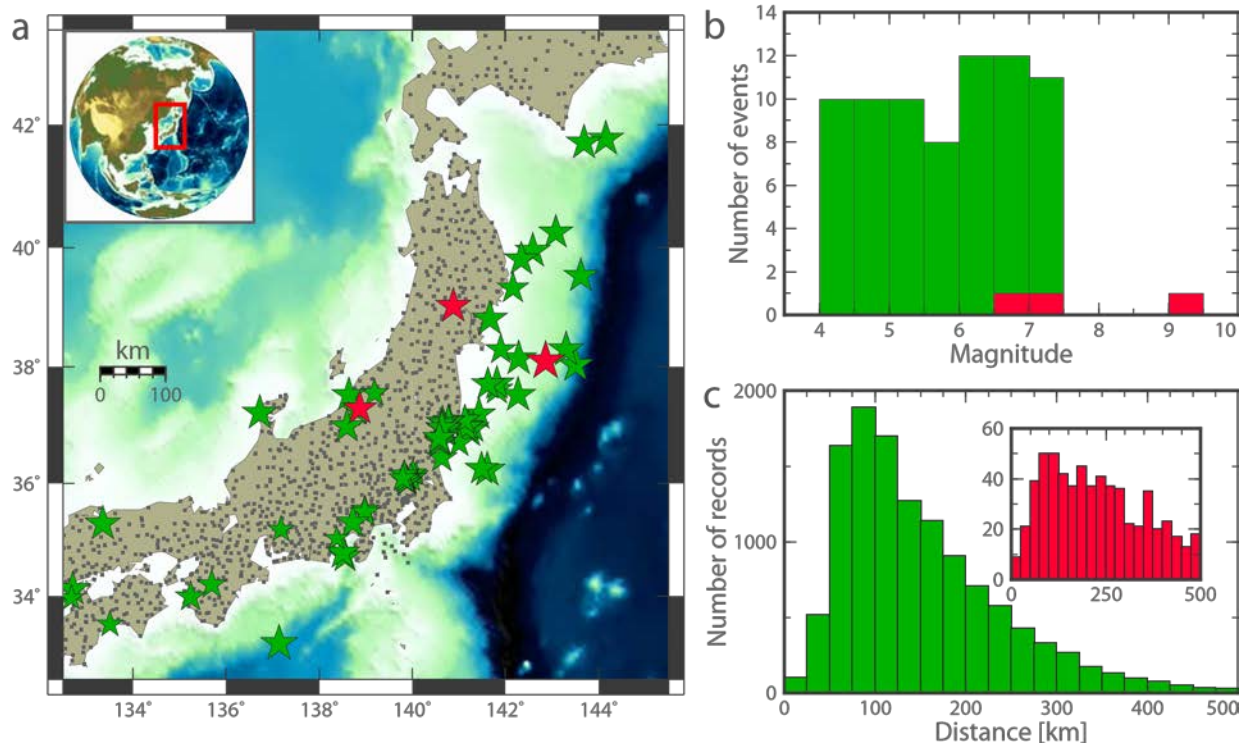


**FIGURE 2.3: DATA-SET DESCRIPTION.** (a) The map shows the distribution of stations (gray dots) and the epicentral location of the selected events. Green stars are the earthquakes used for the calibration, while red stars are the scenario events. The size of the star is proportional to the magnitude. (b) Histogram of the number of earthquakes as a function of magnitude, for the calibration data set (green) and for the scenario studies (red). (c) Distribution of records as a function of distance, for the calibration (green) and for the scenario events (red).

Figure 2.1a shows the distribution of selected events and used stations. Panels (b) and (c) show the magnitude and distance histograms, for the calibration and the validation dataset. The correlation laws, obtained using the calibration data-set, are:

$$\begin{aligned} \log \text{PGV}(\text{cm/s}) &= 1.11(\pm 0.08) + 0.69(\pm 0.04) \log P_d(\text{cm}), & \text{stdv} &= 0.57, \\ \log \text{PGV}(\text{cm/s}) &= 0.72(\pm 0.06) + 0.93(\pm 0.05) \log P_v(\text{cm/s}), & \text{stdv} &= 0.52, \\ \log \text{PGV}(\text{cm/s}) &= -0.55(\pm 0.05) + 0.72(\pm 0.05) \log P_a(\text{cm/s}^2), & \text{stdv} &= 0.61, \end{aligned}$$

The performance of the proposed EWS is evaluated by counting the percentage of Successful Alerts (SA), Successful No-Alerts (SNA), False Alerts (FA) and Missed Alert (MA). We tested our on-site strategy using two intensity levels, IMM=V (i.e, PGV = 3.4 cm/s) and IMM=VII (i.e, PGV = 16 cm/s), which correspond to the “light-to-moderate” transition both on the perceived shaking and on the produced damage (Wald et al., 1999, table description).

PERCEIVED SHAKING	Not felt	Weak	Light	Moderate	Strong	Very strong	Severe	Violent	Extreme
POTENTIAL DAMAGE	none	none	none	Very light	Light	Moderate	Moderate/Heavy	Heavy	Very Heavy
PEAK ACC.(%g)	<.17	.17-1.4	1.4-3.9	3.9-9.2	9.2-18	18-34	34-65	65-124	>124
PEAK VEL.(cm/s)	<0.1	0.1-1.1	1.1-3.4	3.4-8.1	8.1-16	16-31	31-60	60-116	>116
INSTRUMENTAL INTENSITY	I	II-III	IV	V	VI	VII	VIII	IX	X+

The  $W_t$  threshold used for felt and damage intensity level are 0.45 and 0.28, respectively.

Figure 2.4 shows the overall performance of the system for the two intensity levels chosen in terms of alert percentages (panels a and d) and in terms of alert and lead-times (panels b,e,c,f). For both the intensity thresholds, the joint use of  $P_d$ ,  $P_v$  and  $P_a$  significantly improves the performance of the system, as compared to the independent use of single amplitude parameters (see figure 3.8 and 3.9). With the proposed approach, was obtained a high percentage (more than 85%) of successful alerts (including both SA and SNA), a small number of false alarms (about 14%) and a very low percentage

of missed alerts (about 1%). For comparison, Figure 3.8 shows the performance of the system when the three amplitude parameters are independently used. In this case, the percentage of false alarms still remains too high (about 50%), especially for the lower intensity threshold, and therefore none of the three parameters can be considered a reliable candidate for the warning declaration.

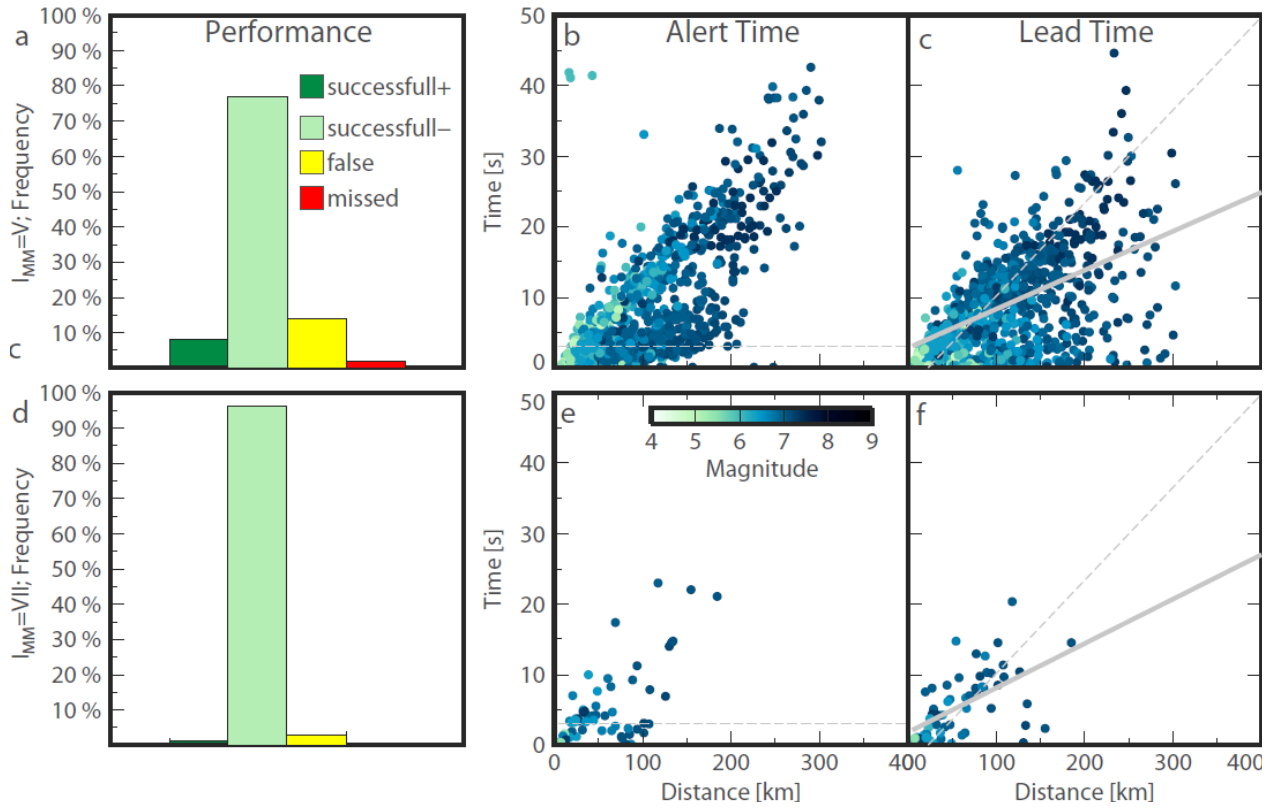


**FIGURE 2.4: PERFORMANCE EVALUATION.** Overall performance of the methodology. (a, d) The histograms show the performance of the system in terms of SA (dark green bar), SNA (light green bar), FA (yellow bar), and MA (red bar) for the two intensity levels. (b, e) Alert times as a function of distance. The black line is the theoretical alert time for the fixed PTW on-site system (3 s). (c, f) Lead times as a function of distance. The black line is the theoretical lead time for the fixed PTW on-site system (S-P arrival time difference at each site), while the green line is the best fit regression of the observed lead time as a function of distance. In Figures 2b, 2c, 2e, and 2f the color scale represents the earthquake magnitude.

Beyond the correct alert declaration, the ability to rapidly provide the warning is also a crucial feature of an early warning system. In terms of timing performances, due to the use of unlimited PTWs, the proposed approach may require longer signal portions for the warning declaration, as compared to standard on-site approaches. Nevertheless, the methodology is able to provide sufficient warning times, as illustrated in the plot of alert times and lead-times as a function of distance (Figure 2.4 b c e f). The alert time is defined as the time elapsed between the arrival of the P-wave and the alert declaration (i.e., when  $Wt$  overcomes the threshold). The lead-time is the time available from the warning declaration to the instant at which the ground velocity overcomes the threshold value (see Figure 2.1). We observed that alert times are approximately constant for small epicentral distances (a few seconds) but increase with increasing distance and magnitude (Figure 2.4 b e). Similarly, lead times also increase with distance and magnitude (Figure 2.4 c f). On average, at a distance of 100 km, the available lead-time is about 8 seconds; around 15 seconds are available at a distance of 200 km and about 25 seconds at 400 km. A deeper discussion about the timing performances is given in the Discussion section.

As a further test, the performance of the system was evaluated when limited PTWs are used, i.e., when the parameter computation is stopped at the expected arrival time of S-waves (Figure 2.8). Generally, both when the amplitude parameters are independently used, and when their combination is adopted, the use of limited PTWs reduces the number of false alarms, but a little increase of the number of missed alarms is observed (Figure 2.9). This is generally true for the overall statistics and is even more relevant for the case of single scenario events (see Figure 2.7).

We analyzed the performance of the proposed methodology for three scenario earthquake cases (Figures 2.5-2.7), which were not used to calibrate the empirical scaling relationship. We included a small-to-moderate inland earthquake (the 2004, M 6.8 Chuetsu event, Figures 2.5-2.7 a), a moderate-to-large inland earthquake (the 2008, M 7.2. Miyagi-Iwate earthquake, Figures 2.5-2.7 b), and the

offshore M 9.0 2011, Tohoku-Oki event (Figures 2.5-2.7 c). For the scenario analysis two different analysis are provided (Figures 2.5 2.7), fixing respectively threshold at damage level (IMM = VII) and felt level (IMM = V). Referring to the high threshold level, scenario cases generally confirmed the overall statistics. For the two smallest earthquakes (M 6.8 and M 7.2) we found a relatively large percentage of total successful alarms (about 70-75%), an average percentage of false alarms around 25%, and an extremely low number of missed alarms (< 2%). For the 2011, M 9.0, Tohoku-Oki

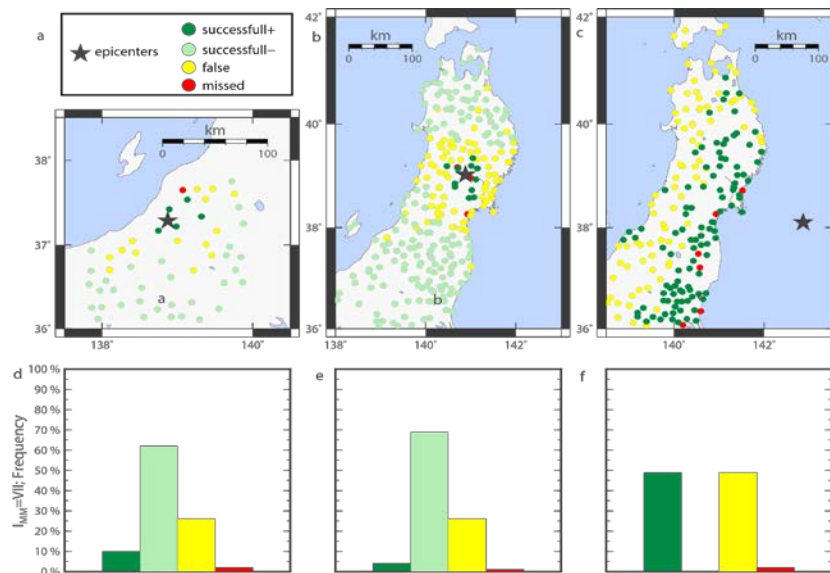


**FIGURE 2.5: SCENARIO TEST DAMGE LEVEL.** Scenario events and relative histogram of the performance, for the higher-intensity threshold (IMM = VII). Map of the alert distribution for (a) the 2004 M 6.8 Chuetsu event, (b) the 2008 M 7.2. Miyagi-Iwate earthquake, and (c) the offshore 2011 M 9.0 Tohoku-Oki event. Small colored circles represent the stations used, and the black star is the earthquake epicenter. (d–f) Histograms of the alert levels for the three scenario events. For all panels, the color scheme is the same as used in Figure 2.4 and is also explained in the legend.

earthquake, successful and false alarms are almost balanced around 49%, while the percentage of missed alarms is again very small (< 2%). Figure 2.7 shows the scenario test using the limited P-wave time window estimated using [2.1].

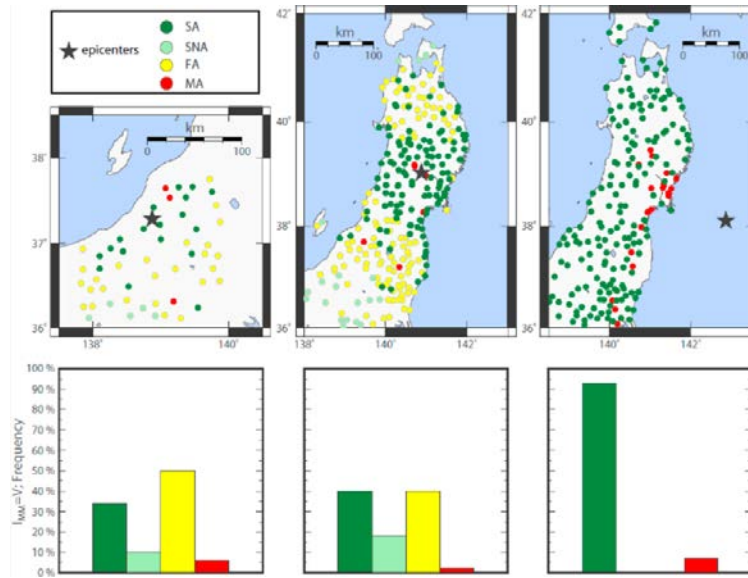


**FIGURE 2.6: SCENARIO TEST FELT LEVEL.** The Figure is the same analysis shows in figure 2.5 fixing the threshold at lower intensity level ( $I_{MM} = V$ ).

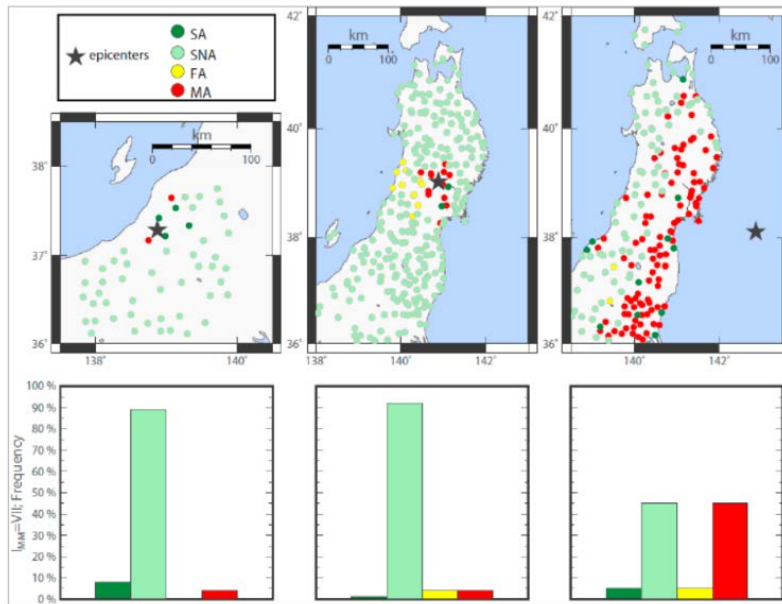


**FIGURE 2.7: SCENARIO TEST WITH LIMITED PTW.** The Figure is the same analysis shows in figure 2.5 using the theoretical P-wave time window expressed in [2.1] and set the threshold at damage intensity level ( $I_{MM} = VII$ ).

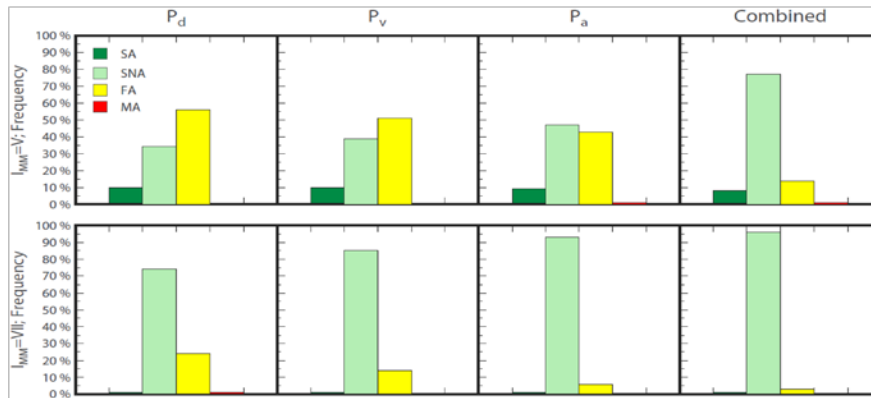


**FIGURE 2.8: CUMULATIVE STATISTICS FOR THE SINGLE PARAMETERS.** The histograms show the performance of the system, in terms of successful alarms (dark green bar), successful no alarms (light green bar), false alarms (yellow bar) and missed alerts (red bar) for the two intensity levels where the parameters are used in single mode. For the comparison with the jointly combination mode, the last column is provided.

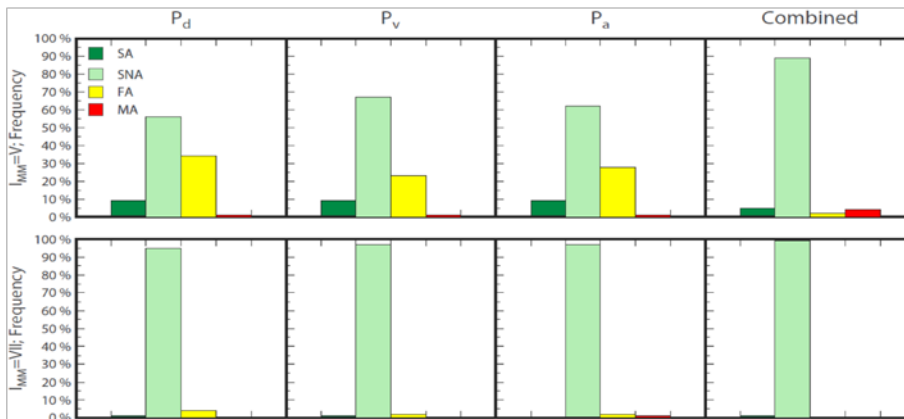


**FIGURE 2.9: CUMULATIVE STATISTICS FOR THE SINGLE PARAMETERS WITH A P-WAVE LIMITED TIME WINDOW.** The histograms show the performance of the system in the same way of figure 2.5. The difference is that the P-wave parameters are estimate on a limited P-wave time window, which is stopped at the first S-wave arrival time theoretical predicted by 2.1 relationship. For the comparison with the jointly combination mode, the last column is provided

## 2.3.2 Application to the Italian data-set

The Data-set used for this analysis consists of 229 events occurred in the Italian region during the period 2006-2016. Is the same data-set used in the section 1.3 with the addition of events recorded during the last seismic sequence of the center of italy.

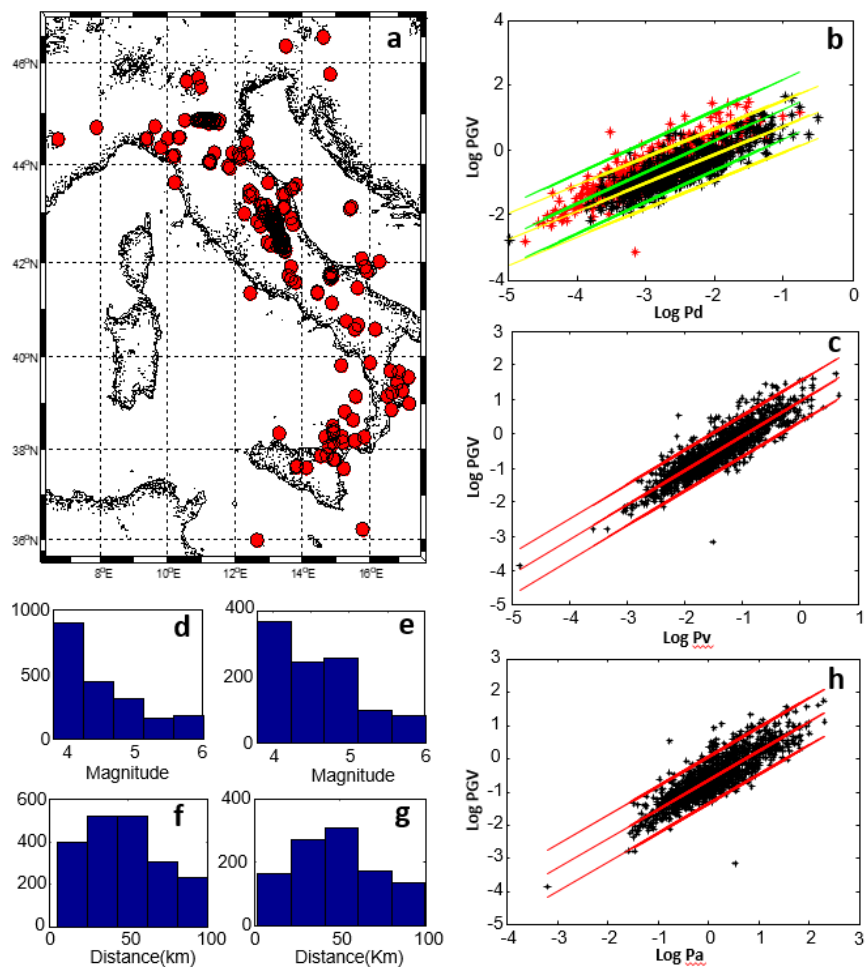


**FIGURE 2.10: DATA-SET AND CALIBRATION LAWS:** panel (a) shows the locations of events used for the analysis. (d) and (e) are magnitude histograms of data respectively used for testing and calibration phase while (f) and (g) are distance histograms of same data. In (b),(c) and (h) you can see  $P_a, P_v$  and  $P_d$  vs PGV plots (black and red stars) and the best fit lines (red, yellow and green lines) provided of  $1-\sigma$  standard deviations bars. In (b) yellow lines is the best fit of black stars data filtered with 0.075-15 Hz band pass filter while green lines is the best fit of red stars data filtered in a 1-25 Hz band.



The distribution of data in terms of magnitude and distance is provided in figure 2.10, while the epicentral location of all events used for the analysis is shown in Figure 2.10a. We processed a total of 3151 vertical components; among them, 1048 records are employed for the calibration of correlation laws and the remaining records are used for testing the system performance.

We preliminary calibrated the empirical scaling relationships to correlate the P-phase peak estimates in acceleration ( $Pa$ ), velocity ( $Pv$ ) and displacement ( $Pd$ ) to the maximum velocity amplitude recorded on the horizontal components (PGV) (Figure 2.10b,c and h). For the calibration, the initial peak amplitudes are measured on a fixed time window, depending on the theoretical arrival of the S-wave. Specifically, the  $T_s$ - $T_p$  time window is computed using equation 2.1, assuming the  $b$  factor equal to 0.082 sec/km. The empirical scaling relationships that we found are:

$$\begin{aligned} \log \text{PGV}(\text{cm/s}) &= 2.22(\pm 0.15) + 0.97(\pm 0.05) \log Pd(\text{cm}), & \text{stdv} &= 0.37, \text{band-filter: } [1;25]\text{Hz} \\ \log \text{PGV}(\text{cm/s}) &= 1.60(\pm 0.11) + 0.87(\pm 0.04) \log Pd(\text{cm}), & \text{stdv} &= 0.32, \text{band-filter: } [0.075;15]\text{Hz} \\ \log \text{PGV}(\text{cm/s}) &= 0.95(\pm 0.05) + 1.02(\pm 0.03) \log Pv(\text{cm/s}), & \text{stdv} &= 0.30, \\ \log \text{PGV}(\text{cm/s}) &= -0.89(\pm 0.03) + 0.67(\pm 0.02) \log Pa(\text{cm/s}^2), & \text{stdv} &= 0.36, \end{aligned}$$

For the testing phase, the early warning parameters are estimated in a simulated real-time data streaming environment. The preliminary signal processing for the estimation of  $Pd$ ,  $Pv$ , and  $Pa$  is the same as already explained in Chapter 1 (section 1.2). The mean value and linear trend are first removed from raw acceleration data. Then, a single and double integration operations are performed to retrieve the ground motion velocity and displacement, respectively. A high pass filter is finally applied to the displacement waveforms, to reduce the low-frequency noise contamination deriving from the double integration operation. In order to establish the proper cut-off frequency for the filter, the quality of the signal is evaluated by estimating the Signal to Noise Ratio (SNR) and the  $Pv/Pd$  ratio. In the previous

chapter more details and motivations of this filter processing is provided. After the preliminary data processing and quality check analysis, the P-wave parameters are estimated on the vertical component of the signals, using progressively expanding time windows, without any further constraint to the expected S-wave arrival time. A statistical analysis shows that about 30% of the S-wave amplitude is present on the vertical component (see Figure 2.12).

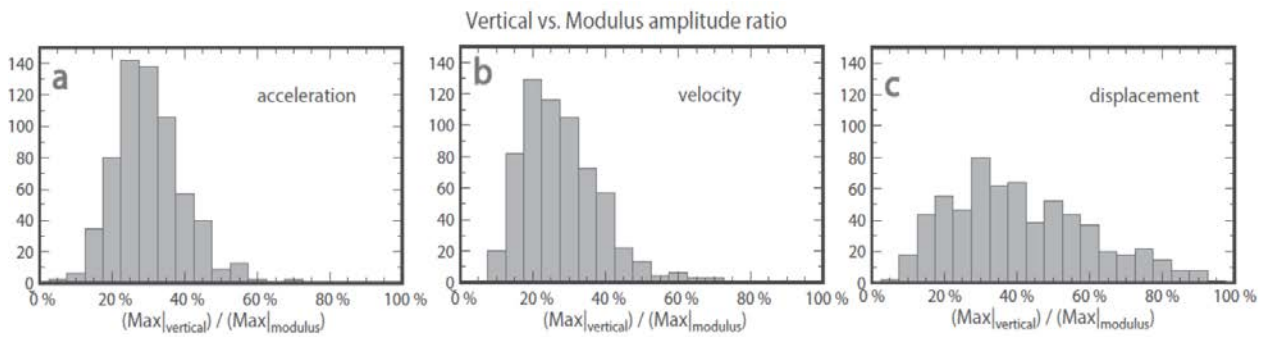


**FIGURE 2.12: VERTICAL VS. HORIZONTAL AMPLITUDE RATIO.** Histogram of the S-wave amplitude ratio among the vertical component and the modulus of acceleration (a), velocity (b) and displacement (c). The amplitude is computed within a 5 second time window around the expected S-wave arrival time.

To avoid the inclusion of later phase arrivals after the P-wave, we performed a signal polarization analysis of the 3-component waveforms, following the formulation proposed by Rosenberger [2010].

Specifically, as soon as the P-wave phase is automatically detected (using Filter-Picker algorithm [Lomax, A., C. Satriano and M. Vassallo, 2012]), the algorithm starts to continuously estimate the polarization of the signal in real-time and looks for its variation from a reference polarization direction value. The reference direction of the polarization vector is estimated as the direction closer to the vertical during the first 0.5 second of the signal after the P-wave arrival time ( $\widehat{u}_p$ ) and is used to compare the real-time estimate of the signal polarization ( $\widehat{u}_t$ ). In particular, the dot product ( $\widehat{u}_p \cdot \widehat{u}_t$ ) is about 1 when the polarization is consistent with that observed for the P phase and tends to 0 when the

polarization is on the orthogonal direction (as for the S-wave polarization). The dot product is used as a characteristic function (Figure 2.13b) to modulate the amplitude of signal and decrement the peak of the signal associated to the S-wave phase arrival (Figure 2.13).

After modulating the signal amplitude, we estimated the early warning parameters on a P-wave dominant signal, where the influence of the S-wave arrival is expected to be significantly reduced.

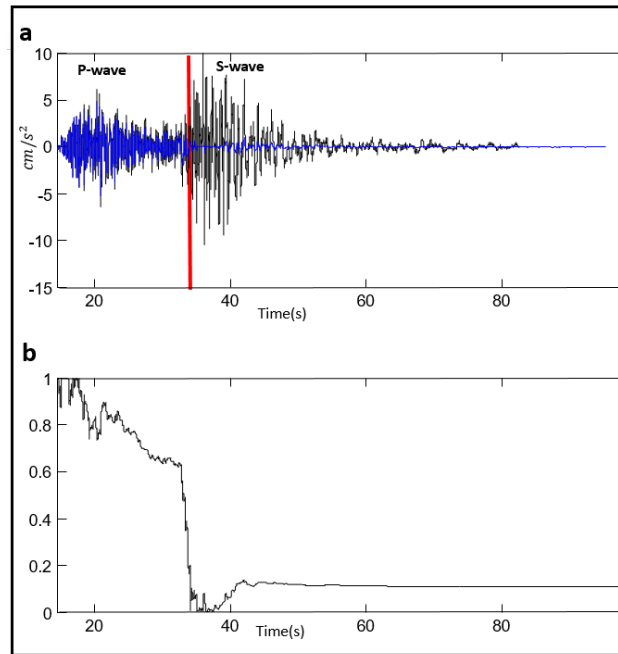


**FIGURE 2.13: POLARIZATION FILTER.** (a) Show an example of vertical component processed with SVD polarization algorithm, the black line plot is the original z-component while the blue line is the **P-wave dominant** waveform obtained using the characteristic function shows in panel (b).

The EW system performance is evaluated using 2103 vertical component records, with magnitude ranging between 4 and 6.5 and hypocentral distances between 0 and 100 km (see the histograms in Figure 2.11d,f).

PERCEIVED SHAKING	Not felt	Weak	Light	Moderate	Strong	Very strong	Severe	Violent	Extreme
POTENTIAL DAMAGE	none	none	none	Very light	Light	Moderate	Moderate/Heavy	Heavy	Very Heavy
PEAK ACC.(%g)	<.21	.21-0.52	0.52-1.3	1.3-3.1	3.1-7.5	7.5-18	18-45	45-109	>109
PEAK VEL.(cm/s)	<0.08	0.08-0.2	0.2-0.6	0.6-1.5	1.5-3.4	3.4-10	10-26	26-74	>74
INSTRUMENTAL INTENSITY	I	II-III	IV	V	VI	VII	VIII	IX	X*

FIGURE 3.11: INTENSITY CONVERSION TABLE. L. Faenza and A. Michellini, 2010.

The performance of the system is evaluated by counting the percentage of successful alarms (SA and SNA), FA and MA using two critical level of local intensity correspond at PGV equal to 0.6 cm/s (IMM=V) and PGV equal to 3.4 cm/s (IMM=VII) (according to Faenza and Michellini 2010 conversion table, Figure 2.11). In order to maximizing the number of successful prediction of the system, the **Wt** thresholds are fixed at 0.5 and 0.6 for felt and damage intensity level, respectively.

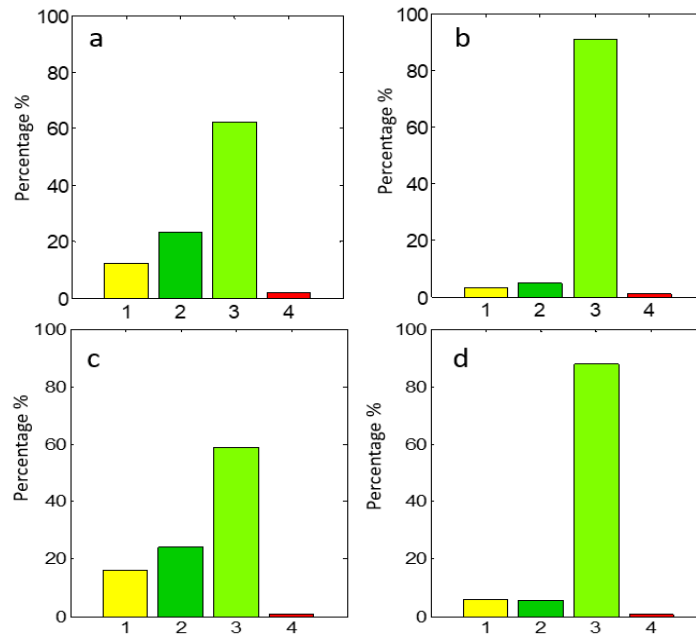
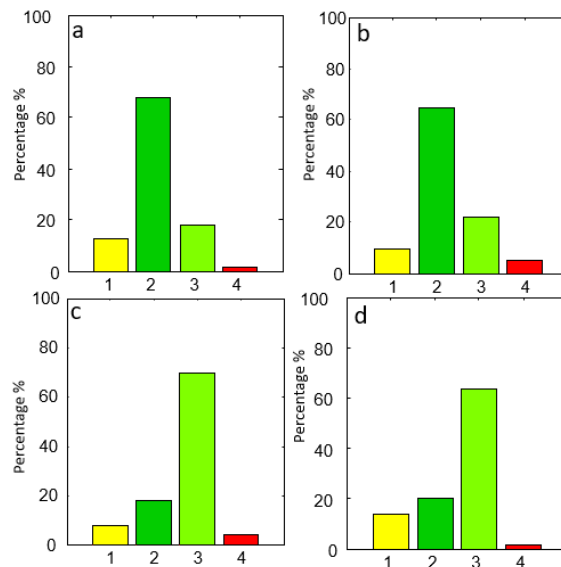


FIGURE 2.14: CUMULATIVE STATISTICS. The figure shows the cumulative statistics for all data of testing database. (b) and (a) show the statistics, using a threshold level on felt intensity level (IMM=V), respectively for data processed with polarization filter algorithm or not. (d) and (c) are the same analysis using a threshold level on damage intensity level (IMM=VII).

The histograms of figure 2.14 show the percentage of outcomes for all data, both using the polarization analysis (left panel) and using the vertical component of the recorded waveforms without any

amplitude modulation (right panel). The use of the polarization analysis improves the reliability of the prediction, with a reduction of false alerts of about 9% (as it is shown in Figure 2.14).

Finally, we evaluated the performance of the methodology for the largest events, with magnitude greater or equal than 5 Mw (Figure 2.15), which undoubtedly represent the most dangerous and most relevant cases to be considered.



**FIGURE 2.15: CUMULATIVE STATISTICS.** The figure shows the same analysis of figure 2.14 using only data with moment magnitude greater than 5.

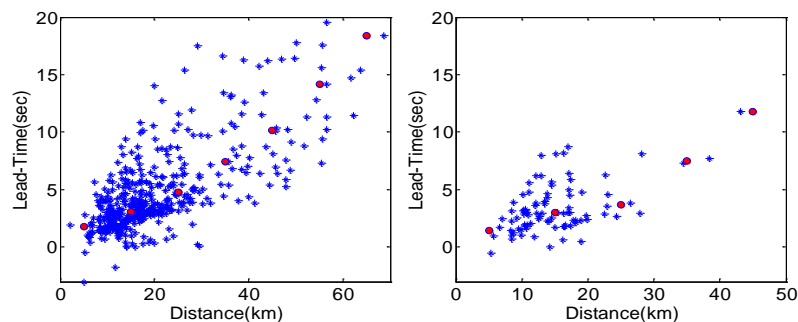


**FIGURE 2.16: LEAD-TIME STATISTICS.** The figure shows the Lead-time vs distance plots for alerts provided using all testing data-set. the Lead-times for damage threshold level are provided on the right, while on the left threshold is fixed on felt level. The red circles are the median values estimate using a bin of 10 kilometers. Negative Lead-times are considered missing alerts in cumulative statistics.

The percentage of successful predictions (SNA+SA) is larger than 80%, while the cumulative percentage of missed and false predictions (MA+FA) is about 20%. The available lead-times as a function of distance for the SA case, are shown in figure 2.16. Between 10 and 30 km from the source, most of the lead times vary between 1-2 s and 5-6 s, with an average value of about 3s.

After evaluating the overall statistics, we applied the methodology to a limited number of scenario cases. The analyzed events are two of the largest earthquakes occurred during the recent 2016-2017, central-Italy earthquake sequence: the Mw 5.5, 2016 10, 26 Macerata earthquake and the Mw 6.5, 2016 10, 30, Norcia earthquake.

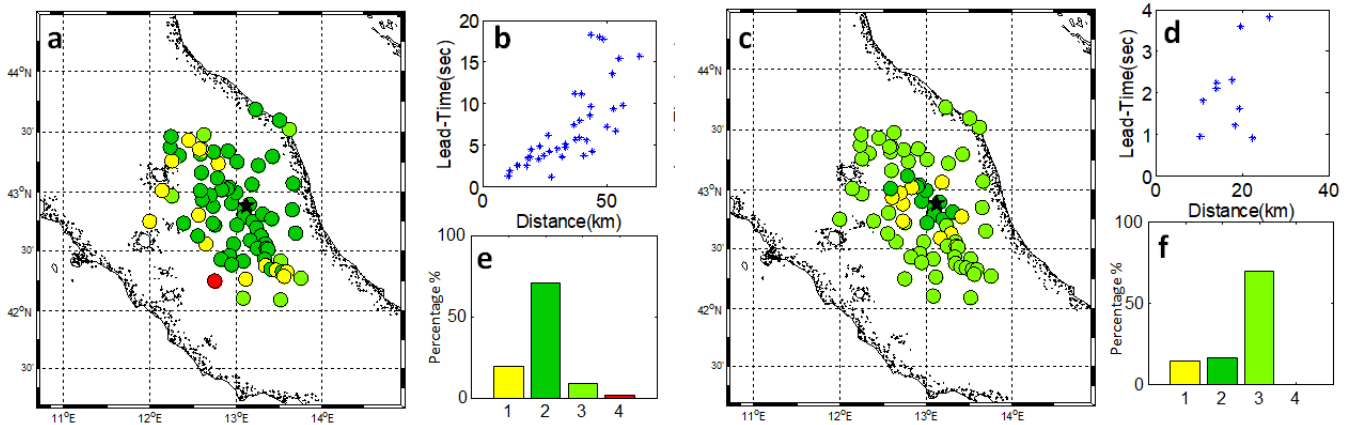


**FIGURE 2.17: SCENARIO TEST OF MACERATA EARTHQUAKE.** The figure shows the performance of system in scenario of Amatrice earthquake. (a), (b) and (c) panel are respectively the map of stations (circles colored according to predictive results) and epicenter (back star) used for the analysis, the plot of Lead-time vs distance and cumulative statistics for threshold fixed on the felt level (PGVth=0.6cm). (c), (d) and (f) are the same analysis for threshold fixed on the damage (PGVth=3.4 cm).

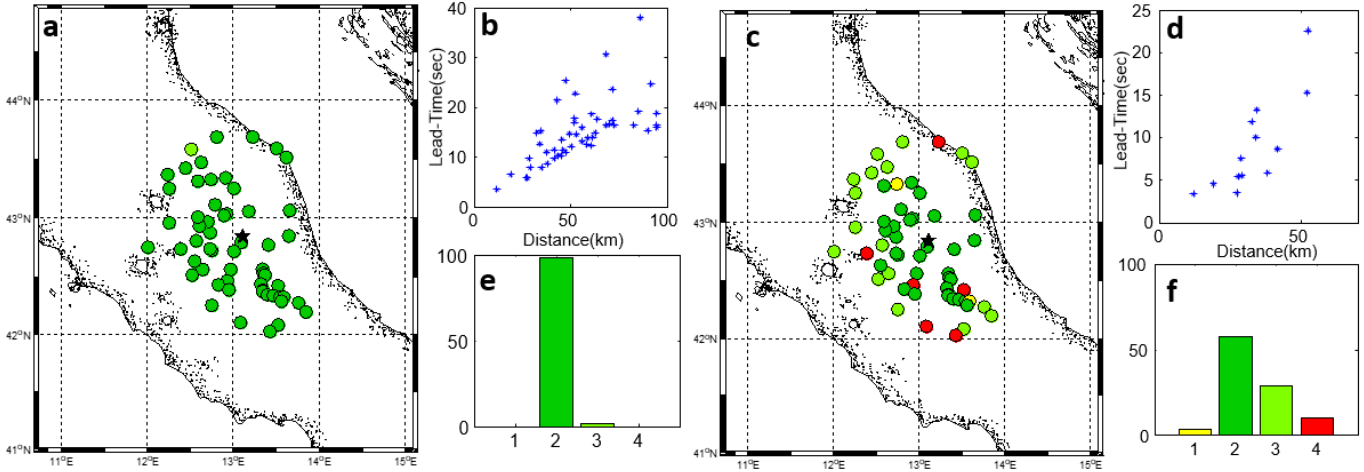


**FIGURE 2.18: SCENARIO TEST OF NORCIA EARTHQUAKE.** The figure shows, in the same way of figure 2.17, the performance of system in scenario of Norcia earthquake.

We focused our attention on data recorded in the source area, within 100 km from the epicenter. For both events, the system provided a relatively high rate of successful alerts. In particular, for the Macerata earthquake scenario, we found about 20% of false and about 5% of missed alerts for felt threshold (Figure 2.17e) and about 15% of false alters for damage threshold (Figure 2.17f). The Norcia case study showed no cases of false alarms and about 15 % of missed alerts in case the threshold is set on damage level (Figure 2.18f).

## 2.4 Discussion

The Early Warning methodology that we proposed is based on the real-time, continuous measurement of three peak amplitude parameters ( $P_d$ ,  $P_v$  and  $P_a$ ) which are empirically combined for the prediction of the expected shaking at the same site. Acceleration, velocity and displacement provide a complementary image of the spectral content of the source, whose highest frequencies are mostly associated to finer details of the rupture process and wave propagation, while the low-frequency content is sensitive to the seismic moment.

The S-waves are generally identified along the horizontal components of a seismogram through the variation in amplitude and frequency of the signal with respect to the preceding P-waves (Diehl et al., 2009). However, in those regions where extensional or compressional tectonics is dominant, the S-wave amplitude along the vertical component may be not negligible. For example, in the case of Japan the S-wave amplitude along the vertical component at the S-arrival time represents about 30% of the whole seismogram amplitude (i.e., the modulus of ground motion recordings), as it can be inferred from the histogram of Figure 2.12. This confirms that a large portion of the S-wave amplitude may contaminate the vertical component of ground motion.

Efficient algorithms, based on the use of a characteristic function, for the S-wave arrival time identification have been proposed and refined techniques combining polarization analysis and lateral waveform coherence of earthquake recordings have been also recently proposed (Amoroso et al., 2012, Rosenberger, 2010 etc...). In final part of this analysis, an algorithm based on the polarization analysis of the 3-component recorded seismograms is proposed and applied in order to reduce the S-wave amplitude contamination on the vertical component of the ground motion and to provide a “P-wave dominant” signal to be used for the measurement of the initial P-wave peak amplitude parameters.



The performance of the system significantly changes when limited (to the S-wave first arrival) or unlimited time windows are considered. Figure 2.7 shows the performance for the scenario cases, when limited time windows are used for the parameter measurement. As intuitively expected, when the P-wave time window is progressively expanded and no time limit is imposed, the incidence of false alarms increases, with respect to the case of limited time windows. The increase, however, is balanced by a substantial reduction of missed alarms, which are, indeed, the most critical issue for an EWS. This is especially true for the case of the 2011, Mw 9.0, Tohoku-Oki earthquake, for which the percentage of missed alerts decreases from about 50% to only 2%, when unlimited time windows are considered.

One main advantage of the proposed methodology is that, in principle, depending on the desired application, false or missed alarms can be prioritized at the user's discretion. Following the calibration curves of Figure 2.1d, for example, the percentage of false alarms can be reduced by choosing a high  $W_t$  value, with a consequent little increase of missed alert. On the contrary, for those applications in which false alarms are more tolerable, while missed alarms should be avoided, lower  $W_t$  values are to be preferred.

A similar calibration can be done in any standard on-site approach, by changing the threshold value chosen for the warning declaration. However, when limited time windows are used, the missed alerts are related not only to the threshold value for the warning declaration, but are also due to an intrinsic limitation of the methodologies, which are not able to follow the evolution of the source process. For this reason, the incidence of missed alerts in standard approaches cannot be easily reduced without increasing false alarms too much, and this is especially true for the case of large events.

In terms of timing performances, the proposed methodology may require shorter or longer signal portions for the warning declaration, as compared to the standard approaches. In a standard on-site EWS, 3 seconds of P-wave signal are used for the parameter estimation and thus the alert time does not

depend neither on the source-to-receiver distance nor on the earthquake magnitude. The gray dashed line in Figure 2.4c shows the alert time for a common on-site EW system. In our approach, instead, both distance and magnitude play here a key role. We found that alert times are around 1-2 seconds for small-to-moderate events recorded at small epicentral distances (i.e., for magnitude between 4 and 5 within 100 km), while longer PTWs are required in case of large events recorded at large distances (20-to-30 seconds for magnitude 9 events, recorded at 300 km). This result is consistent with the recent observations of Colombelli et al., (2014), who measured the logarithm of  $Pd$  over progressively expanding PTWs and found that it starts with small values and then progressively increases with time, until a plateau value is reached. The greater the magnitude, the longer the time is needed for  $Pd$  to reach its final value. From a practical point of view, in the proposed approach, the warning can be declared within a very short time window, for small-to-moderate events, while longer P-wave time signals are needed to properly predict the expected shaking for large events.

As for the lead-times, the plots show a clear dependency with both distance and magnitude, as confirmed by the best fit regression line (solid gray line) and by the colors scale of figure 2.4 c.f. . As for the distance dependency, this result is not surprising, since the lead-time is essentially due to the S-P wave travel time difference. Our observed lead-times are generally smaller than the theoretical values, with about 10 seconds of lead-time at a distance of 100 km and about 20 seconds at 200 km. For comparison, the theoretical lead-time as a function of distance is shown with a dashed gray line. The dependency of lead-times on magnitude can be explained in terms of source process and of propagation effects. For large events, indeed, the source process has a longer duration and a late peak in the moment rate function is expected. In addition, magnitude generally increases with distance in the Japanese earthquake database, since the largest events are mostly occurring offshore at the slab zone. As a consequence, the strongest ground shaking can be associated either to later slip episodes and to the arrival of later phases.

The application of the proposed methodology to the M 9.0 Tohoku-Oki event provided a relatively high percentage of false alarms (about 49%). We point out, however, that all of these false alarms are associated with a ground shaking amplitude and related intensity smaller than the predicted damage level but higher than the level of perceived shaking by population. This reduces the negative impact of false alarms and cry-wolf syndrome, due to the effective experience of earthquake shaking as a consequence of the alert.

For the Tohoku-Oki event, the kinematic inversions have shown a complex frequency dependent rupture history, with asperities radiating energy with different frequency content at different locations (Meng et al., 2011; Maerklin et al., 2012). The evolutionary estimate of  $Pd$  showed that the initial P-wave amplitude is largely underestimated with short P-wave time windows, while stable and consistent magnitude values are obtained for PTW exceeding 25-30 s. Here, indeed, we found a similar result, with warning times for the magnitude 9 event of about 20-25 s within 200 km and with longer PTWs of more than 30 seconds needed at larger distances, thus confirming that appropriate time windows are required to capture longer portions of the rupture process and lower frequencies radiated from the source. Standard EEW methodologies, which are based on the use of limited P-wave signal portions, would have not been able to capture the energy from the whole source process, with a consequent dramatic underestimation of the expected shaking (Hoshiaba et al., 2011; Colombelli et al., 2012b).

In our methodology, the alert for the higher intensity level would have been issued at coastal stations approximately 36 seconds after the first P-wave detection, thus still providing around 23 seconds of warning, prior to the arrival time of the strongest shaking. In the region of Tokyo, instead, the alert would have been issued about 60 seconds after the P-wave detection, with about 38 seconds of warning.

We also evaluated the performance of the proposed methodology using a data-set of Italian earthquakes and applying the polarization analysis described in Section 2.3.2. This further application confirms the reliability of the methodology that has been strengthened with a polarization filter of vertical component that reduces number of false alert (Figure 2.15 2.14).

A practical strategy for the proposed approach could be to declare the first warning as soon as the lower intensity threshold is overcome and then to confirm (or possibly cancel) the previous alert, if the higher intensity threshold is also reached.

# **Chapter 3: Rapid estimation of the earthquake potential damage zone**

## **3.1 Introduction**

In the previous chapters, we introduced two different approaches for an on-site EEWS and we discussed in details the methodologies and the results of their application to Japan and Italian earthquakes. In the present chapter, we present a methodology, called QUAKE-UP, aimed at integrating the network and on-site approach to have a more complete and reliable real-time characterization of the earthquake source and of the intensity impact of the seismic wave in the area affected by the event.

The proposed strategy is based on the idea to combine the on-site strategy, discussed in Chapter 2, in a dense seismic network with the aim to use the on-site measurement to give a prediction of shaking expected around the epicentral area. At the same time, using the seismic observations at more stations, the system is able to locate and estimate the magnitude of the source with an evolutionary and probabilistic approach.

A complete characterization of the event is given and the impact of the earthquake is predicted through the estimation of an early shake-map based on the interpolation algorithm of P-wave parameters measured at nodes of the network and the local intensity predicted by the attenuation laws using the location and magnitude of the earthquake.

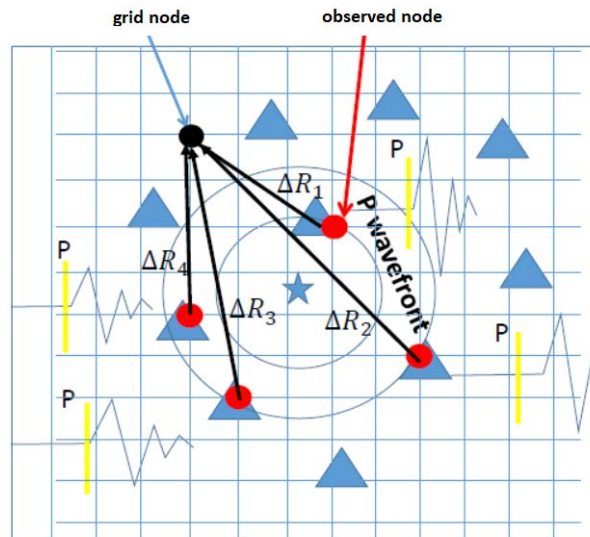


**FIGURE 3.1. QUAKE-UP CONCEPT:** The figure shows the concept idea of Quake-up. The observed nodes (network stations drawn as blue triangles) are used to predict the observations on the nodes of a regular grid. The data available (red circles) and the values predicted by the P-wave attenuation laws using location and Magnitude are weigh in function of the distance from the node (black circles) in order to predict the P-wave amplitude in this point.

This is done by correlating the measured P-wave amplitude with the Peak Ground Velocity and Instrumental Intensity and by mapping the measured and predicted P-peak displacement at a dense spatial grid, which includes the nodes of the accelerometer array deployed in the earthquake source area. The interpolation algorithm is inspired by the concept of USGS shake-map algorithm [Worden, C.B et al., 2010].

In this framework, a software platform was developed, that includes the most advanced techniques for a refined estimation of the main source parameters (earthquake location and magnitude) and for an accurate prediction of the expected ground shaking level. We apply this methodology on the main shock of the recent seismic sequence occurred in the central Italy and on two Japan earthquakes with magnitude larger than 7.

## 3.2 Methodology

This first step of this methodology is the real-time detection and location of event using the RT-LOC algorithm [Satriano *et al.* 2008]. The real-time picker used for the P-wave arrival time detection is filter-picker 5 [Lomax *et al.*, 2011].

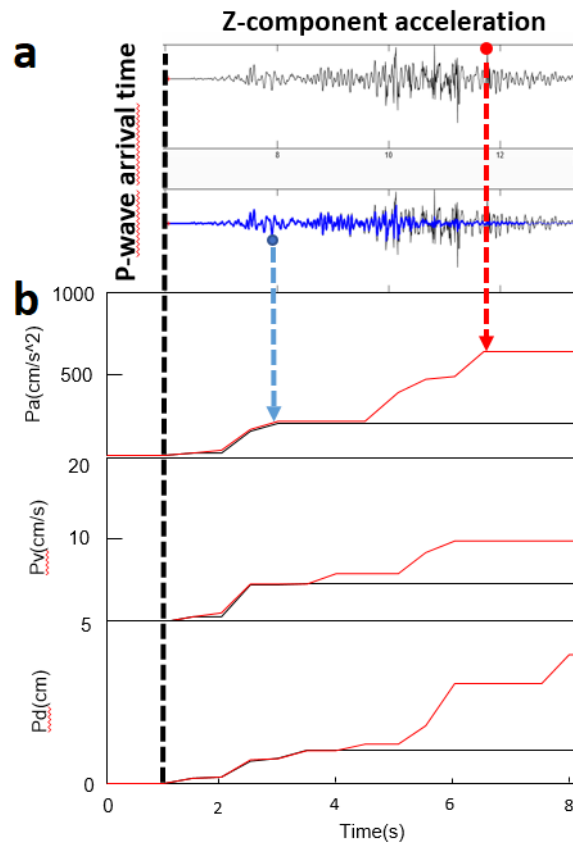


**FIGURE 3.2. P-wave parameters:** (a) shows an example of P-wave processing. The data used is the acceleration Z-component recorded during the Norcia earthquake at Arquata del Tronto site. The black line represents the original waveform while blue line is the trace processed by SVD algorithm. Red and blue circles are the maximum of  $P_a$  respectively on the original and P-dominant trace. (b) shows the realtime measurement of  $P_a$ ,  $P_v$ , and  $P_d$  exemplifying the time window from the P arrival time (dashed line) on the original trace (red line) and on P-dominant trace (black line).

The system processes the accelerometric, vertical components of the ground motion, provided by the high quality sensors in real-time. The mean value and linear trend are first removed from raw acceleration waveforms. A quality check of the input data, based on the signal-to-noise ratio and on the  $Pd/Pv$  ratio is used to estimate the proper filter (the procedure is the same as performed by SAVE system and described in Chapter 1). The system then uses the acceleration waveform to estimate the  $Pa$  (P-wave pick acceleration). Subsequently, accelerometer data are integrated to obtain the velocity and the linear trend is removed again, prior to estimate the  $Pv$  (P-wave pick velocity). After a second integration, the displacement waveform is obtained. In order to remove the low frequency amplification effect caused by the double integration processing, the trace is filtered with the high pass filter selected during the quality control phase. In this way, the data-processing provides a robust estimation of the P-wave pick amplitudes, in acceleration, velocity and displacement, which are then jointly used to predict the maximum PGV expected at site. The local intensity in terms of PGV at the observation site of the network is estimated using the following relationships:

$$\text{Log}(PGV)=a*\text{Log}(Pa)-b; \quad [3.1]$$

$$\text{Log}(PGV)=a'*\text{Log}(Pv)+b'; \quad [3.2]$$

$$\text{Log}(PGV)=a''*\text{Log}(Pd)+b''; \quad [3.3]$$

$$\omega_i = \frac{1}{\sigma_i^2}; \quad PGV = \frac{\sum_{i=1}^3 \omega_i PGV_i}{\sum_{i=1}^3 \omega_i}, \quad i = [a \ v \ d] \quad [3.4]$$

In [3.4]  $\sigma_i$  are the standard deviations of [3.1], [3.2] and [3.3] that are retrieved using a specific calibration data-set. The amplitude P-wave peaks are measured on an expanded time windows. The use of the vertical component reduces the S-wave influence as explained in Chapter 1. Moreover, the traces



are processed using a real-time polarization filter based on the SVD decomposition, described in the previous chapter, in order to reduce the S-wave contamination during the peak measurements.

The expected value is estimated as a weighted average of the PGV obtained from [3.1], [3.2] and [3.3].

The weights are the reverse of square uncertainties as written in [3.4].

The values of PGV predicted in a generic point of the numeric grid are estimated using an interpolation algorithm that combines: 1) the expected PGV from the on-site measurement (PGV on-site) and 2) the expected PGV provided by the network-based algorithm given the location and magnitude estimates (PGV\_GMPE). The algorithm combines this two pieces of information using the following relationships:

$$\sigma_{x,y,on-site} = \sigma_{GMPE} \cdot (1 - \exp(-\sqrt{0.6 \cdot r_{\Delta}})) \quad r_{\Delta} \leq Rroi \quad [3.5]$$

$$\sigma_{x,y,on-site} = (\sigma_{x,y,on-site}|_{r_{\Delta}=Rroi}) \cdot \frac{r_{max}-Rroi}{r_{max}-r_{\Delta}} \quad r_{max} \geq r_{\Delta} > Rroi \quad [3.6]$$

$$\sigma_{x,y,on-site} = \infty \quad r_{\Delta} \geq r_{max} \quad [3.7]$$

$$\overline{PGV} = \frac{\sum_{i=1}^N \left[ \frac{1^2}{\sigma_{x,y,on-site,i}} * PGV_{x,y,on-site,i} \right] + \frac{1^2}{\sigma_{theo}} * PGV_{x,y,theo}}{\sum_{i=1}^N \frac{1^2}{\sigma_{x,y,on-site,i}} + \frac{1^2}{\sigma_{theo}}} \quad [3.7]$$

where **Rroi** defines the area around the observed points where the observed data influence the PGV interpolation more than the PGV estimate through the attenuation law and **Rmax** defines the limit of the area where the observed data influence the interpolation. The setting of these parameters depends on the density of the network.

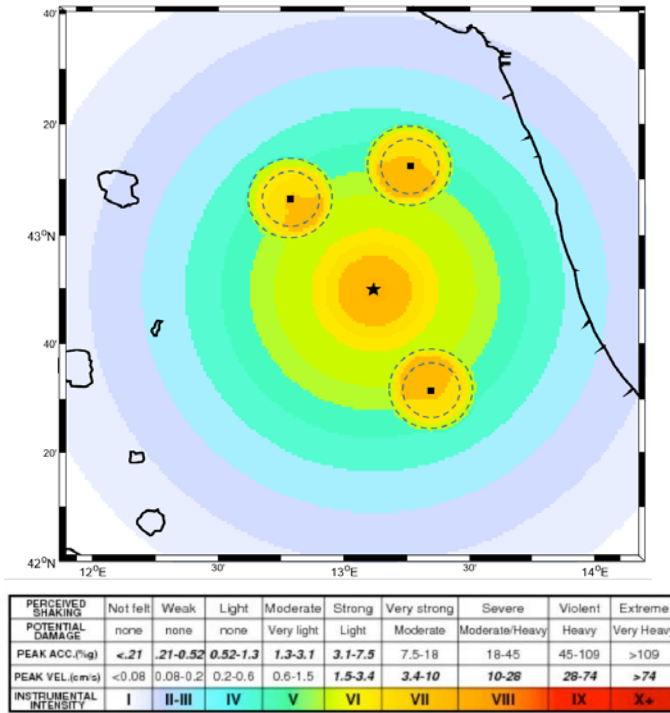


**FIGURE 3.3. MAPPING ALGORITHM EXAMPLE:** The figure shows an example of the MAP interpolation algorithm. The black star is the epicenter of event while black squares are the three observation points with high values of P-wave amplitudes ( $P_a, P_v$  and  $P_d$ ). The dashed circles are the areas of radius  $R_{roi}$  (10km) and  $R_{max}$  (15km), where the observation points influence the estimation of map. Outside from these areas, the map is calculated using [3.8] – [3.10]. The PGV is predicted using [3.1] – [3.4] and finally converted in the Intensity using the table shown in figure.

This approach is borrowed from the generic shake-map interpolation algorithm [Worden, C.B et al., 2010]. Also the  $\sigma_{x,y,on-site}$  and  $\sigma_{theo}$  are the uncertainties associated respectively to the PGV predicted from the on-site measurement of the P-wave peaks while the second one is the standard deviation of the following attenuation laws:

$$\log(Pa_{x,y,theo}) = c + d * M - e * \log(R); \quad [3.8]$$

$$\log(Pv_{x,y,theo}) = -c' + d' * M - e' * \log(R); \quad [3.9]$$

$$\log(Pd_{x,y,theo}) = -c'' + d'' * M - e'' * \log(R); \quad [3.10]$$

The  $PGV_{x,y,theo}$  is retrieved using the  $Pa_{x,y,theo}$ ,  $Pv_{x,y,theo}$  and  $Pd_{x,y,theo}$  in the [3.1], [3.2], [3.3] and the final PGV is obtained using [3.4].

In order to give the more reliable values of magnitude, the final value is the median of the below estimations:

$$M_{wt} = f * \log(\tau_{c,x,y}) + g; \quad [3.11]$$

$$M_{wpd} = h * \log(Pd_{x,y}) + i * \log(R) + l; \quad [3.12]$$

$$M_{wppv} = h' * \log(Pv_{x,y}) + i' * \log(R) + l'; \quad [3.13]$$

$$M_{wpa} = h'' * \log(Pa_{x,y}) + i'' * \log(R) + l''; \quad [3.14]$$

The  $Pv_{x,y}$ ,  $Pa_{x,y}$ ,  $Pd_{x,y}$  and  $\tau_{c,x,y}$  are respectively the P-wave peaks, the hypocentral distance and the signal predominant period [Kanamori et al. 2005] measured in real-time at each stations of the network. In this way, each triggered stations provide four estimations of Moment Magnitude and the real-time out-put of the system is the median value weighted with the respectively P-wave time window duration as described below:

$$\omega_i = \frac{1}{\sigma_i^2}; M_{wp} = \frac{\sum_{i=1}^3 \omega_i M_{wpi}}{\sum_{i=1}^3 \omega_i}; \quad i = [a \ v \ d]; \quad [3.16]$$

$$\overline{M}_W = \frac{\sum_{n=1}^{N(t)} (M_{wpn} + M_{wt_n}) * Td_n}{2 * \sum_{n=1}^{N(t)} Td_n}; \quad [3.17]$$

Where the  $\sigma_i$  are the standard deviations of [3.12], [3.13] and [3.14]. In the [3.17],  $\mathbf{n}$  is referred at the n-th triggered station.

In order to have a rapid and reliable convergence to the final magnitude of the event, only the recordings within 100km from the epicenter are used, or alternatively the first 30 triggered stations.

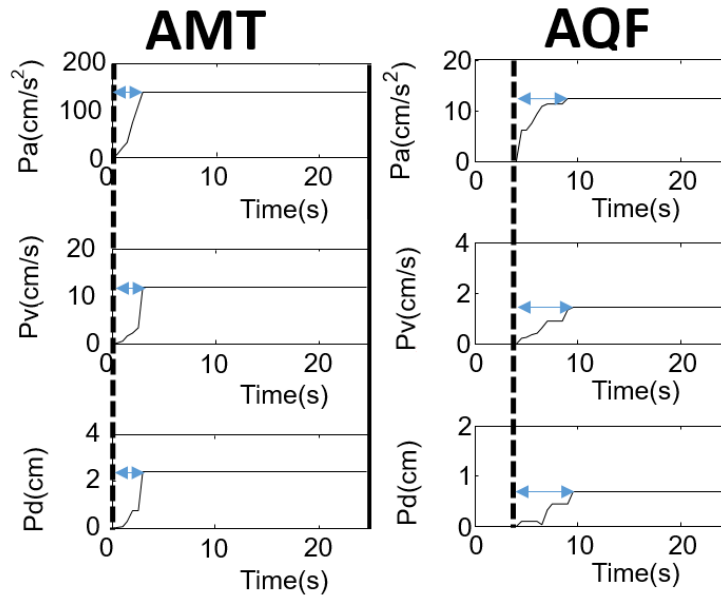


**FIGURE 3.4. DISTANCE DEPENDENCE OF RISE-TIME:** On the left, there are the P-wave parameters ( $P_a, P_v, P_d$ ) measured on an expanded time window from P-wave arrival time (Dashed line). The slope curves are referred at record of Norcia earthquake (Mw 6.5) at Amatrice site, about 25 km of distance from the source. On the right, there are the same plots for L’Aquila site, about 50 km of distance. Blue indicators show the rise-time of slope curves, that in Amatrice case is about 2-3 seconds while L’Aquila case is about 4-5 seconds.

The early shake-map is the interpolation of  $PGV_{x,y}$  converted into instrumental intensity. The final output of the algorithm is the map of the predicted shaking intensity produced by the ongoing earthquake. It is updated in real-time when the new data-measurement are available or when the estimation of location and magnitude change. The data provided from the stations far away from the epicentral area are reliable after few seconds of the P time window (PTW) (see comparison between AMT and AQF

stations in Figure 3.4). For the station far away from the source, the predicted shaking is underestimated respect to the final values because the data ( $P_v$ ,  $P_a$  and  $P_d$ ) are related to a partial P-wave packet irradiated by the source.

As show in Figure 3.4 at station AQF, the convergence at final values of P-wave amplitude parameters requires several seconds, for this reason, to avoid the local intensity underestimation, the measurements done on a short P-wave time window, where the available P-wave time window is shorter than the theoretical  $T_s$ - $T_p$  time, computed using localization and a velocity model for the P and S waves ( $T_s$  and  $T_p$  are the theoretical arrival time respectively of S and P phases), are not included in the interpolation algorithm.

### 3.3 Application and results

In order to test this Early-warning system concept, we perform three different scenario tests with the aim to check the reliability of the strong earthquakes characterization. The events selected are:

- The Norcia earthquake occurred on october 30, 2016. The moment magnitude of this event is estimated by INGV (Istituto Nazionale Geofisica Vulcanologia) as 6.5 Mw and the strong shaking is recorder in most part of the central Italy.
- The 2008 Iwate earthquake with a moment Magnitude of 6.9.
- The last scenario test is the mega earthquake occurred off the Pacific coast of Tōhoku region in 2011. It was the most powerful earthquake ever recorded in Japan and the fault region is about 500 km length. The earthquake and tsunami also caused extensive and severe structural damage in north-eastern Japan, including heavy damage to roads and railways as well as fires in many areas, and a dam collapse.

The test is performed using the accelerometric data recorded at the local network and using the simulate the real-time processing like SAVE analysis setting the virtual transmitted package duration at 0.5 second. The on-site parameters are estimate in the same way of the SAVE, the difference is that in this analysis are using all three parameters in order to have a more reliable prediction of the maximum PGV occurred. The information predicted is used at the time that is available with the aim to simulate e time evolution of the Location, Magnitude and Intensity map prediction.

In this first preliminary analysis we have observed the evolution in time of the map prediction and the source parameters estimation. The speed convergence at the system final estimation depend on the network density around the epicentral area.

### 3.3.1 Application to 2016 Norcia 6.5 Mw earthquake

This earthquake is the main shock of the last Italian seismic sequence, started in august 2016, which is still affecting the center Italy areas. In order to perform this scenario test, we calibrated equations [3.1-3.3] and [3.8-3.10] using a a-doc Italian data-set composed by records of earthquakes in the magnitude range between 4 and 6 and epicentral distance between 10 and 200 km (The database consists of the accelerometric traces provided by the national Italian network, the same used for the calibration of the SAVE system and explained in chapter 1). The calibration is performed by processing the data in the same way of the real-time processing. The relationship retrieved are the following:

$$\text{Log}(PGV) = 0.75 \pm (0.02) * \text{Log}(Pa) - 0.74 \pm (0.01); \quad \sigma: 0.39 \quad R^2: 0.73 \quad [3.18]$$

$$\text{Log}(PGV) = 0.88 \pm (0.02) * \text{Log}(Pv) + 0.54 \pm (0.03); \quad \sigma: 0.35 \quad R^2: 0.79 \quad [3.19]$$

$$\text{Log}(PGV) = 0.73 \pm (0.02) * \text{Log}(Pd) + 1.21 \pm (0.05); \quad \sigma: 0.41 \quad R^2: 0.70 \quad [3.20]$$

$$M_{wt} = 2.90 \pm (0.43) * \log(\tau_{c,x,y}) + 4.78 \pm (0.10); \quad \sigma: 0.46 \quad R^2: 0.39 \quad [3.21]$$

$$Pa_{x,y,theo} = +0.72 \pm (0.35) + 0.64 \pm (0.06) * \mathbf{M} - 2.15 \pm (0.12) * \log(\mathbf{R}); \quad [3.22]$$

$$Pv_{x,y,theo} = -2.10 \pm (0.32) \pm (0.35) + 0.80 \pm (0.05) * \mathbf{M} - 1.78 \pm (0.11) * \log(\mathbf{R}); \quad [3.23]$$

$$Pd_{x,y,theo} = -4.15 \pm (0.41) + 0.97 \pm (0.07) * \mathbf{M} - 1.77 \pm (0.14) * \log(\mathbf{R}); \quad [3.24]$$

$$M_{wpa} = 1.41 \pm (0.13) * \log(Pa_{x,y}) + 3.06 \pm (0.32) * \log(\mathbf{R}) - 0.62 \pm (0.58); \quad [3.25]$$

$$M_{wpv} = 2.11 \pm (0.19) * \log(Pv_{x,y}) + 1.18 \pm (0.08) * \log(\mathbf{R}) + 2.71 \pm (0.28); \quad [3.26]$$

$$M_{wpa} = 0.96 \pm (0.07) * \log(Pd_{x,y}) + 1.72 \pm (0.18) * \log(\mathbf{R}) + 4.25 \pm (0.27) \quad [3.27]$$

in the above equations, PGV are the absolute maximum measured on the horizontal components in velocity. The  $Pa, Pv$  and  $Pd$  are estimated on the P-dominant vertical-components, obtained using the SVD polarization filter,  $\mathbf{M}$  is the moment Magnitude of the event and  $\mathbf{R}$  is the hypocentral distances from the event.

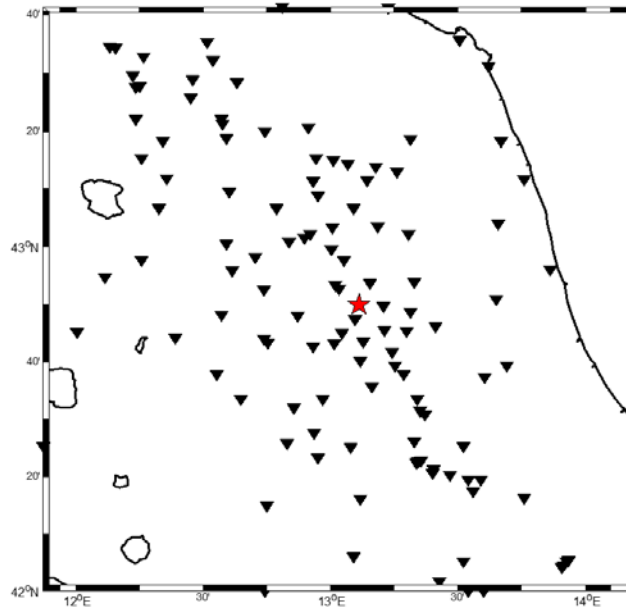


**FIGURE 3.5. NORCIA EARTHQUAKE SCENARIO:** The figure shows the data used to perform the scenario test of Norcia earthquake (6.5 Mw). The Red star is epicenter while the black triangles are stations used for the analysis.

In this first scenario case, the data are provided by the Italian accelerometer network managed by the civil protection [Gorini *et al.* 2010]. The network is built from 235 high quality accelerometer stations in a range of distance between 10 and 300 km. The stations density is higher into the region where the probability of earthquake occurrence is higher, for this reason more stations are deployed along the Apennines ridge (FIGURE 3.5). The offline simulation is performed using a software platform written in MATLAB that implements the real-time processing of data and the algorithms discussed in the previous section.

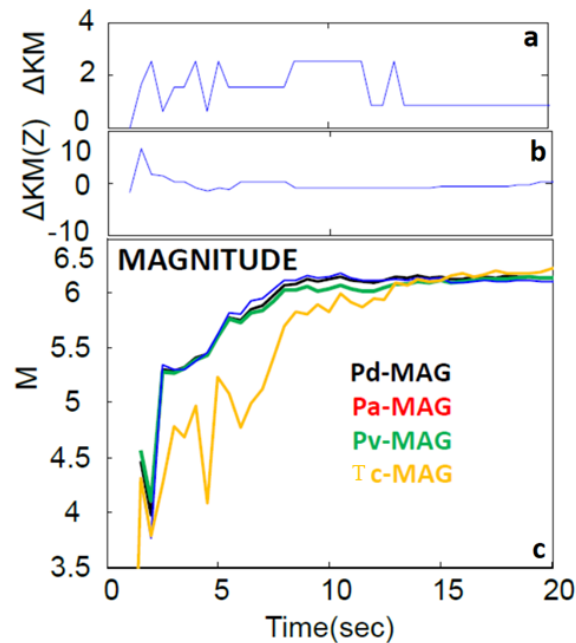


**FIGURE 3.6. SOURCE PARAMETERS ESTIAMTION (NORCIA):** (a) show the time evolution of epicentral location after the first trigger of the system. The error is the difference between bulletin INGV location and the location estimate in real-time by Quake-up. (b) is the same plot of (a) for the depth. (c) are the real-time estimation of Magnitude form  $Pd$  (black),  $Pa$  (red),  $Pv$  (green) and  $\tau_c$  (yellow).



After only three seconds from the first trigger, the RT-LOC algorithm, using the current national network deployment, is able to locate the earthquake with a stable position and an error in distance of 2-3 kilometers from the INGV bulletin location (see FOGURE 3.6 a-b). Figure 3.6c shows that the estimation of magnitude is reliable after 10 seconds from the first detection and settle on the final value 6.1.

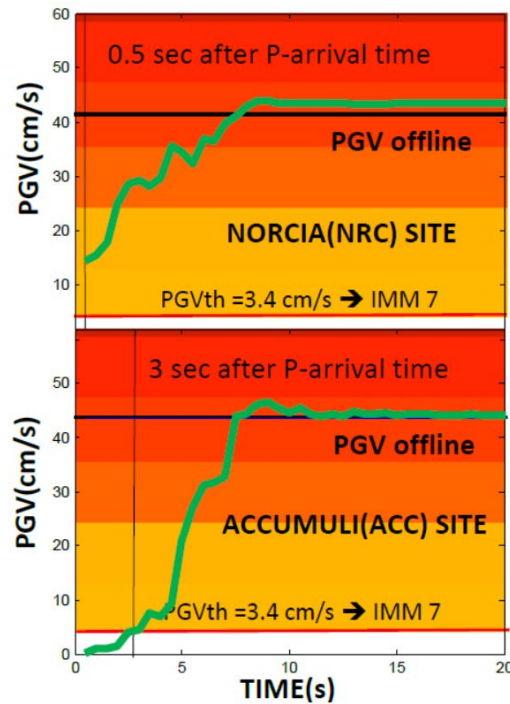


**FIGURE 3.7. ALERT EVOLUTION AT TARGET SITE (NORCIA):** The figure shows the time evolution of PGV predicted (green lines) at target site of NRC (Norcia) and ACC (Accumuli). The red lines are the threshold of critical intensity level (VII  $PGV=3.4\text{cm/s}$ ) while black lines are the PGV estimate offline on the horizontal components. The time-evolution of PGV prediction show an alert time of 0.5 seconds in Norcia at 10 km of distance from source and 3 seconds for Accumuli at 20km of distance.

The system provides an early alert in particular at the targets near the source where just after 0.5-3 seconds the intensity predicted is upper than a critical value equal to 7 (see Figure 3.7).

In order to evaluate the space and time evolution of the alert, the map of intensity is represented after 3,5,7,10,12 and 20 seconds from the first alert in figure 3.8.

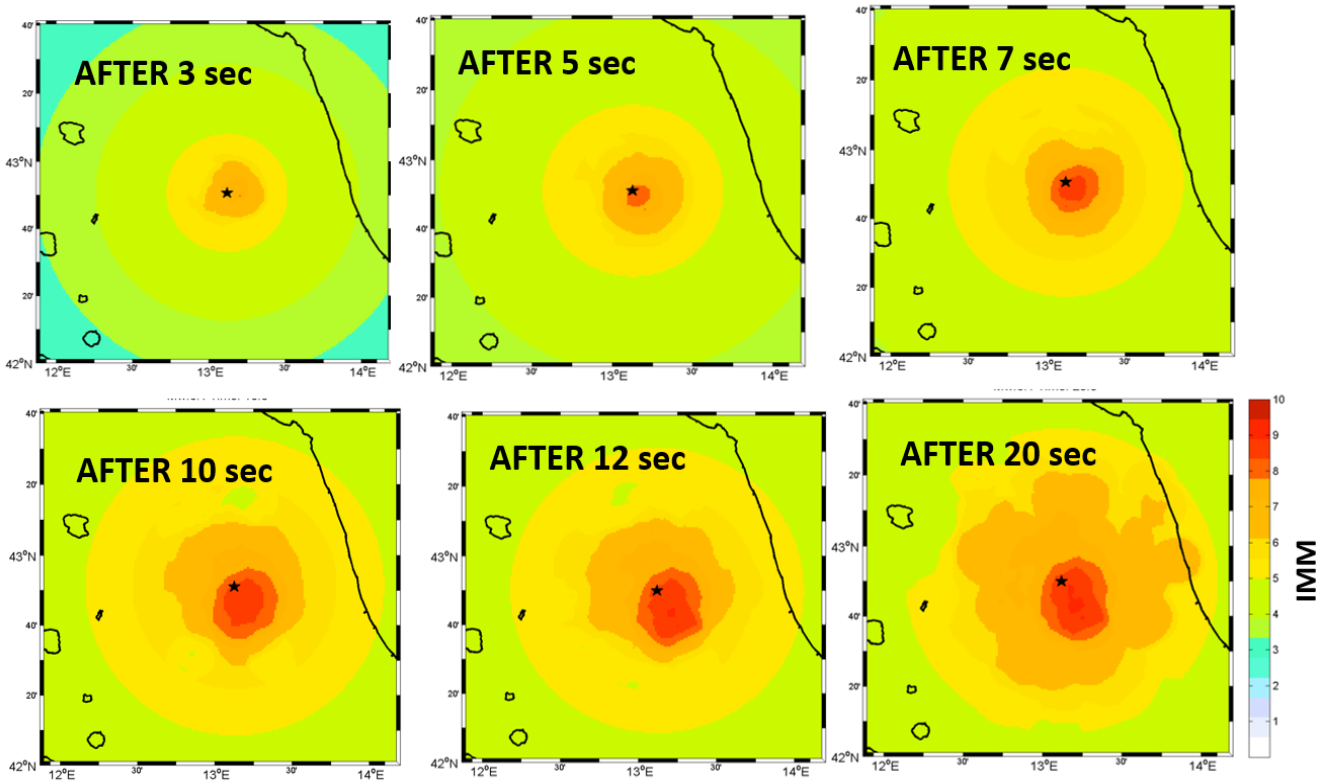


**FIGURE 3.8. PDZ MAP EVOLUTION(NORCIA):** The figure shows the Intensity map time-evolution. The intensity is estimate from PGV using the Faenza and Michelini (2010).

The comparison between the final intensity map of the system and bulletin intensity map of USGS shows that the principal characteristics of the earthquake impact is retrieved and the Potential Alert

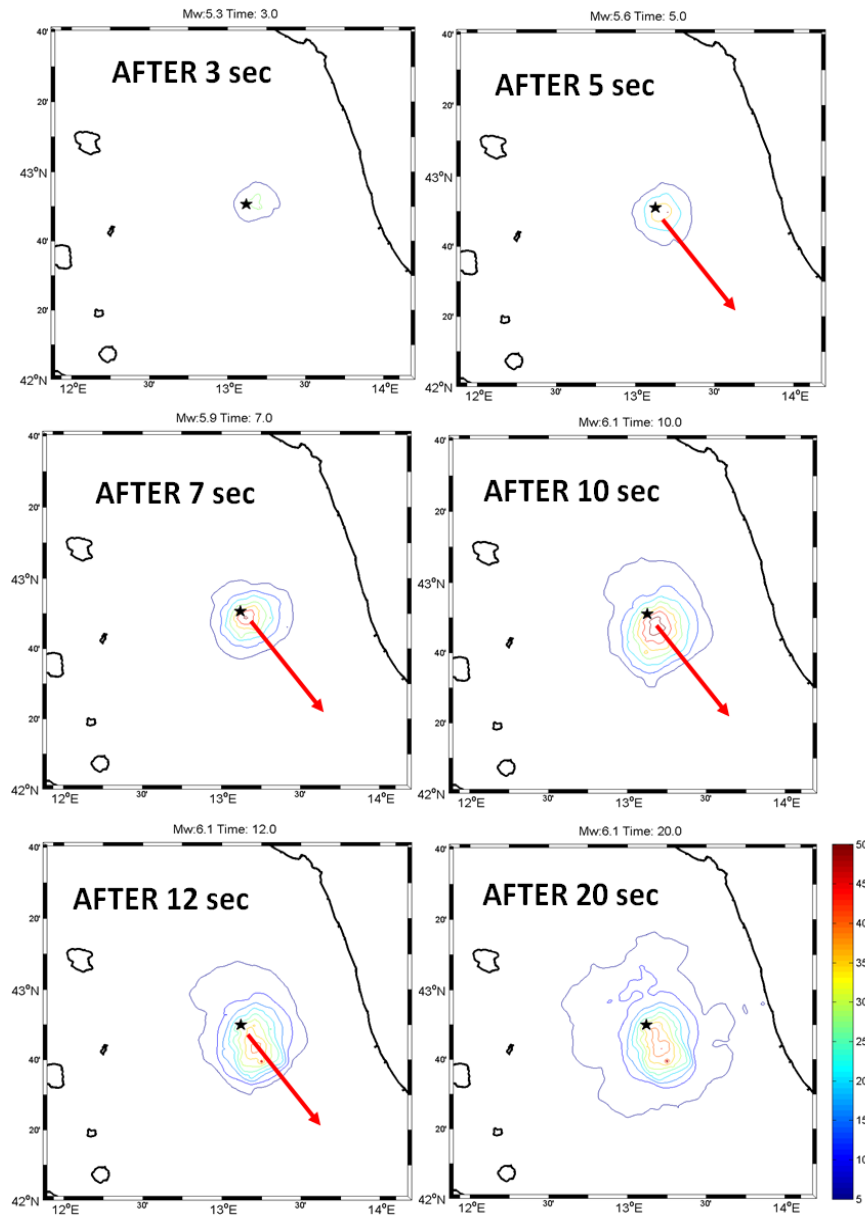


**FIGURE 3.9. PGV-MAP EVOLUTION (NORCIA):** In this figure, the evolution of the contoured PGV-map predicted is presented. The red arrow show the directivity direction predicted by the contour map.

Zone (PDZ) matches the real area where the damage was occurred (see FIGURE 3.9). In addition, the contoured map of predicted PGV shows that the north-south directivity of the fault is evident just after few seconds of the fracture enucleation (FIGURE 3.8).

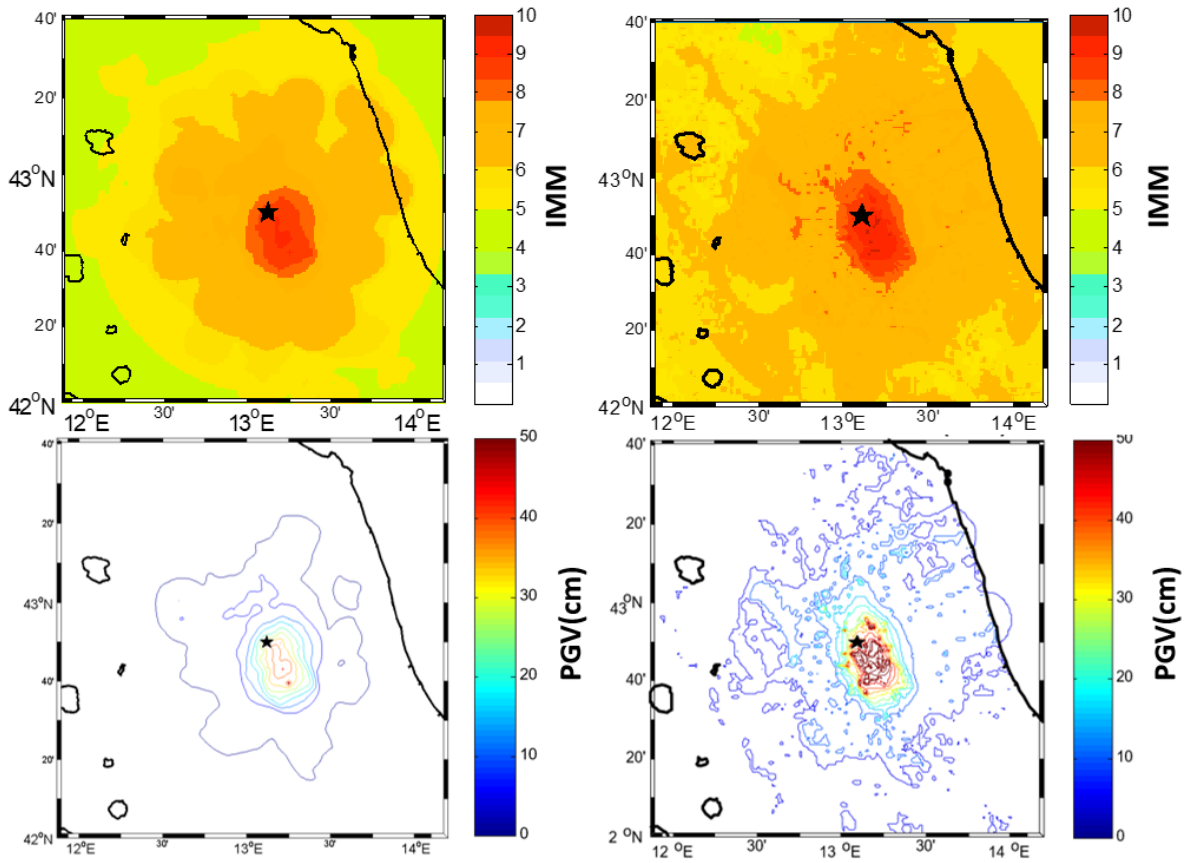


**FIGURE 3.10. MAP COMPARISON:** On the left, there are the final maps of Quake-up while on the right there are the maps of USGS bulletin for NORCIA earthquake.

### 3.3.2 Application to Japan earthquakes

With the aim of testing the method on giant earthquakes, where the source effects (i.e. directivity effect) are produced in large scale on shake maps, an application to the Japanese earthquakes was performed. The high Japanese seismicity and the very dense national seismic network have allowed a large number of seismic data to be available. In this different seismotectonic context it was necessary the recalibration of laws and data-set used for it are k-net and kik-net records of earthquakes in a moment magnitude range between 4 and 8.3. The data-set used is the same of chapter 3 for Japan calibration and using the same criteria adopted for the data-processing in the Italian context, the following laws are obtained:

$$\text{Log}(PGV) = 1.00 \pm (0.02) * \text{Log}(Pa) - 1.07 \pm (0.02); \quad \sigma: 0.32 \quad R^2: 0.71 \quad [3.28]$$

$$\text{Log}(PGV) = 0.88 \pm (0.02) * \text{Log}(Pv) + 0.54 \pm (0.03); \quad \sigma: 0.24 \quad R^2: 0.84 \quad [3.29]$$

$$\text{Log}(PGV) = 0.68 \pm (0.02) * \text{Log}(Pd) + 1.25 \pm (0.03); \quad \sigma: 0.33 \quad R^2: 0.70 \quad [3.30]$$

$$M_{wt} = 3.10 \pm (0.43) * \log(\tau_{c,x,y}) + 5.89 \pm (0.10); \quad \sigma: 0.54 \quad R^2: 0.62 \quad [3.31]$$

$$Pa_{x,y,theo} = +1.58 \pm (0.23) + 0.34 \pm (0.03) * \mathbf{M} - 1.34 \pm (0.09) * \log(\mathbf{R}); \quad [3.32]$$

$$Pv_{x,y,theo} = -1.40 \pm (0.18) \pm (0.35) + 0.50 \pm (0.02) * \mathbf{M} - 1.04 \pm (0.07) * \log(\mathbf{R}); \quad [3.33]$$

$$Pd_{x,y,theo} = -3.06 \pm (0.23) + 0.71 \pm (0.03) * \mathbf{M} - 1.47 \pm (0.14) * \log(\mathbf{R}); \quad [3.34]$$

$$M_{wpa} = 2.65 \pm (0.22) * \log(Pa_{x,y}) + 3.56 \pm (0.39) * \log(\mathbf{R}) - 3.68 \pm (0.90); \quad [3.35]$$

$$M_{wppv} = 1.93 \pm (0.08) * \log(Pv_{x,y}) + 2.01 \pm (0.16) * \log(\mathbf{R}) + 2.85 \pm (0.28); \quad [3.36]$$

$$M_{wprd} = 1.38 \pm (0.05) * \log(Pd_{x,y}) + 2.03 \pm (0.15) * \log(\mathbf{R}) + 4.33 \pm (0.24) \quad [3.37]$$

In the first japan scenario case, the testing data are used 205 records of Iwate (2008) earthquake. Figure 3.11 shows the distribution of the stations used.

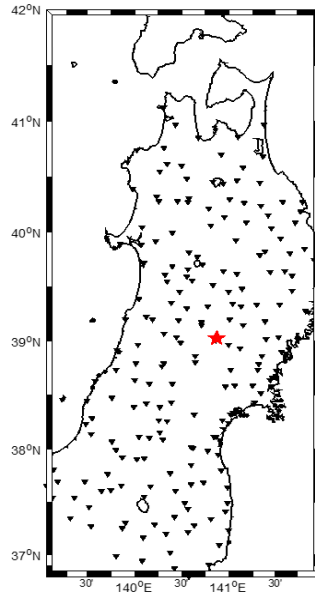


**FIGURE 3.11. STATION DISTRIBUTION (IWATE):** A map of stations (black triangles) distribution was provided. The red star is the epicentral location of the earthquake.

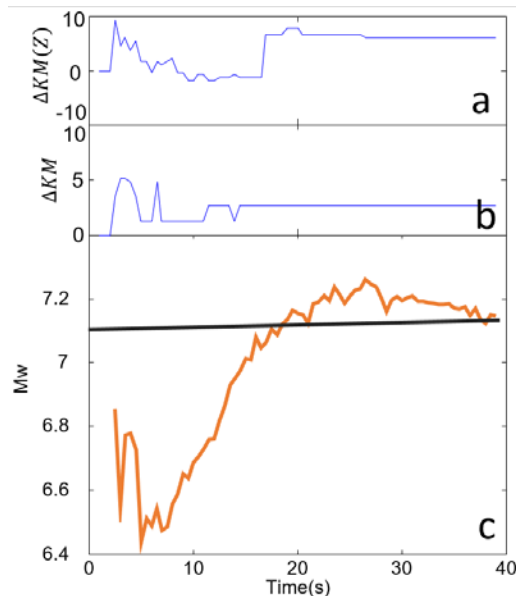


**FIGURE 3.12. SOURCE PARAMETERS ESTIAMTION (IWATE):** (a) show the time evolution of epicentral location after the first trigger of the system. The error is the difference between bulletin location and the location estimate in real-time by Quake-up. (b) is the same plot of (a) for the depth. (c) is the real-time estimation of Magnitude compared with the real-one (black-line).

With the new calibration, the system estimates the magnitude of the event upper than 6.0 just at first time of detection and upper 7.0 after 15 seconds. The achievement of the final value occurs after 20 seconds when the system provides a magnitude 7.2 (see FIGURE 3.12).

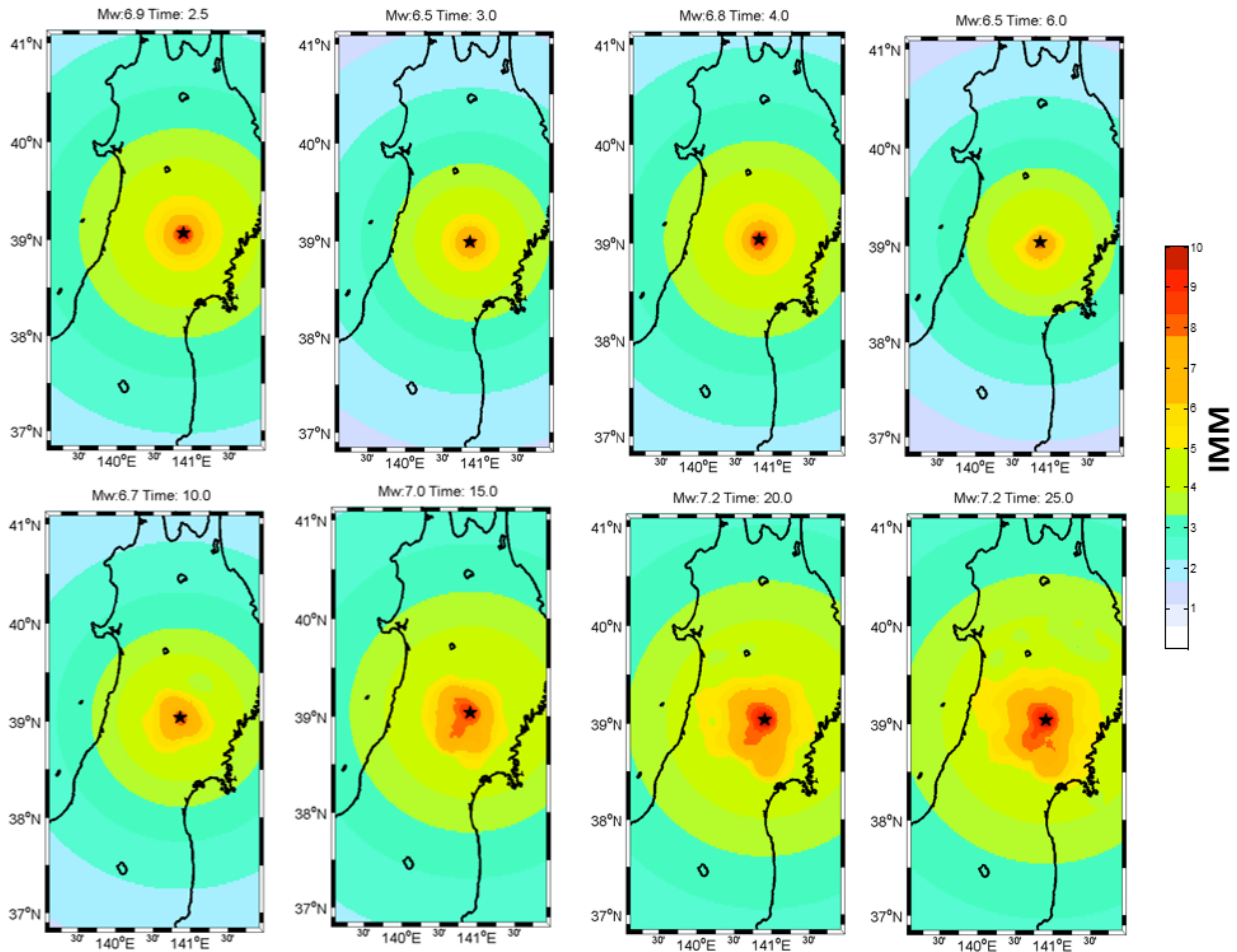


**FIGURE 3.13. PDZ MAP EVOLUTION (IWATE):** The figure shows the Intensity map time-evolution. The intensity is estimate from PGV using the Wald et al., 1999. The maps are printed, respectively from top-left at down-right, after 2.5,3,4,6,10,15,20 and 25 seconds from the first trigger.

As the previous case, the location of earthquake is reliable in particular the epicenter location (3.12b). The shake-map predicted matches the real-one pretty well. At south-west of epicenter in figure 3.15, after 15 seconds, a patch of critical intensity is shown, that indicates a fault directivity change compatible with the fault model valued with aftershock distribution and used in *Y. Ohta et al.* [2008].

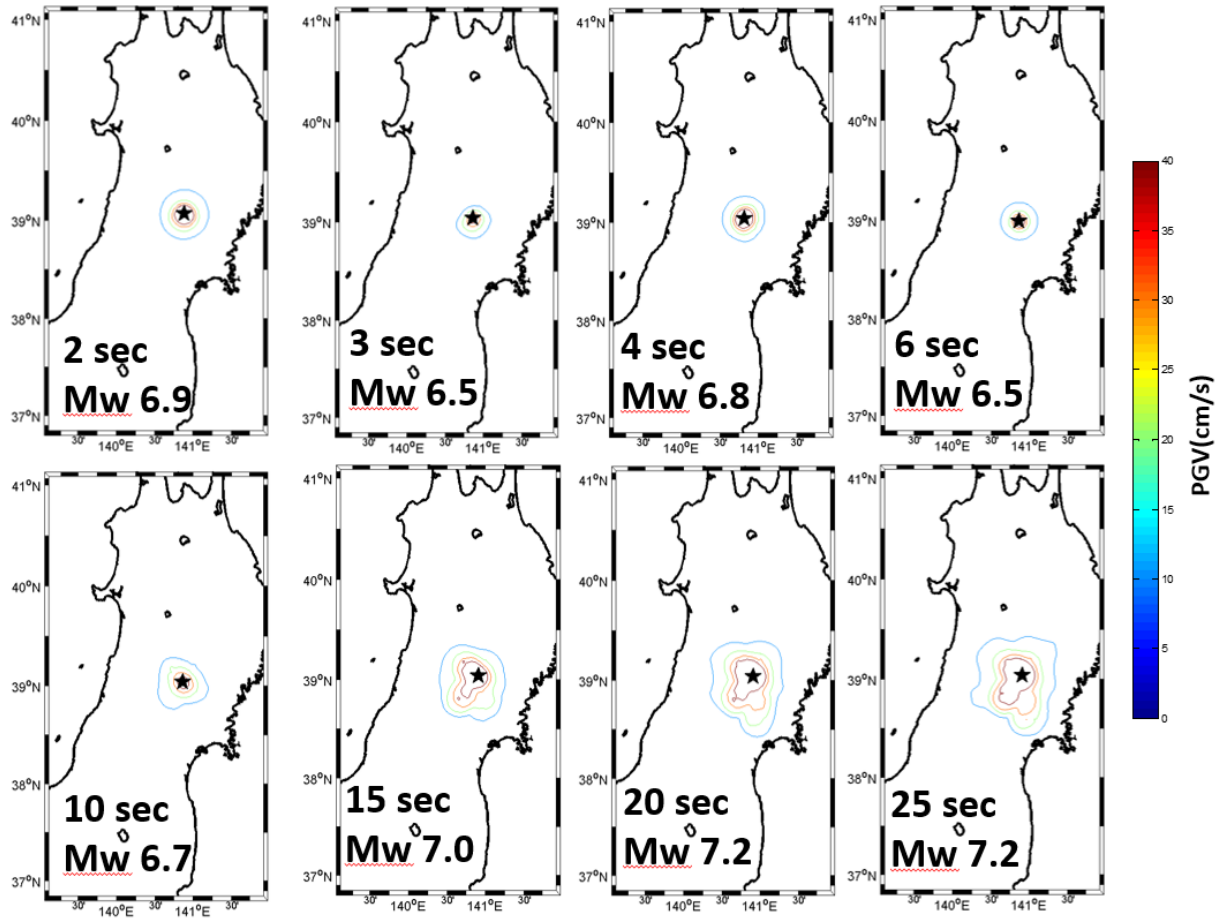


**FIGURE 3.14. PGV MAP EVOLUTION (IWATE):** The figure is the same of 3.13 but show the time evolution of the contoured PGV-map.



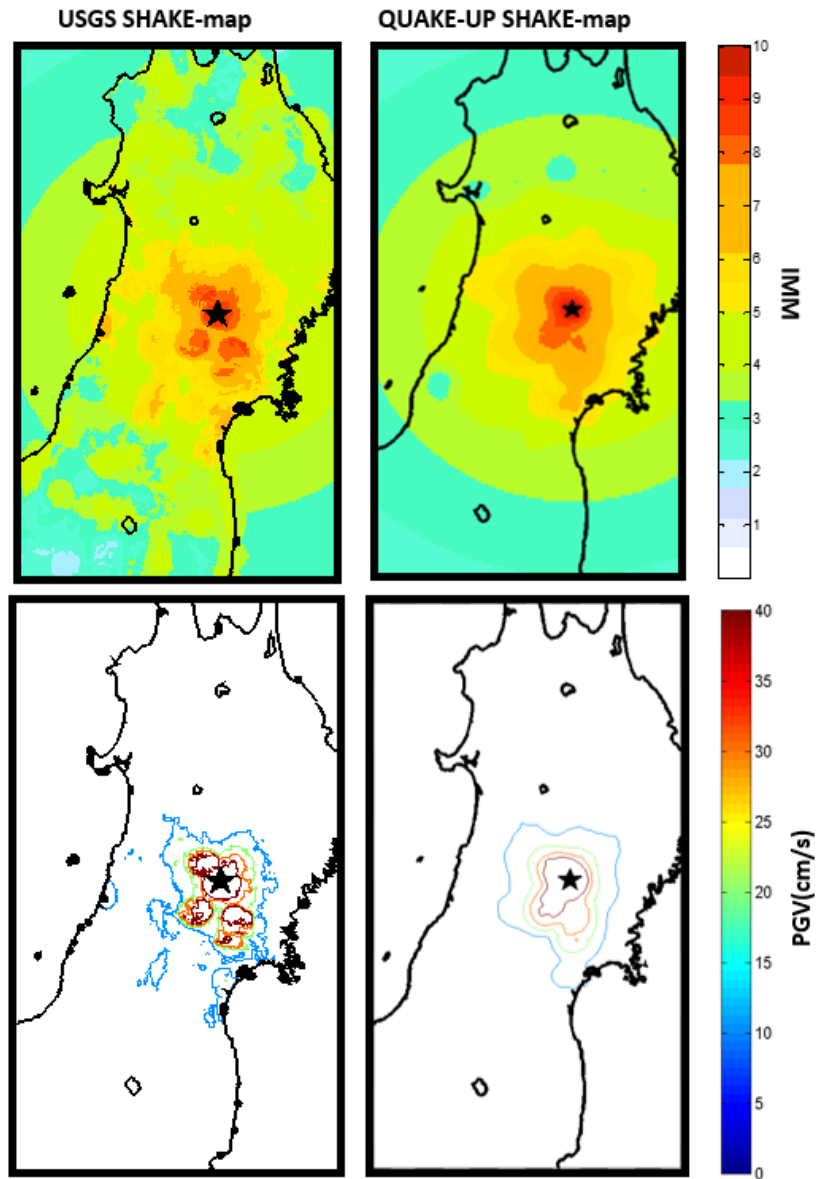


**FIGURE 3.15. MAP COMPARISON (IWATE):** The figure shows a comparison between the USGS shake-map (on left side) and the Quake-up make produced after 30 seconds from the event detection.

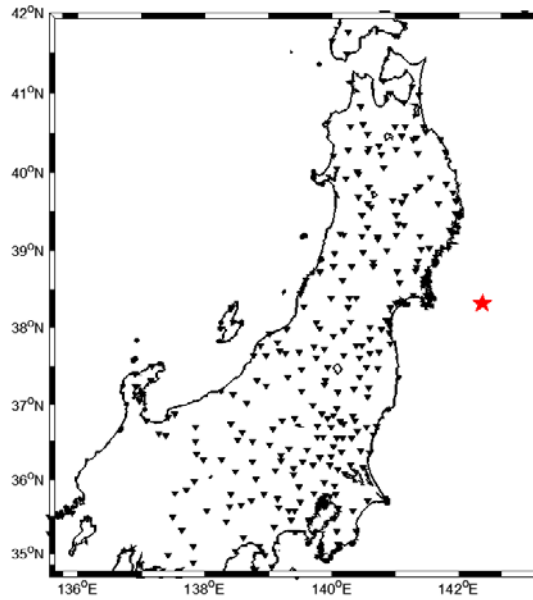


**FIGURE 3.16. STATIONS DISTRIBUTION (TOHOKU-OKI):** The figure shows the distribution of 275 stations used for the Tohoku-Oki scenario test (black triangles). The red star is the epicenter of the Tohoku-Oki earthquake.

The second Japan scenario test is the 2011 Tōhoku-Oki earthquake. The station distribution is provided in Figure 3.16. The coseismic surface displacement data observed by GEONET reveals a total major rupture length reaches about 380 km with a fault width of 90-130 km [S. Ozawa *et al.* 2011]. The earthquake was initially reported as 7.9 Mw by the USGS before it was quickly upgraded to 8.8 Mw, then to 8.9 Mw, and then finally to 9.0 Mw. One minute before the earthquake was felt in Tokyo, the Earthquake Early Warning system, which includes more than 1,000 seismometers in Japan, sent out warnings of impending strong shaking to millions. It is believed that the early warning by the Japan Meteorological Agency (JMA) saved many lives. However, the estimated intensities were smaller than the actual ones in some places in Kanto and Tōhoku regions. This was thought to be because of smaller estimated earthquake magnitude due to the limited P-wave time window used for the real-time analysis. This test is very important to prove that the use of an expanded time window can prevent saturation of laws [3.28]-[3.37], in fact, the final magnitude estimation is 9.0 provided 120 seconds after the first detection (Figure 3.17).

As shows the figure 3.17c, in first time the magnitude is about 4-5 while after 30 seconds the magnitude rise over 7 and finally over 8 after 40 seconds.

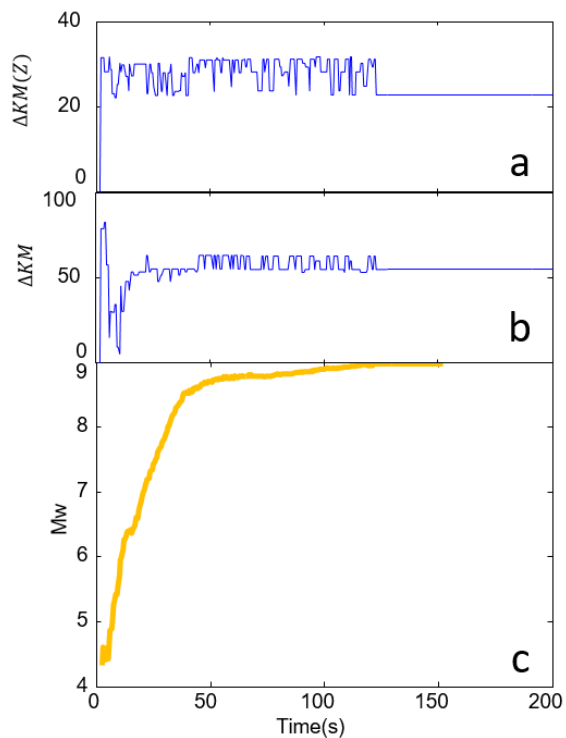


**FIGURE 3.17. SOURCE PARAMETERS ESTIAMTION (TOHOKU-OKI):** This is the same figure of 3.12.

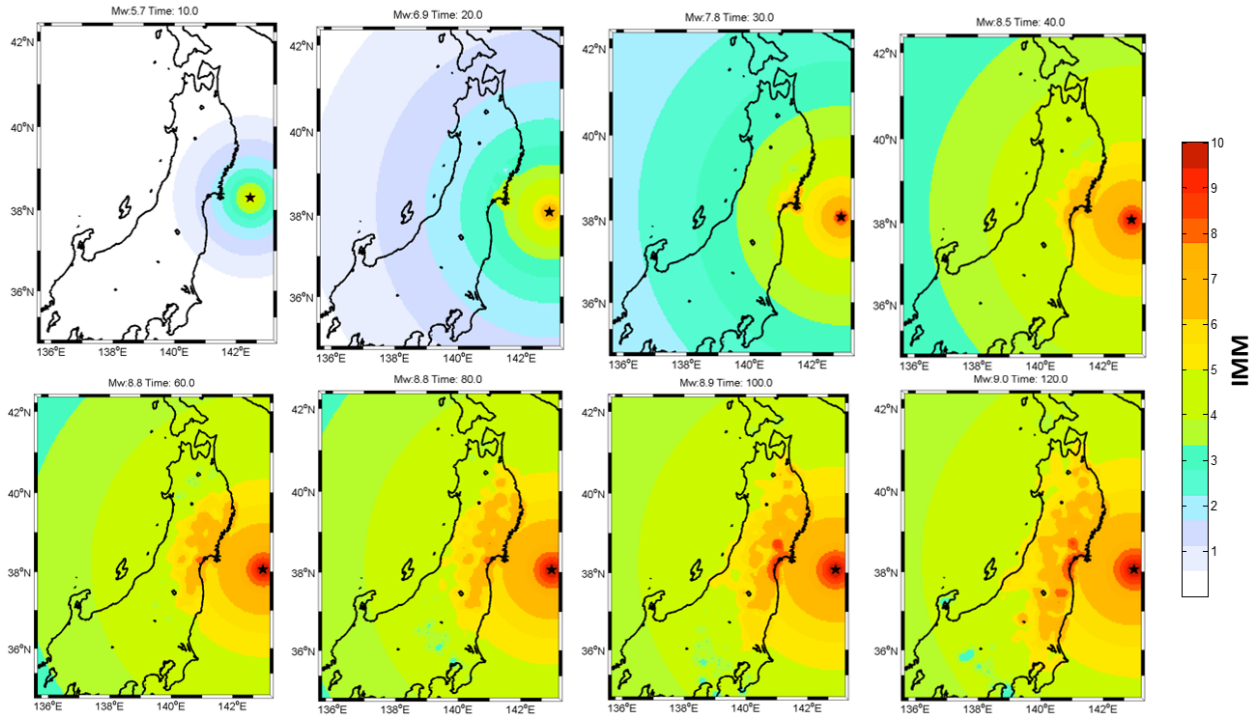


**FIGURE 3.18. PDZ MAP EVOLUTION (TOHOKU-OKI):** This is the same figure of 3.13 for Tohoku-Oki earthquake. The Map

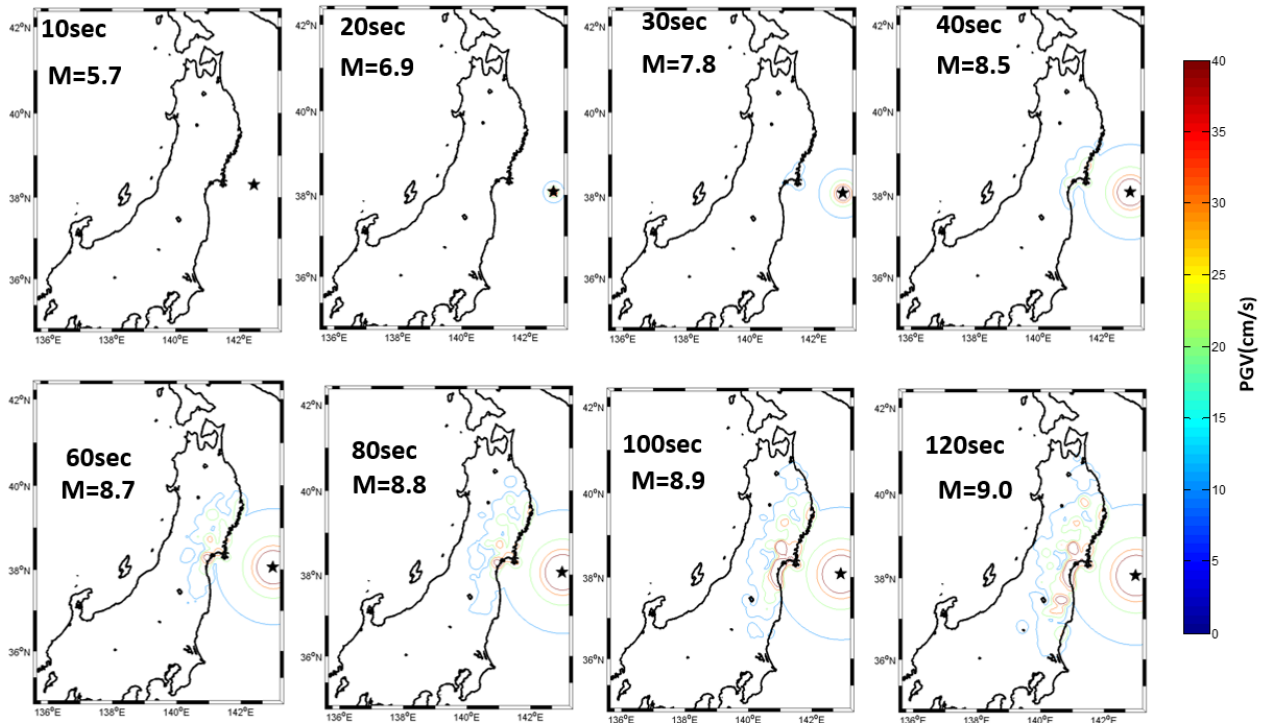


**FIGURE 3.19. PGV MAP EVOLUTION (TOHOKU-OKI):** This is the same figure of 3.14 for Tohoku-Oki earthquake. The Map is shown at 10,20,30,40,60,80,100 and 120 seconds after the event detection.

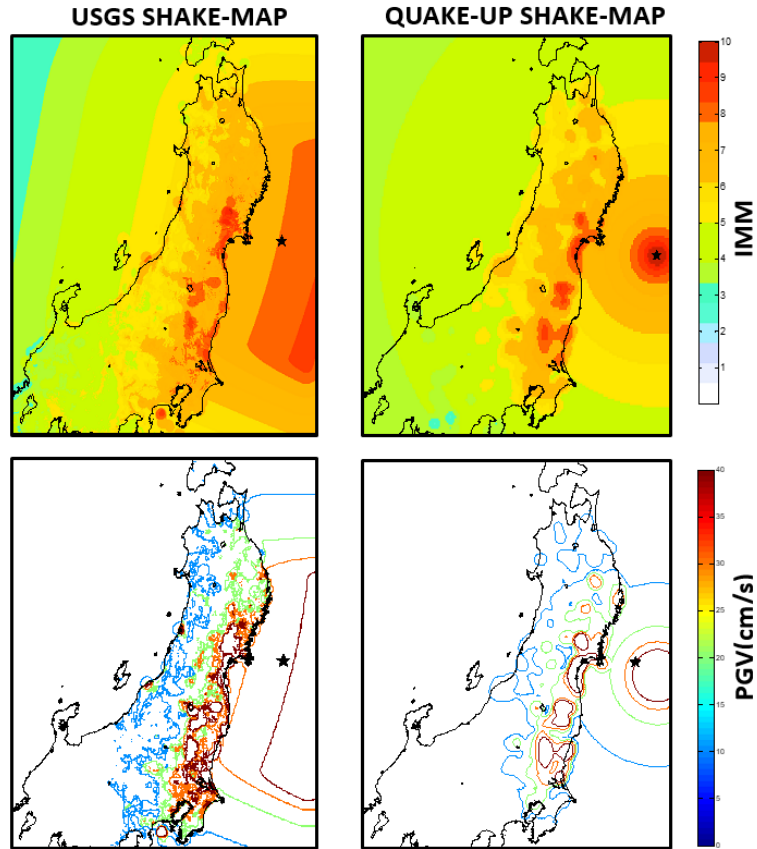


**FIGURE 3.20. MAP COMPARISON (TOHOKU-OKI):** This is the same figure of 3.15 for Tohoku-Oki earthquake.

In the final provided map the great part of strong shaking areas are recovered. At 100 seconds from first detection, critical values of local intensity, due to southern fracture propagation, are correctly predicted in Tokyo region.

### 3.4 Discussion

In this analysis the innovative and reliable real-time methodology for detection and characterization of earthquake impact was proposed. The base idea is to combine the network and on-site approaches with the aim of taking advantage of both methodologies. This strategy has allowed us to have a precise characterization of both the source parameters and the shaking intensities in the area where the seismic network is present. It is clear that for the optimal performance of system, a modern and dense network with high quality accelerometric stations and low latency data transmission was required.

The algorithm was implemented in a Matlab offline platform that simulates the real-time data analysis and was called Quake-up. In order to perform the scenario tests we have selected three events: two large magnitude earthquakes (Norcia 6.5 M and Iwate 7.2 M), and a mega-thrust earthquake (Tohoku-Oki Mw 9). Using the local data, the system was calibrated for the Italian and Japan seismic-tectonic contexts (laws [3.18]-[3.37]). As expected, the calibration process showed the differences of law coefficients especially for attenuation laws ([3.21]-[3.27] & [3.31]-[3.37]) and for  $\mathbf{M}$  vs  $\tau_c$  relationships ([3.20] & [3.30]).

During the testing phase, the performance are evaluated in term of quickness and reliability of the information provided by Quake-up. The reliability is evaluate comparing the data predicted with the earthquake bulletin information while the time-evolution of estimation was provided to show the rapidly of the methodology. In any case, the scenario tests highlighted a great reliability for the intensity map provided. The comparison with the USGS maps shows that the major features of the map are recovered (see Figures 3.10, 3.14 and 3.20), particularly in the epicentral area, where the extensive source effect is evident. The time evolution of contoured PGV-maps (Figures 3.9, 3.14 and 3.19) shows that, the effects of directivity are already clear few seconds after the fracture enucleation. In detail, the southeast directivity of the Norcia earthquake is highlighted with red arrows in Figure 3.9 just after 5

seconds from the first trigger. The rapidity in source parameters estimation is strongly influenced by the density of network in the epicentral area. The fastest convergence for Magnitude and Location is obtained for the Norcia earthquake scenario, where the density in the epicenter is highest (about 0.9 stations/ $km^2$ ). In this case, the rise-time of Magnitude estimation is 8-9 seconds after the first trigger (Figure 3.6). In Iwate scenario case, the convergence is obtained after 20 seconds with a network density in epicentral area about three times lower than Norcia scenario. From point of view of the alerts, the use of on-site predictions benefits the quickness of alert in particular for sites very close to the source, as for Norcia site in the first scenario case (see Figure 3.7) where the alert is give after 0.5 seconds form the event trigger.

The system is able to select the P-wave part of signal using the real-time polarization filter that permits the expansion of the portion of signal processed indefinitely without worrying about the inclusion of other seismic phases. This advantage allows to avoid the saturation of correlation laws used for the final estimation of magnitude and intensity. This is more important for the large earthquakes (such as the 2011 Tohoku-Oki earthquake), where the duration of the fracture at source is upper than 50 seconds [H. Yue, 2013], for this reason the portion of signals useful for the reliable estimation of source parameters and local intensities are higher than the arrival times of other seismic phases (as S-wave). The polarization filter strategy is necessary to estimate the peak amplitude of the P-wave signal on the expanded time window avoiding the overestimation. The Tohoku-Oki scenario test shows a convergence of the magnitude estimation after 50 sec, compatibly with the duration of source time function, and the plateau is at 9 as the Bulletin value (FIGURE 3.17). The location is not reliable due to the low azimuthal coverage of network, distributed all over the western side of the earthquake (see Figure 3.16), and an unsuitable velocity model (Ueno *et al.* 2002) for offshore event. Contrariwise, the intensity map obtained is reliable and the area of critical shaking are well recovered. The southern

directivity of the fracture process is evident from the map of PGV, after 120 seconds after the event trigger (Figure 3.19) and the final intensity map is very similar to the USGS shake-map (Figure 3.20).



# Chapter 4: Early warning system embedded into a seismic station

## 4.1 Introduction

In this chapter we will describe the research and development phases aimed to implement the SAVE algorithm in an embedded system, which is able to record the seismic waves, process the data acquired and provide to the end-user an alert. The project is the result of a 6-month internship period in a company, followed by a co-tutor, Dr. Claudio Martino, technologist at the Osservatorio Vesuviano (INGV institute) in Naples, to acquire technical knowledge and deal with technological development. The company selected for the researching cooperation is the TMEsrl (Test and Manufacturing Engineering), which has large experience in designing and manufacturing of software and hardware solutions. During this period, a synergic collaboration has been developed due to the necessity of performing the hardware design of the data-logger and the computational analysis unity able to run the SAVE algorithm discussed in the first chapter.

The station is able to acquire the high quality seismic data from one or two 3-components seismic sensors with a maximum of 6 separate channels. The records are provided via TCP-IP port using a seedlink protocol and the local storage is done.

The digitization is performed with six 32-bit Analogic-Digital-Converter modules, able to digitalize data with high amplitude resolution. The recorded data is adequate for seismic analyzes performed by a low power mini-pc embedded. The merger of my scientific expertise and the engineering skills of the TME company has resulted in the development of prototypes currently being tested at some strategic

sites selected in the area of Irpina, where the ISNET (Irpinia Seismic NETWORK) is currently installed and working.

## 4.2 MOMA project

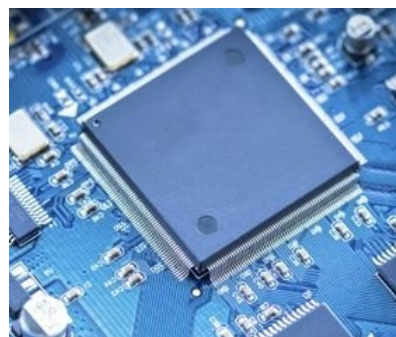
The project MOMA, acronym of MonitOring seisMic stAtion, was born in order to develop an advanced low-power station that consists of a data-logger able to digitalize the analogic signal, provided by the seismic instrumentation, storage and send the records and waveforms via internet network. The step forward was to integrate an on-site EEWS able to define a critical alert level and do preventive automated risk mitigation actions. The best strategy to provide a more reliable alert is to use external high-quality accelerometers and for this purpose, two versions of the MOMA prototypes were made, with internal and external sensors.

### 4.2.1 On-board sensors

The station was equipped with an internal sensor, consisting of two different types in order to provide the accelerometric and velocimetric signal. The first one is a triaxle MEMS accelerometer with a full scale settable to 2g or 6g. The sensor sensitivity is  $50 \mu g/\sqrt{Hz}$  at a full scale of 2g. This sensitivity does not allow the sensor to record small seismic events, but only strong ground shakes ( $M > 3.5$ ) with epicentral distance less than 10km.

#### Accelerometer

- Full scale range:  $\pm 2g$  or  $\pm 6g$
- Low power consumption ( $\cong 1 \text{ mW}$ )
- Acceleration noise density ( $\pm 2g$ ) :  $50 \mu g/\sqrt{Hz}$



- High shock survivability (10000 g)

The velocity is recorded by a 3 channel geophone with the resonance frequency of 4.5 Hz. This type of sensors is usually used for monitoring and recording microsismicity ( $M < 3.5$ ).

### Geophone

- Frequency (Hz): 4.5 +/- 10%
- No power consumption.
- Distortion (%): <0.3
- Damping: 0.6 +/- 10%
- Coil Resistance ( $\Omega$ ): 375 +/- 5K
- Sensitivity (V/m/s): 28.8 +/- 7.5%
- Max Coil Excursion (mm): 4mm
- Temperature Range ( $^{\circ}\text{C}$ ): -40 / +70



In any case, the maximum amplitude of the analogic signal provided by the internal sensors are limited at 2.5 Vpp.

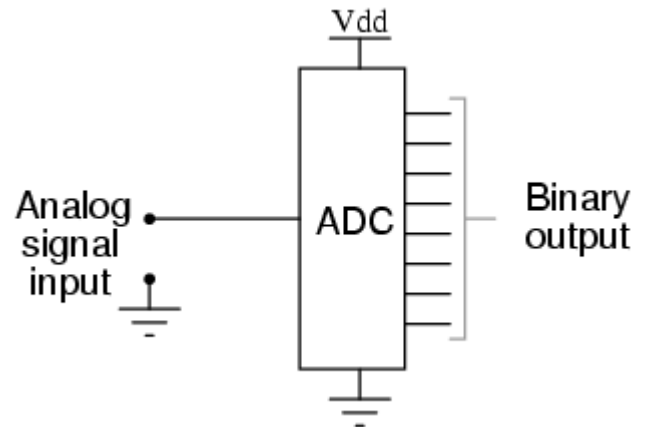
### 4.2.2 Analog to digital conversion

For the digitalization operation, the A/D conversion is based on 6 single-chip analog to digital converter with an integrated, low-noise programmable gain amplifier and two channel input multiplexer. The converter uses a fourth-order delta-sigma ( $\Delta\Sigma$ ) modulator that provides high-

resolution performances with than more 132 db SNR (@100 SPS), low noise ( $5 \text{ nV}/\sqrt{\text{Hz}}$ ) and high input impedance allowing easy interfacing to sensors over with range of gains.

### Data Acquisition (ADCs):

- Input level: 5Vpp (for internal sensors) or 40Vpp (for external sensors).
- Impedance: 16k $\Omega$
- HW Gain: 1 to 4
- Type: Individual 32-bit Delta Sigma converter per channel (synchronuos)
- 100 sps  $\approx$ 132dB (RMS noise to RMS clip)
- Sampling rates: 125, 250, 500Hz



The data stream provided by A/C are acquired at the CPU module capable of decimate using a FIR causal filter and formatting data in the seedlink standard protocol and synchronize the bit-stream to the periodic signal produced by the integrated gps antenna with precision of  $\leq 20 \text{ ns}$  (Clear sky). The CPU module is developed using a low power ARM Cortex-M4 and 512kb of RAM memory sufficient to manage a light firmware. The data buffer is storage on internal flash-memory (for more than two months of data storage) and ready to processing.

### 4.2.3 Timing module (GPS)

The Timing module is based of the LEA-M8T module. LEA-M8T deliver high integrity, precision timing in demanding applications world-wide. Support for BeiDou, GLONASS and Galileo constellations enables compliance with national requirements. Enhanced sensitivity and concurrent

constellation reception extend coverage and integrity to challenging signal environments. Survey-in and fixed-position navigation reduce timing jitter, even at low signal levels, and enable synchronization to be maintained with as few as one single satellite in view. Same technical specifications are reported below:

### Features - Timing

- Timing accuracy Clear sky:  $\leq 20$  ns
- Time-pulse frequency: 0.25 Hz – 10 MHz
- Time-pulse jitter:  $\pm 11$  ns
- Time-mark resolution: 21 ns
- Integrity reports: RAIM active, phase uncertainty  
time-pulse rate/duty-cycle
- Operating temp:  $-40^{\circ}$  C to  $85^{\circ}$  C
- Storage temp:  $-40^{\circ}$  C to  $85^{\circ}$  C



LEA-M8T  
17.0 x 22.4 x 2.4 mm

The signal generated by GPS module (1kHz) is delivered to A/D converter in order to synchronize it with this reference signal and the final digital stream data is acquired by CPU module through 6 SPI (Serial Peripheral Interface) ports, synchronous serial communication interfaces.

The next step was to organize the data into a local database of daily records and provide the stream of data with a low latency (lower than 0.3 sec) at one or more client instances. All these tasks are managed by the Linux embedded system on a single-board computer designed around the Microchip AT91SAMG25 (ARM9@400MHz MPU) equipped with a 256mb ram memory. The Linux system is

customized in order to hosts SeisComP (the SEISmological COMMunication Processor) software and others tools able to manage the mini-seed data. SeisComP platform acquires the data from a serial port of a CPU module and manages a seedlink server in charge of management of one or more client connections via TCP/IP port.

### 4.3 End-user interface

The configuration webpage is provided, built using HTTP and java-script programming language.

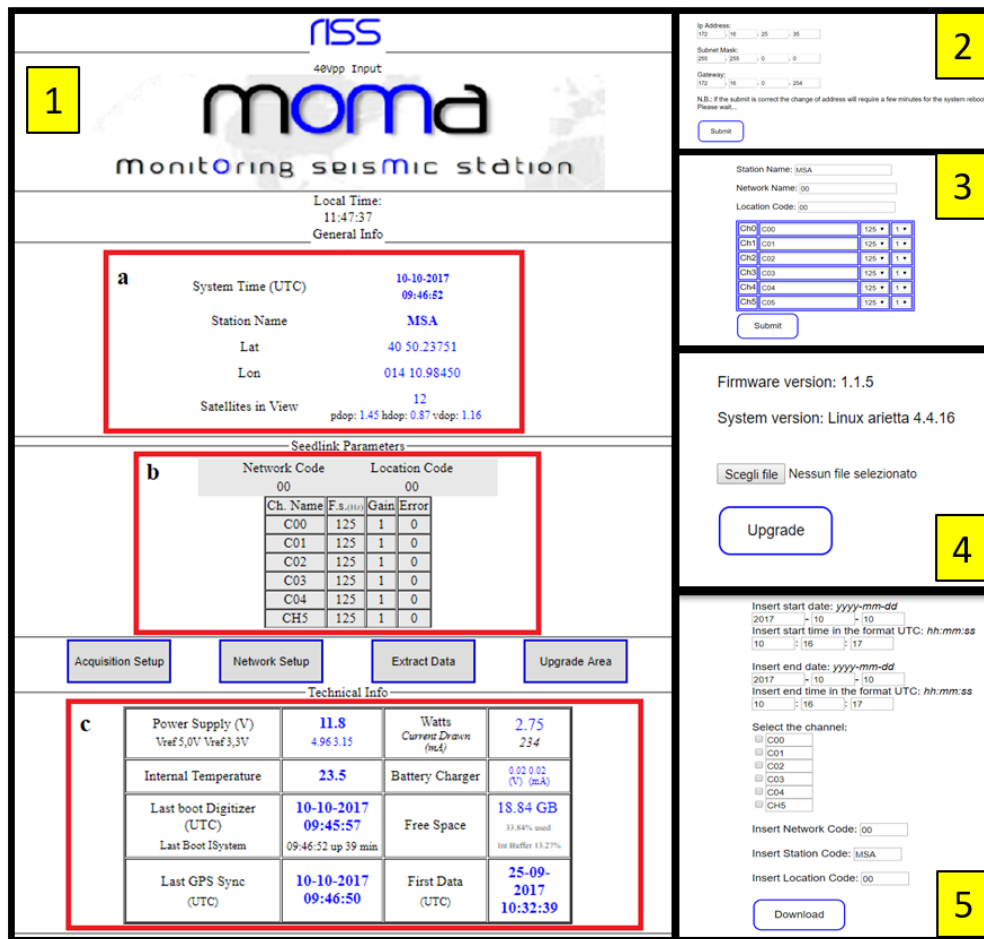


**Figure 4.1: MOMA WEB-PAGE.** (1) Panel 1) Shows the home-page of MOMA web interface. The mains information of page are highlighted with red square: (a) info about the system times, Station name and geographical coordinates and GPS state; (b) are the channels information about name, sampling rate, Gain and status; (c) are the information about the Power voltage and consumption, internal temperature, date of the last system boot and last GPS fix, free disk space and battery charger. Pages (2) (3) (4) and (5) can be accessed through a specific button on the main page. On (2) page, the user can set station ip, network sub mask and gateway. In (3), channel names, sampling rate gain and stations parameters can

be set. In (4) the information about the software are provided and it is possible to update the digitizer firmware. At last, on page (5), the user can download from the station the local dataset the data in mseed format selecting channels and stations information.

In the web page, the end-user can customize any station information as: station name, network name, location code, location coordinates. Furthermore, the user can change the acquisition parameters such as sampling rate, able or disable channels and change channel names. The webpage gives the same information: the connection state, CPU usage and temperature and the download section is provided in order to recover data from the local data-base.

## **4.4 EEWS for MOMA**

Originally, SAVE algorithm was implemented in a C++ code, which was designed to be used on PC computers. A customization of the software was made in order to run the code on low power integrated systems. The graphic part of the platform was eliminated and the user screen was replaced with a webpage that provides the number of declared daily events and the respective classification of intensity, magnitude and expected hypocentral distances. The source code and the necessary libraries were then recompiled for ARM environment. The final version of software was installed and tested on prototype stations located in Irpinia region. The software performance and proper operation is monitored analyzing the log files provided in real-time and located in the flash memory.

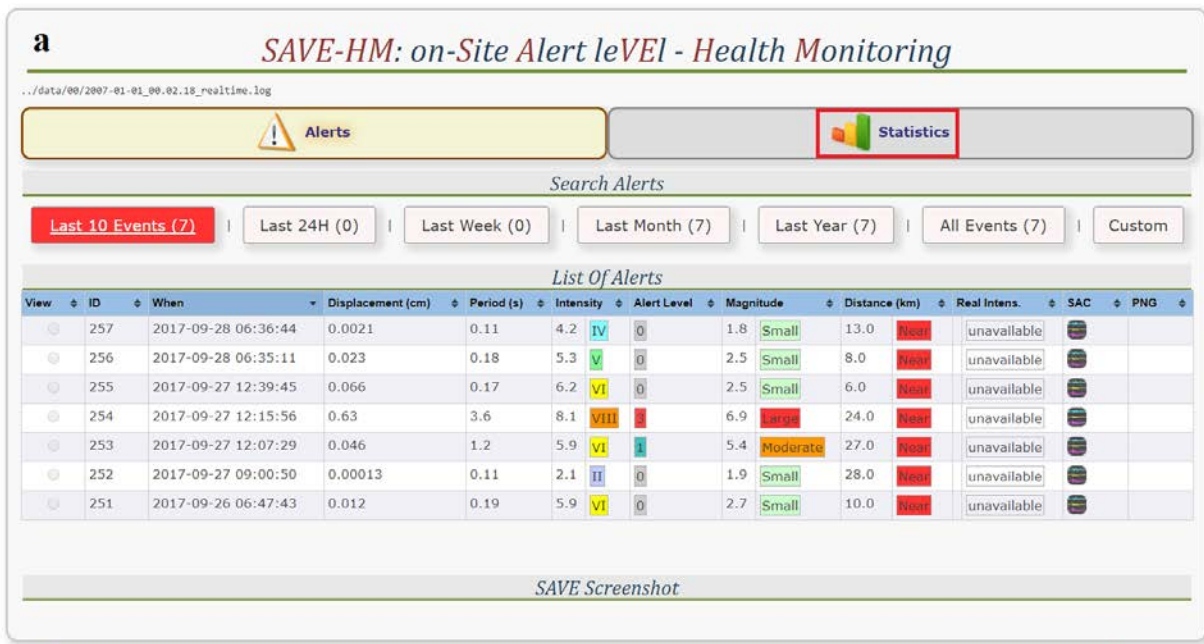


**Figure 4.2: SAVE WEB-PAGE.** (a) Shows the home page of the SAVE web page. The information about the last alerts is given. The time window of list can be selected as the last 24h, week, month and year. The user can select all event list or customize the research. The list provides information about the time (UTC) of alerts and the classification of events in the term of Magnitude, distance and intensity declared. Using the statistics button on the homepage, the (b) page is provided, where are the histograms of the local intensity declared in function of time of declaration and intensity level predicted.



## 4.5 Spectral straightening of the Geophone response

The geophone at 4.5 Hz is a useful sensor to acquire the surface microseismicity ( $0.1 < M < 4$ ) in particular, in particular, the possibility to improve the performance of this sensor was investigated.

In the final part of this analysis, three seismic events recording at the MOMA station are collected. The signals are compared with a reference instrumentation located in the same site and the site located in Rocca San Felice (AV) where the station RSF3 of ISNet network is installed. RSF is equipped with a broadband velocimeter TRILLIUM-40S of Nanometrics and an accelerometer Guralp CMG-5T. The traces recorded at the same time and at same site by MOMA and TRILLIUM have been used in order to expand the useful spectral acquisition band of Geophone in the way described below.

The exact spectral response of the Geophone is recovered using the spectral ratio between the amplitude spectrum of the record at Geophone and the same signal recorded at TRILLIUM corrected by its instrumental response, which is best explained by the following equation:

$$G_{resp} = \frac{(G_{resp} * Signal)}{\left(\frac{Trillium_{resp} * Signal}{Trillium_{resp}}\right)} \quad [4.1]$$

Where the “\*” and “/” are respectively product and division in the frequency domain while  $G_{resp}$  and  $Trillium_{resp}$  are respectively the Geophone and Trillium frequency response. Finally  $Signal$  is the spectrum of the signal without the instrumental response.

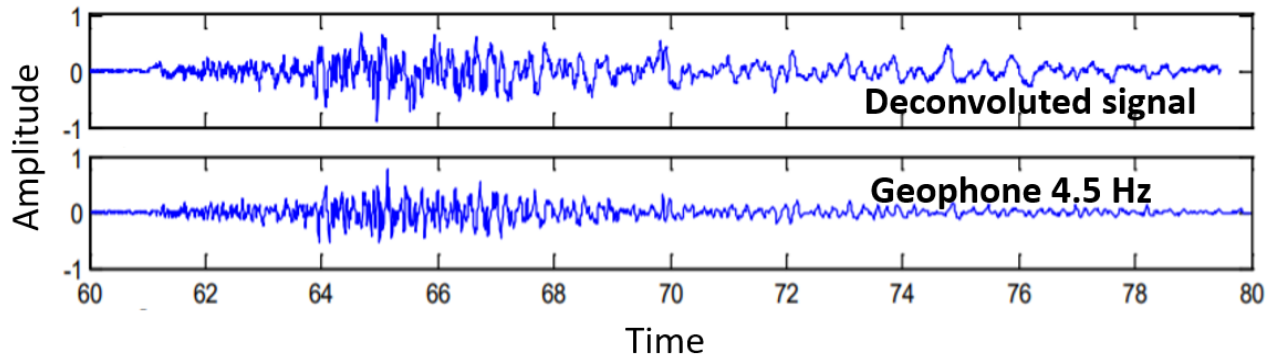


**Figure 4.3: SINGAL COMPARISON.** The figure shows a comparison between the vertical component records by internal geophone of MOMA and the same signal records by trillium and corrected for the instrumental response. The example is an earthquake of the local magnitude 2.2 occurred in Irpinia region.

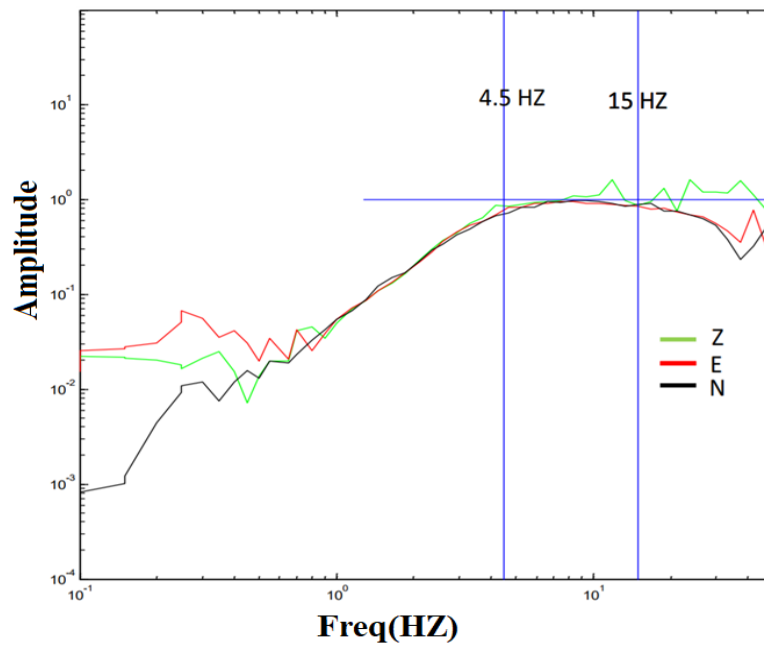


**Figure 4.5: Geophone spectral response.** The figure shows the instrumental response of the Geophone for vertical (green line) east-west (red line) and north-southern (black line) components using the relation [4.1] and the logarithmic spectral smoothing.

The  $G_{resp}$  (Figure 4.5), estimated by this procedure, has been used to correct the signal recorded by the Geophone and the low frequency instability is corrected with a filter Butterworth 2 pole high pass with corner frequency of 0.5 Hz.

Through this processing was possible to retrieve, with good quality, the signal spectrum between 0.5 and 4.5 Hz (see Figure 4.6.), otherwise certainly damped by the sensor.

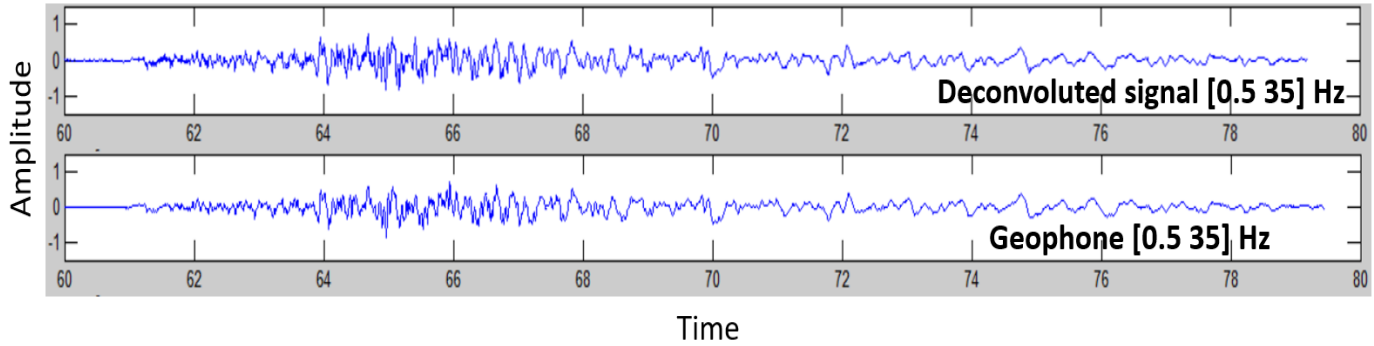


**Figure 4.6: Signal comparison after the spectral straightening.** The figure shows the new comparison of the same signal of figure 4.3 the deconvoluted signal of Trillium filtered with a Butterworth band pass filter [0.5 35] Hz and the Geophone signal corrected using the  $G_{resp}$  and filtered with the same Butterworth bandpass filter.

## 4.6 Discussion

The MOMA project is a work-in-progress task managed by RISS.srl, an university spin-off supported by RISSClab research group. To give my contribution to this project, a 6-month internship at TME.srl (partner of Riss.srl) was planned. During the internship, the hardware development phases of the station have been followed and the implementation of SAVE EW system in MOMA was done.

In the present chapter, the technical details about the implementation of the data-logger and on the internal sensors were provided (section 4.2). In the section 4.3 and 4.4, the end-user interfaces of the data-logger and SAVE alert system have been described while, in section 4.5, a procedure of spectral straightening of internal geophone response, aimed to increase the sensor bandwidth, was described and tested with good result on a seismic signal (see Figure 4.6).

## Conclusions

In chapter 1 we focus on the development of a rapid, stable, but approximate methodology for an on-site EWS.

The work described in this chapter is the result of a collaboration with the research team (RISSClab). The methodological part and the data processing techniques were developed in collaboration with the research group while the data-set formatting, refinement of the EW methodology and the testing phase was the result of my work in the first year of PhD.

The methodology we described is robust, since it requires the fulfillment of strict criteria for testing the quality of the real-time streaming data. Among them, the  $SNR$  is used to distinguish spurious transient signals from true earthquake detections, while the  $P_d/P_v$  ratio is a powerful way to discriminate noisy waveforms, which are still affected by low-frequency drifts after the double integration and filtering operations. The correct evaluation of the initial peak displacement in real-time is the first strategy to minimize the percentage of over/underestimations of the expected earthquake magnitude and ground shaking at the target site.

For most of the analyzed cases, SAVE is able to deliver a correct warning shortly after the P-wave detection. A time window of 1 second is indeed enough to provide reliable information about the main source parameters and the expected ground shaking at the target site. The estimates are then refined (or confirmed) when longer P-wave time windows are used (2, 3 seconds). The SAVE algorithm has been implemented in a seismic station through the development of an embedded system called MOMA. The technical details and project description are provided in chapter 4.

Subsequently, in chapter 2, a refined and innovative approach for on-site early warning system is explained and tested. My contribution in this work has been to develop all aspects of the described methodology and performance evaluation in cumulative and scenario tests. The data-set formatting is

the result of a previous job.

In the proposed approach to on-site EEW, the initial amplitude parameters are continuously measured along the ground motion recordings and the use of limited P-wave signals, used in SAVE approach, has been replaced by the concept of expanded P-wave Time Windows. Standard approaches to EEW, which are based on the use of short portion of the P-wave signal, may significantly fail when dealing with the very large events. The empirical regression relationships between these parameters and magnitude, based on few seconds of P-wave, saturate beyond a magnitude threshold that can be estimated into the range 7-7.5 (*Kanamori, 2005; Rydeleck and Horiouchi, 2006; Rydeleck et al., 2007; Zollo et al., 2007; Festa et al., 2008*). This saturation is due to the imaging of a small portion of the fault plane. When an earthquake rupture extends for hundreds of kilometers on the fault, the large asperities possibly encountered far away from the hypocenter may control the rupture dynamics. The analysis of strong motion data of the Mw 9.0, 2011 Tohoku-Oki mega-thrust earthquake confirmed that larger time windows are necessary to properly estimate the size of the ongoing event (*Colombelli et al., 2012b; Colombelli et al., 2014*). The possibility of expanding the observation time window allows capturing longer portions of the rupture process and lower frequencies radiated from the source, thus possibly avoiding the saturation effect causing the earthquake magnitude underestimation.

In terms of practical operations, a possible risk when expanding the P-wave time window is the inclusion of S-waves. The S-wave amplitude, if not properly considered, may lead to overestimations of the predicted ground shaking level. To avoid this effect a robust and reliable algorithm to generate a “P-wave dominant” signal was proposed and tested. Cumulative statistics indicate false alerts decrease due the application of this strategy. Another important aspect is that the single parameters approach, to predict the local intensity, has been replaced by a multi-parameter approach. The overall statistics confirmed that the performance of the system significantly improves when the combination of three parameters is used, with a relevant increase of successful alarms and a substantial reduction of false

alarms. The empirical combination of three different parameters provides a broader insight into the ongoing phenomena, while keeping the methodology, at the same time, reliable and as simple as possible. Compared with the standard on-site methodologies, this approach is likely to provide reliable warnings and more robust prediction of potential earthquake damaging effects.

The proposed methodology is conceived to operate as a single-station, threshold-based, EWS and is expected to improve the reliability of an on-site system, for those cases where no information or constrain on the earthquake source is available in real-time. On-site EWS are extremely useful both when the target is too close to the source area and when a high level of accuracy is required in real-time for the warning declaration. Contrariwise, a weak point of the single station approach is the false alarms due by the poor information useful to define the alert. Therefore, a multi-station approach is necessary to improve the reliability of the alert and in this way, in chapter 3, the development of a network based system has been done. The idea of this approach is based on the interpolation of data obtained from individual stations. The methodology proposed has proven to be innovative, reliable and useful to provide a rapid alert message strictly constrained. In addition, a complete characterization of earthquake impact is provided using a consolidated algorithm of data interpolation (like USGS map) able to build a realistic map of predicted impact. All scenario cases confirm a good performance of the system in term of source parameters estimation and reliability of predicted intensity map where extended source effects are visible already after few seconds form the event trigger. The quickness of source parameters convergence significantly depends on the network density around the epicentral area and the duration of the source time function. In conclusion, the test performed during these analyses and the results obtained, show that the multi-parametric approach is useful to increase the reliability of the system. Also, the robust processing of data in order to increase the reliability of parameters used for predictions is necessary and crucial for a correct definition of alerts. In this way, the development of more robust criteria for bad quality data exclusion and data adaptive filtering are key objectives for

having a reliable and performing system, and for increasing the statistical reliability of the automated tools. Furthermore, the possibility to obtain a complete characterization of the ongoing earthquake in term of source parameters and expected shaking is possible using a dense network deploy on the area of interest. A future perspective is the development a software platform that implements the Quake-up real-time system and end-user visual display where the most relevant pieces of information will be displayed and updated as soon as new data are available.

Chapter Three is the synthesis of work done in these three years of PhD and uses the methodologies described and developed in Chapters 1 and 2. The technique for the shake map building and all tests described are the product of the work done during the last year of PhD.

## References

1. Alcik, H., O. Ozel, N. Apaydin, and M. Erdik (2009), A study on warning algorithms for Istanbul earthquake early warning system, *Geophys Res. Lett.* 36, L00B05, doi:10.1029/2008GL036659.
2. Allen, R. M., H. Kanamori, (2003). The potential for earthquake early warning in Southern California. *Science.* ;300:786–789.
3. Allen, R.M., P. Gasparini, O. Kamigaichi, M. Bose, (2009). The Status of Earthquake Early Warning around the World: An Introductory Overview, *Seismol Res Lett*, 80(5), 682-693, doi 10.1785/gssrl.80.5.682.
4. Amoroso, O., N. Maercklin, and A. Zollo (2012), S-wave identification by polarization filtering and waveform coherence analyses, *Bull. Seismol. Soc. Am.*, 102(2), 854–861, doi:10.1785/0120110140.
5. Bernard, P., and A. Zollo (1989). The Irpinia (Italy) 1980 earthquake: Detailed analysis of a complex normal fault. *Journal of Geophysical Research* 94, 1,631–1,648.
6. Boore, D. M., C. D. Stephens, and W. B. Joyner., (2002). Comments on baseline correction of digital strong-motion data: Examples from the 1999 Hector Mine, California, earthquake, *Bull. Seism. Soc. Am.* 92, 1543–1560.
7. Böse, M., C. Ionescu, F. Wenzel, (2007). Earthquake early warning for Bucharest, Romania: Novel and revised scaling relations. *Geophys. Res. Lett.* ;34:L07302. doi: 10.1029/2007GL029396.
8. Böse, M., E. Hauksson, K. Solanki, H. Kanamori, and T. H. Heaton (2009), Real-time testing of the on-site warning algorithm in southern California and its performance during



- the July 29 2008 Mw5.4 Chino Hills earthquake, *Geophys. Res. Lett.*, 36, L00B03, doi:10.1029/2008GL036366.
9. Brondi, P., M. Picozzi, A. Emolo, A. Zollo, and M. Mucciarelli (2015). Predicting the macroseismic intensity from early radiated P wave energy for on-site earthquake early warning in Italy, *J. Geophys. Res. Solid Earth*, 120, 7174–7189, doi:10.1002/2015JB012367.
  10. Böse, M., R.M. Allen, H. Brown, G. Cua, M. Fischer, E. Hauksson, T. Heaton, M. Hellweg, M. Liukis, D. Neuhauser, P. Maechling and CISN EEW Group (2013), CISN ShakeAlert – An Earthquake Early Warning Demonstration System for California in: F. Wenzel and J. Zschau (eds.) *Early Warning for Geological Disasters - Scientific Methods and Current Practice*; ISBN: 978-3-642-12232-3, Springer Berlin Heidelberg New York.
  11. Carranza, M., E. Buforn, S. Colombelli, and A. Zollo (2013), Earthquake early warning for southern Iberia: A P wave threshold-based approach, *Geophys. Res. Lett.*, 40, doi:10.1002/grl.50903.
  12. Colombelli, S., A. Caruso, A. Zollo, G. Festa and H. Kanamori, (2015). A P wave-based, on-site method for earthquake early warning. *Geophys. Res. Lett.*, 42: 1390–1398. doi: 10.1002/2014GL063002.
  13. Colombelli, S., A. Zollo, G. Festa, and H. Kanamori (2012b), Early magnitude and potential damage zone estimates for the great Mw 9 Tohoku-Oki earthquake, *Geophys. Res. Lett.*, 39, L22306, doi:10.1029/2012GL053923.
  14. Colombelli, S., A. Zollo, G. Festa, and M. Picozzi (2014), Evidence for a difference in rupture initiation between small and large earthquakes. *Nat. Comm.* 5:3958 doi: 10.1038/ncomms4958.
  15. Colombelli, S., O. Amoroso, A. Zollo, and H. Kanamori (2012a), Test of a threshold-based

- earthquake early warning using Japanese data, *Bull. Seismol. Soc. Am.*, 102, 1266–1275, doi:10.1785/0120110149.
16. Cua, G. and T. H. Heaton, (2007). The Virtual Seismologist (VS) method: a Bayesian approach to earthquake early warning. In "Earthquake Early Warning Systems", P. Gasparini, G. Manfredi, J. Zschau (Eds), Springer, ISBN-13 978-3-540-72240-3.
  17. Cua, G., M. Fischer, T. Heaton, S. Wiemer, D. Giardini, (2009). Real-time performance of the Virtual Seismologist method in southern California. *Seismol. Res. Lett.* 80(5) p740-747.
  18. Diehl, T., N. Deichmann, E. Kissling and S. Husen (2009), Automatic S-wave picker for local earthquake tomography, *Bull. Seism. Soc. Am.*, 99, 1906-1920, doi:10.1785/0120080019.
  19. Emolo A., M. Picozzi, G. Festa, C. Martino, S. Colombelli, A. Caruso, L. Elia, A. Zollo, P. Brondi, N. Miranda (2016). Earthquake early warning feasibility in the Campania Region (Southern Italy) and demonstration system for public school buildings. *Bull. Earthquake Eng.*, doi: 10.1007/s10518-016-9865-z.
  20. Espinosa Aranda, J.M., A. Jiménez, G. Ibarrola, F. Alcantar, A. Aguilar, M. Inostrosa, and S. Maldonado (1995), Mexico City Seismic Alert System, *Seism. Res. Lett.* Vol. 66, No. 6, 42-52.
  21. Espinosa-Aranda, J.M., A. Cuellar, A. Garcia, G. Ibarrola, R. Islas, S. Maldonado, and F.H. Rodriguez (2009), Evolution of the Mexican Seismic Alert System (SASMEX), *Seism. Res. Lett.* 80 694-706.
  22. Faenza L. and A. Michelini, (2010), Regression analysis of MCS intensity and ground motion parameters in Italy and its application in ShakeMap. *Geophysical Journal International*, 180: 1138–1152. doi: 10.1111/j.1365-246X.2009.04467.x.
  23. Festa, G., M. Lancieri, and A. Zollo (2008), Magnitude estimation from early radiated

- energy, *Geophys. Res. Lett.*, 35, L22307, doi:10.1029/2008GL035576.
24. Goldstein, P., D. Dodge, M. Firpoand, and L. Minner (2003). SAC2000: Signal processing and analysis tools for seismologists and engineers, in the IASPEI International Handbook of Earthquake and Engineering Seismology, W. H. K. Lee, H. Kanamori, P. C. Jennings, and C. Kisslinger (Editors), Academic Press, London.
  25. Gorini et al. (2010) The Italian Strong Motion Network. *Bull Earthq Eng*, 8: 1075-1090. Guidoboni, E., G. Ferrari, D. Mariotti, A. Comastri, G. Tarabusi and G. Valensise, (2007). CFTI4Med, Catalogue of Strong Earthquakes in Italy (461 B.C.-1997) and Mediterranean Area (760 B.C.-1500). INGV-SGA. <http://storing.ingv.it/cfti4med/>.
  26. Horiuchi, S., H. Negishi, K. Abe, A. Kamimura, and Y. Fujinawa (2005), An automatic processing system for broadcasting system earthquake alarms, *Bull. Seism. Soc. Am.* 95 347–353.
  27. Hoshiaba, M. (2013). Real-time prediction of ground motion by Kirchhoff-Fresnel boundary integral equation method: Extended front detection method for earthquake early warning. *Journal of Geophysical Research: Solid Earth*, 118(3):1038-1050.
  28. Hoshiaba, M. and Aoki, S. (2015). Numerical shake prediction for earthquake early warning: Data assimilation, real-time shake mapping, and simulation of wave propagation. *Bulletin of the Seismological Society of America*, 105(3):1324-1338.
  29. Hoshiaba, M., K. Iwakiri, N. Hayashimoto, T. Shimoyama, K. Hirano, Y. Yamada, Y. Ishigaki, and H. Kikuta (2011), Outline of the 2011 off the Pacific coast of Tohoku Earthquake (Mw 9.0) – Earthquake Early Warning and observed seismic intensity-, *Earth Planets Space* 63, 547—551.
  30. Hoshiaba, M., O. Kamigaichi, M. Saito, S. Tsukada, and N. Hamada (2008), Earthquake Early Warning Starts Nationwide in Japan, *Eos Trans. AGU*, 89(8), 73–74,

doi:10.1029/2008EO080001.

31. Ionescu, C., M. Böse, F. Wenzel, A. Marmureanu, A. Grigore, G. Marmureanu, (2007). An Early Warning System for Deep Vrancea (Romania) Earthquakes, pp 343-349 *Earthquake Early Warning Systems*, Editors P. Gasparini, G. Manfredi, J. Zschau. Springer Berlin Heidelberg New York, ISBN-13 978-3-540-72240-3, DOI: 10.1007/978-3-540-72241-0\_17.
32. John, C., A. Zollo, A. Marmureanu, C. Zulfikar, S. Parolai, (2016). State-of-the art and future of earthquake early warning in the European region, *Bull Earthquake Eng*, doi: 10.1007/s10518-016-9922-7.
33. Kamigaichi, O., M. Saito, K. Doi, T. Matsumori, K. Takeda, T. Shimoyama, K. Nakamura, M. Kiyokoto, Y. Watanabe, (2009). Earthquake early warning in Japan: warning the general public and future prospects, *Sesimological research Letters*, 80: 717-726.
34. Kanamori, H. (2005), *Real-Time Seismology and Earthquake Damage Mitigation*, *Annu. Rev. Earth Planet. Sci.*, 33, 195--214 doi: 10.1146/annurev.earth.33.092203.122626.
35. Kuyuk, H. S., R. M. Allen, H. M. Brown, M. Hellweg, I. Henson, and D. Neuhauser, (2014). Designing a network-based earthquake early warning algorithm for California: ElarmS-2, *Bull. Seismol. Soc. Am.* 104, no. 1, 162–173, doi: 10.1785/0120130146.
36. Kuyuk, H.S., R.M. Allen (2013) Optimal Seismic Network Density for Earthquake Early Warning: A Case Study from California *Seismo. Res. Lett.*, 84(6), pp 946-954.
37. Libslink. Client library for receiving continuous data streams from SeedLink servers, 2013, <http://www.iris.edu/pub/programs/SeedLink> (last accessed January 2016).
38. Locati M., R. Camassi, and M. Stucchi (2011). DBMI11, la versione 2011 del Database Macrosismico Italiano. Milano, Bologna, doi:10.6092/INGV.IT-DBMI11. [Available at <http://emidius.mi.ingv.it/DBMI11>.].
39. Lomax, A., S. Satriano and M. Vassallo, (2012). Automatic picker developments and

- optimization: FilterPicker - a robust, broadband picker for real-time seismic monitoring and earthquake early-warning, *Seism. Res. Lett.*, 83:531-540, doi: 10.1785/gssrl.83.3.531.
40. Luzi, L., S. Hailemichael, D. Bindi, F. Pacor, F. Mele, F. Sabetta, (2008). ITACA (ITalianACcelerometric Archive): a web portal for the dissemination of Italian strong motion data. *Seismol Res Lett.* doi:10.1785/gssrl.79.5.
  41. Nakamura, Y [1988] On the urgent earthquake detection and alarm system (UrEDAS), Proceedings of Ninth World Conference on Earthquake Engineering, Paper # 13-2-12, August 2-9, 1988, Tokyo-Kyoto, Japan (Vol. VII), pages VII-673-Vii-678.
  42. Nakamura, Y. (1984). Development of the earthquake early-warning system for the Shinkansen, some recent earthquake engineering research and practical in Japan. The Japanese National Committee of the International Association for Earthquake Engineering, 224–238.
  43. Nakamura, Y. (1988). On the urgent earthquake detection and alarm system (UrEDAS), in Proceedings of Ninth World Conference on Earthquake Engineering, Paper# 13-2-12, vol. VII, pp. 673–678, Tokyo-Kyoto, 2–9 Aug.
  44. Odaka, T., K. Ashiya, S. Tsukada, S. Sato, K. Ohtake, and D. Nozaka (2003), A new method of quickly estimating epicentral distance and magnitude from a single seismic record, *Bull. Seism. Soc. Am.* 93 526-532.
  45. Ohta, Y., M. Ohzono, S. Miura, T. Iinuma, K. Tachibana, K. Takatsuka, K. Miyao, T. Sato, and N. Umino, Coseismic fault model of the 2008 Iwate-Miyagi Nairiku earthquake deduced by a dense GPS network, *Earth Planets Space*, 60, 1197–1201, 2008.
  46. Pacor, F., R. Paolucci, L. Luzi, F. Sabetta, A. Spinelli, A. Gorini, M. Nicoletti, S. Marcucci, L. Filippi, and M. Dolce (2011), Overview of the Italian strong motion database ITACA 1.0, *Bull Earthquake Eng*, 9(6), 1723–1739, doi:10.1007/s10518-011-9327-6.

47. Peng, H.S., Z.L. Wu, Y.M. Wu, S.M. Yu, D.N. Zhang, and W.H. Huang (2011), Developing a prototype earthquake early warning system in the Beijing Capital Region, *Seism. Res. Lett.* 82 394-403.
48. Picozzi, M., (2012). An attempt of real-time structural response assessment by an interferometric approach: a tailor-made earthquake early warning for buildings. *Soil Dynamics and Earthquake Engineering*, 38, 109–118. doi:10.1016/j.soildyn.2012.02.003.
49. Picozzi, M., A. Zollo, P. Brondi, S. Colombelli, L. Elia, and C. Martino (2015a). Exploring the feasibility of a nationwide earthquake early warning system in Italy. *J. Geophys. Res. Solid Earth*, 120, 2446–2465. doi: 10.1002/2014JB011669.
50. Picozzi, M., Emolo A., Martino C., Zollo A., Miranda N., Verderame G., Boxberger T., and the REAKT Working Group (2015b). Earthquake Early Warning System for Schools: A Feasibility Study in Southern Italy. *Seismological Research Letters*, Volume 86, Number 2 March/April 2015. doi: 10.1785/0220140194.
51. Rosenberger, A. (2010), Real-time ground-motion analysis: Distinguishing P and S arrivals in a noisy environment, *Bull. Seismol. Soc. Am.*, 100,1252–1262.
52. Rydelek, P. and S. Horiuchi (2006), Is earthquake rupture deterministic? *Nature*, 442, doi:10.1038/nature04963.
53. Rydelek, P., C. Wu, and S. Horiuchi (2007), Comment on “Earthquake magnitude estimation from peak amplitudes of very early seismic signals on strong motion records” by Aldo Zollo, Maria Lancieri, and Stefan Nielsen, *Geophys. Res. Lett.*, 34, doi:10.1029/2007GL029387.
54. S. Ozawa, Nishimura T., Suito H., Kobayashi T., Tobita M., Imakiire T. (2012), Coseismic and postseismic slip of the 2011 magnitude-9 Tohoku-Oki earthquake, *Nature*. 2011 Jun 15;475(7356):373-6. doi: 10.1038/nature10227.

55. Satriano, C., Elia L., Martino C., Lancieri M., Zollo A. and Iannaccone G. (2011). PRESTo, the earthquake early warning system for Southern Italy: concepts, capabilities and future perspectives. *Soil Dyn. Earthq. Eng.*, 31 (2), 137–153, doi: 10.1016/j.soildyn.2010.06.008.
56. SeisComP. Seismological Communication Processor, (2016), <https://www.seiscomp3.org> (last accessed January 2016).
57. Shieh, J.-T., Y.-M. Wu, and R. M. Allen (2008), A comparison of  $\tau_c$  and  $\tau_{pmax}$  for magnitude estimation in earthquake early warning, *Geophys. Res. Lett.*, 35, L20301, doi: 10.1029/2008GL035611.
58. Ueno, H., S. Hatakeyama, T. Aketagawa, J. Funasaki, and N. Hamada (2002), Improvement of hypocenter determination procedures in the Japan Meteorological Agency (in Japanese with English abstract), *Q. J. Seismol.*, 65, 123–134.
59. Wald, D. J., V. Quitoriano, T.H. Heaton, and H. Kanamori (1999), Relationships between Peak Ground Acceleration, Peak Ground Velocity and Modified Mercalli Intensity in California, *Earthquake Spectra*, 15, 557-564.
60. Weber, E., V. Convertito, G. Iannaccone, A. Zollo, A. Bobbio, L. Cantore, M. Corciulo, M. Di Crosta, L. Elia, C. Martino, A. Romeo, C. Satriano, (2007). An Advanced Seismic Network in the Southern Apennines (Italy) for Seismicity Investigations and Experimentation with Earthquake Early Warning. *Seismol Res Lett*, 78 (6), 622-634, doi 10.1785/gssrl.78.6.622.
61. Worden, C.B., D.J. Wald, T.I. Allen, K.W. Lin, D. Garcia, and G. Cua (2010). A revised ground-motion and intensity interpolation scheme for ShakeMap, *Bull. Seism. Soc. Am.* 100(6), 3083-3096.
62. Wu, Y. M., H. Y. Yen, L. Zhao, B. S. Huang, W. T. Liang, (2006). Magnitude determination using initial P waves: A single-station approach. *Geophys. Res.*

- Lett. ;33:L05306. doi: 10.1029/2005GL025395.
63. Wu, Y. M., T. L. Teng, (2002). A virtual sub-network approach to earthquake early warning. *Bull. Seism. Soc. Am.* ;92:2008–2018.
  64. Wu, Y.M. and H. Kanamori (2005), Experiment of an on-site method for the Taiwan Early Warning System, *Bull. Seism. Soc. Am.* 95, 347--353 doi:10.1785/0120040097.
  65. Wu, Y.M. and H. Kanamori (2008), Development of an earthquake early warning system using real-time strong motion signals, *Sensors* 8, 1-9.
  66. Wu, Y.M. and L. Zhao (2006), Magnitude estimation using the first three seconds P-wave amplitude in earthquake early warning, *Geophys Res Lett.* 33 L16312 doi:10.1029/2006GL026871.
  67. Wu, Y.-M., & H. Kanamori, (2005). Rapid Assessment of Damage Potential of Earthquakes in Taiwan from the Beginning of P Waves. *Bulletin of the Seismological Society of America*, 95 (3). pp. 1181-1185. ISSN 0037-1106.
  68. Zollo, A, O. Amoroso, M. Lancieri, Y.M. Wu and H. Kanamori (2010), A threshold-based earthquake early warning using dense accelerometer networks, *Geophys J Int* 183 963-974.
  69. Zollo, A., A. Emolo, S. Colombelli, L. Elia, G. Festa, C. Martino, and M. Picozzi (2013), PRESTo - Probabilistic and Evolutionary Early Warning System: Concepts, Performances, and Case Studies, S41A AGU2013-2407, American Geoscience Union Fall Meeting, 2013, San Francisco, CA, USA.
  70. Zollo, A., G. Iannaccone, M. Lancieri, L. Cantore, V. Convertito, A. Emolo, G. Festa, F. Gallovic, M. Vassallo, C. Martino, C. Satriano, P. Gasparini, (2009). The earthquake early warning system in Southern Italy: Methodologies and performance evaluation, *Geophys Res Lett*, 36, L00B07, doi: 10.1029/2008GL036689.
  71. Zollo, A., M. Lancieri, and S. Nielsen (2007), Reply to comment by P. Rydelek et al. on



- “Earthquake magnitude estimation from peak amplitudes of very early seismic signals on strong motion records”, *Geophys. Res. Lett.*, 34, L20303, doi:10.1029/2007GL030560.
72. Zollo, A., M. Lancieri, S. Nielsen, (2006). Earthquake magnitude estimation from peak amplitudes of very early seismic signals on strong motion records. *Geophys. Res. Lett.* ;33:L23312. doi: 10.1029/2006GL027795.
73. Zollo, A., O. Amoroso, M. Lancieri, Y. M. Wu and H. Kanamori, (2010). A threshold-based earthquake early warning using dense accelerometer networks. *Geophysical Journal International*, 183: 963–974. doi: 10.1111/j.1365-246X.2010.04765.x.
74. Zollo, A., S. Colombelli, L. Elia, A. Emolo, G. Festa, G. Iannaccone, C. Martino, and P. Gasparini (2014), An integrated regional and on-site Earthquake Early Warning System for Southern Italy: Concepts, methodologies and performances, in *Early Warning for Geological Disasters Scientific Methods and Current Practices*, edited by F. Wenzel and J. Zschau, pp. 117–137, Springer, Berlin.

**Analytical Evaluation of PhD Dissertation**  
**PhD Program in Structural, Geotechnical and Seismic Risk Analysis**  
**Cycle 30°**

Referee (*First name and surname*) ..... Anthony Lomax .....

University of : ..... ALomax Scientific .....

**PhD Candidate** (*First name and surname*) ..... **Alessandro Caruso**.....

**Analytical Evaluation of the Dissertation** .....

The dissertation contains a thorough, interesting and practical presentation and evaluation of three, strategies for earthquake early-warning. Numerous complicated algorithms and procedures are well explained, illustrated and validated. The dissertation will form a useful and potentially high impact reference for workers in earthquake early-warning.

Suggested changes and additions:

The original contributions of the candidate to the work should be more clearly noted or listed.

Add more details on tau\_c algorithm (Kanamori, 2005) used for SAVE.

Section "1.3 Application and results" should start with summary sentences.

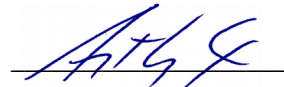
On account of the previous evaluation:

The above mentioned candidate can defend his dissertation in the ordinary session of the final exams;

The above mentioned candidate can defend his dissertation in the **straordinary** session of the final exams;  
\*;

Date \_\_ 10/11/2017 \_\_

Signature



\* the straordinary session will be held not later than june 30<sup>th</sup>, 2018

**GIUDIZIO ANALITICO SU TESI DOTTORATO DI RICERCA**  
**Dottorato di Ricerca in Ingegneria Strutturale, Geotecnica e Rischio Sismico**  
**Ciclo 30°**

VALUTATORE (nome e cognome) Stefano Parolai

DOCENTE PRESSO : TU Berlin, Direttore CRS OGS TRIeste.....

.....

**DOTTORANDO (nome e cognome) ...Alessandro...Caruso.....**

**Giudizio analitico sulla tesi ...La tesi "Earthquake Early warning Strategies for on-site and network based system"** riassume una enorme quantita' di lavoro effettuata dal candidato nell'ambito dello sviluppo e miglioramento di sistemi di early warning. La tesi presenta alcuni aspetti innovativi e di sicuro interesse per applicazioni future. Il candidato sembra aver ben approfondito lo studio di sistemi di allarme sismico e di aver approfondito il problema sviluppando una ottima capacita' di confrontarsi con diversi aspetti riguardante l'allarme sismico. In generale ho apprezzato la capacita' di affrontare l'argomento partendo da una solida e robusta analisi di grandi data set che forniscono uno degli ingredienti principali per le analisi svolte successivamente e che richiedono una buona conoscenza dell'analisi del segnale e dei principi della sismologia. A mio parere, la tesi potrebbe aver beneficiato di una migliore organizzazione della struttura (ad es l'ultimo capitolo al momento sembra entrare un poco forzatamente nel lavoro) che avrebbero meglio valorizzato la notevole, e di alta qualita', mole di lavoro svolto. In particolare suggerirei di riveder alcune sviste (e.g. mancanza del nome del candidato sulla tesi, erronee o mancanti referenze alle figure nel testo) e soprattutto l'inglese. ....

.....

.....

.....

.....

.....  
.....  
.....  
.....

Pertanto:

Il dottorando sopra citato è ammesso alla discussione pubblica della tesi nella sessione ordinaria degli esami finali;

Il dottorando sopra citato è ammesso alla discussione pubblica della tesi con rinvio alla sessione straordinaria degli esami finali \*;

Data 9.11.2017

Firma

Stef. Pali.

\* la sessione straordinaria degli esami finali sarà fissata entro il 30 giugno 2018

UNIVERSITÀ DEGLI STUDI DI NAPOLI  
FEDERICO II



Dottorato di Ricerca in  
INGEGNERIA STRUTTURALE, GEOTECNICA e RISCHIO SISMICO  
30° CICLO

*Collegio dei Docenti*

Proff.: Alessandro Baratta, Antonio De Luca, Antonio Emolo, Massimiliano Fraldi, Giovanni Iannaccone, Iunio Iervolino, Raffaele Landolfo, Claudio Mancuso, Gaetano Mandredi, Emidio Nigro, Matteo Picozzi, Luciano Rosati, Antonio Santo, Francesco Silvestri, Gerardo Verderame, Gianfranco Urciuoli, Aldo Zollo, Giulio Zuccaro

Coordinatore: Prof. Luciano Rosati

*Relazione finale del Collegio sul dottorando*

NOME COGNOME  
ALESSANDRO CARUSO

Novembre 2014 – Ottobre 2017

Il Coordinatore

Prof. Luciano Rosati

(firma)  
*Luciano Rosati*

Correlatrice

Dott.ssa Simona Colombelli

(firma)

*Simona Colombelli*

il tutor

Prof. Aldo Zollo

(firma)

*Aldo Zollo*

Il dottorando

Dott. Alessandro Caruso

(firma)

*Alessandro Caruso*

## RELAZIONE FINALE DEL COLLEGIO DEI DOCENTI

Il candidato ha svolto il Dottorato di Ricerca presso il laboratorio di sismologia del Dipartimento di Fisica "E. Pancini", dell'Università degli Studi di Napoli, Federico II. Durante il suo percorso di dottorato, il candidato ha lavorato assiduamente alla sua tematica di ricerca principale, contribuendo attivamente alla concezione e allo sviluppo delle metodologie proposte. Lo studente ha mostrato una buona conoscenza e padronanza della tematica dell'Early Warning, dimostrando di saperne approfondire tutti gli aspetti, nonché una buona capacità di analisi ed interpretazione dei risultati ottenuti, come testimoniato dalle pubblicazioni su riviste scientifiche internazionali, delle quali Alessandro Caruso è co-autore.

Sempre presso il laboratorio di sismologia, lo studente ha inoltre collaborato assiduamente ad altre attività del gruppo di ricerca, quali la revisione degli eventi sismici della rete ISNet e i seminari di gruppo, che hanno consentito al candidato di ampliare la conoscenza in tematiche attinenti al suo tema di ricerca dominante.

Infine, lo studente ha svolto attività didattica presso il dipartimento di Fisica, nelle esercitazioni pratiche del corso di Analisi ed elaborazione numerica dei Segnali e del corso di Sismologia, entrambi tenuti dal prof. Aldo Zollo.

Il dottorando Alessandro Caruso ha svolto attività di ricerca nell'ambito del Rischio Sismico, occupandosi, nello specifico, di Sistemi di Early Warning, che rientrano tra le strategie più efficaci per la mitigazione del rischio sismico in tempo reale. La tematica trattata è di grande attualità e di forte interesse per la comunità sismologica nazionale ed internazionale, come sottolineato anche dai revisori del manoscritto.

La tesi è strutturata in 3 capitoli. I primi due capitoli sono dedicati alla proposizione di metodologie per i sistemi di early warning. Nel primo capitolo, si presenta una metodologia innovativa per l'early warning a singola stazione, denominata SAVE, che consente di caratterizzare rapidamente l'intensità dello scuotimento del suolo atteso al sito, e di avere stime approssimative della magnitudo dell'evento e della sua distanza dal sito di registrazione. Nel secondo capitolo, si propone una strategia più accurata per un sistema di allerta di tipo on-site. Questo approccio è basato su tecniche raffinate per l'analisi dei dati che, unite ad un approccio multi-parametrico, consentono di ottenere predizioni più affidabili dello scuotimento del suolo al sito target.

Il terzo capitolo, poi, descrive una nuova metodologia che integra gli approcci di tipo regionale e on-site, per una predizione accurata del livello di danneggiamento atteso ai siti target. Questa metodologia, nella tesi denominata "Quake-Up", racchiude gli elementi più innovativi per l'analisi dei dati in tempo reale e pone le basi per una nuova generazione di sistemi di early warning, nella quale la caratterizzazione accurata dell'area di danneggiamento e degli effetti attesi ad uno o più siti di interesse, acquisisce maggiore rilievo.

Nel quarto capitolo, infine, il candidato illustra i risultati della sua esperienza di formazione presso l'azienda TME (Testing and Manufactory Engineering) in Via Carlo Alberto Dalla Chiesa 81050 - Portico di Caserta Caserta (NA). Durante questo stage semestrale, Alessandro Caruso ha appreso gli elementi tecnici basilari per lo sviluppo e l'implementazione di algoritmi all'interno di una stazione sismica, nella tesi denominata MOMA.

La tesi di Alessandro Caruso sintetizza un notevole lavoro svolto durante i tre anni di dottorato, attraverso il quale il candidato ha maturato una buona conoscenza e padronanza della tematica trattata. Alcune parti del manoscritto, sono state anche oggetto di pubblicazioni su riviste scientifiche internazionali, confermando l'adeguatezza e la validità delle metodologie proposte, nonché la rilevanza scientifica delle stesse.

Il Coordinatore

Prof. Luciano Rosati

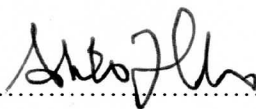
(firma)



Il Tutor

Prof. Aldo Zollo

(firma)



Dott.ssa SIMONA COLOMBELLI

